2021

Biophysical Analysis of the Structure and Aggregation of Amyloid beta Peptide

Faisal Abedin
University of Central Florida

BIOPHYSICAL ANALYSIS OF THE STRUCTURE AND AGGREGATION OF AMYLOID β PEPTIDE

By

FAISAL ABEDIN

BS: Physics (University of Dhaka, 2012)

MS: Physics (University of Texas at El Paso, 2016)

A dissertation submitted in partial fulfilment of the requirements
for the degree of Doctor of Philosophy
in the Department of Physics
in the College of Sciences
at the University of Central Florida
Orlando, Florida.

Summer Term
2021

Major Professor: Suren Tatulian

ABSTRACT

Alzheimer's disease (AD) is the major cause of dementia and is characterized by neuronal death and brain atrophy. The amyloid β (Aβ) peptide is tightly associated with neuronal dysfunction during AD, but the molecular mechanism underlying the neurotoxic effect of Aβ is poorly understood. Extracellular fibrillar deposits (plaques) of Aβ were initially believed to be the cause of AD, but currently there is overwhelming evidence that the prefibrillar Aβ oligomers are the major toxic entities. Structural characterization of Aβ oligomers and fibrils is important for understanding the structural features determining the toxic potency of the peptide. This project has studied the aggregation and accompanying structural transitions of Aβ, a naturally occurring hypertoxic species, i.e. pyroglutamylated Aβ, and their combination, using biophysical approaches (circular dichroism, fluorescence, infrared spectroscopy). In addition, aggregation and structure of overlapping peptide fragments have been studied to identify the specific stretch of Aβ that serves as seeding region initiating the aggregation and fibril formation by the full-length Aβ peptide. These studies elucidate the structural features of Aβ responsible for the peptide's neurotoxic action.

Dedicated to my parents
A.B.M. Zainal Abedin
Morsheda Begum

ACKONWLEDGEMENT

I would like to acknowledge and give my warmest thanks to my supervisor (Dr. Suren Tatulian) who has the attitude and the substance of a genius; he continuously and convincingly conveyed a spirit of adventure in regard to research and made this work possible. His guidance and advice carried me through all the stages of writing my project. I would also like to thank my committee members for their continued support and encouragement: Dr. Talat Rahman, Dr. Aniket Bhattacharya, Dr. Ellen Kang and Dr. Kenneth Teter. I offer my sincere appreciation for the learning opportunities provided by my committee.

I would also like to give special thanks to and my family and very close friends for their continuous support and understanding when undertaking my research and writing my project. Your prayer for me was what sustained me this far.

Finally, I would like to thank God, for letting me through all the difficulties. I have experienced your guidance day by day.

TABEL OF CONTENTS

LIST OF FIGURES

LIST OF TABLES

CHAPTER 1: INTRODUCTION

1.1 Amyloid β Peptide Structure and Toxicity

Alzheimer's disease (AD) is a neurodegenerative pathology that mostly affects elderly people and causes cognitive decline and dementia. The underlying pathology is brain atrophy, synaptic loss and neuronal cell death [1]. At the molecular level, extracellular fibrillar deposits (plaques) formed by the amyloid β (Aβ) peptide and intracellular accumulation of neurofibrillary tangles of tau protein are the major histopathological traits of AD [2-4].

Aβ plaques were initially believed to cause the onset and progression of AD, but further studies provided strong evidence that the prefibrillar oligomeric form of Aβ, rather than fibrillar aggregates, constitutes the main cytotoxic entity [5]. The molecular mechanism by which Aβ oligomers kill neuronal cells is yet to be identified, but the extensive research has delineated several pathways. One of the prevalent mechanisms of Aβ neurotoxicity is formation of pores or ion channels in cellular membranes, causing dysregulation of cellular homeostasis and neuronal cell death [6-8]. For example, binding of Aβ to the endoplasmic reticulum (ER) and pore formation results in Ca^{2+} release, followed by abnormal activation of certain cytosolic enzymes and apoptotic cell death [9-13]. Recruitment of Aβ to mitochondria and altered mitochondrial dynamics has been identified as another mechanism of apoptotic neuronal cell death during AD [10,14-17]. Lastly, a variety of unrelated receptors bind Aβ, leading to disruption of cell signaling pathways and cellular damage through apoptosis or necrosis [18-20].

Aβ is derived from a bitopic protein in neuronal membrane, amyloid precursor protein (APP), by β- and γ-secretases, which cleave APP in the transmembrane and extracellular juxtamembrane regions [21]. The pathogenicity of Aβ depends on many factors, specifically the peptide species, their aggregation state, the composition of the assemblies, and the peptide's

secondary, tertiary, and quaternary structures. Due to poor sequence specificity of the secretases, as well as because of further proteolytic processing, Aβ species of various lengths are produced in human brain. The 40 and 42-amoino acid residue peptides ($A\beta_{1-40}$ and $A\beta_{1-42}$ are) are the prevalent forms. APP can also be cleaved by α-secretase, which does not produce Aβ (Figure 1.1)

It has been reported that the Aβ oligomers undergo a conformational switch from random coil or α-helix to highly toxic β-sheet structure [22]. Successful design of molecules capable of interacting with

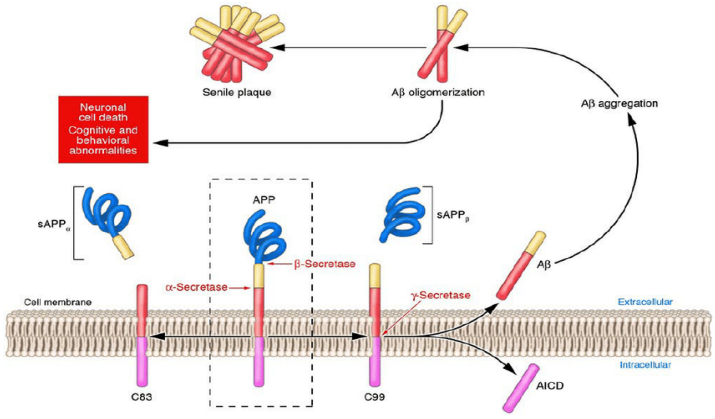

Figure 1. 1**:** The non-amyloidogenic and amyloidogenic pathways of APP processing. Cleavage of APP by α-secretase produces sAPPα which is harmless, whereas cleavage of APP by β- and γ-secretases produces the amyloidogenic Aβ peptide. Source: Petra E. Spies et al. [23].

Aβ as inhibitors of aggregation or as inhibitors of membrane pore formation may lead to fundamental progress in the improvement of anti-Alzheimer therapies [24,25]. However, such efforts will require a detailed knowledge of the structural features of various toxic forms of Aβ peptides. The major objective of this project is to help accumulate such knowledge. Specifically, the project is designed to achieve a mechanistic understanding of the conformational changes of

Aβ peptide in aqueous environment by using biophysical approaches, such as circular dichroism (CD), Fourier transform infrared spectroscopy (FTIR) and fluorescence spectroscopy (FS).

1.2 Different Forms of Aβ

The full-length $A\beta_{1-42}$ with sequence NH_2-DAEFRHDSGYEVHH QKLVFFAEDVGSN KGAIIGLMVGGVVIA-COOH is amphiphilic as its N-terminal half is hydrophilic and the C-terminal half is mostly nonpolar. Interaction of $A\beta_{1-42}$ with ER membrane has been shown to activate the ryanodine receptor ion channel and dysregulate intracellular calcium homeostasis [26, 27]. Lin et al. [28] have shown that $A\beta_{1-42}$ has globular structure that forms multimeric channel-like assemblies in a planar lipid bilayer. Alternatively, it has been reported that Aβ forms fibrils consisting of antiparallel β-sheets and β-hairpins at residues 24 to 29, with intramolecular hydrogen bonding between β-strands on either side of a β-turn and a bend in residues 23 to 26 [29].

$A\beta_{1–40}$ is the most abundant Aβ species and possesses significant neurotoxicity. Coles et al. [30] reported that the first 14 residues of $A\beta_{1–40}$ are structurally disordered in the fibrils, the rest of the protein adopts an α-helical conformation between residues 15 and 36 with a kink or hinge at 25−27. $A\beta_{1–40}$ contains central (residues 17-21) and C-terminal (residues 30-40) hydrophobic segments. Formation of parallel β-sheet structure might be hampered by electrostatic repulsions between similar charges.

Recently, Alomar et al have done an observational study of $A\beta_{1–42}$ and $A\beta_{1–40}$ in the cerebrospinal fluid during pregnancy. There it has been documented the higher concentrations of $A\beta_{1-42}$ in cerebrospinal fluid of third trimester pregnancies and correlations between the beta-amyloid ratio and the vascular endothelial growth factor support the hypothesis that beta-amyloid peptides are involved in complex adaptive brain alterations during pregnancy.[31]

it has been reported that transition of $A\beta_{1–40}$ from α-helical structure cytotoxic β-sheet structure occurs due to the variation in the solvent polarity; additionally, change in pH and salt concentration cause transition of oligomers into protofibrils, followed by amyloid fibril formation [32]. There is evidence that amyloid fibrils of $A\beta_{1–40}$ initiate amyloid formation in different globular proteins and metabolites, converting native structures into β-sheet rich assemblies [33]. Moreover, contacts between Aβ peptide's cross β structure and the native folds of proteins mediated through H-bonds and hydrophobic interactions, resulting in onset of amyloid cross-seeding [33]. It has also been reported that the mixture of monomeric ^{13}C-labeled $A\beta_{1–40}$ and unlabeled $A\beta_{1–42}$ form mixed oligomers with largely random distribution of $A\beta_{1–40}$ and $A\beta_{1–42}$ [34]. A combination of nuclear magnetic resonance, thioflavin-T fluorescence, transmission electron microscopy and dynamic light scattering was applied to characterize the aggregation kinetics of $A\beta_{1-40}$ peptide where it was reported that at 37 °C soluble $A\beta_{1-40}$ remains intrinsically disordered and mostly in monomeric form despite evidence of the presence of dimers and/or other small oligomers.[35]

Okada et al. [36] reported that the fibril formation of $A\beta_{1–40}$ on monosialoganglioside GM1 clusters are more cytotoxic than those formed in aqueous solution and the structure of this highly toxic fibril contains in register parallel and two-residue-shifted antiparallel β-sheet however less toxic fibril contains only in register parallel β-sheet. The study of aggregation $A\beta_{1–40}$ was performed by using NMR spectroscopy which showed that the aggregation was initiated by reversible transient oligomers, followed by formation of fibrils [37].

The brains of cognitively normal individuals may contain large amounts of Aβ peptides [38]. During the onset and progression of AD, N-terminally truncated hypertoxic Aβ species bearing the pyroglutamate modification accumulates and reaches 40-50% of total Aβ load [39-46]. It has been reported that pyroglutamate-Aβ (pE-Aβ) has a higher proclivity for aggregation than the unmodified full-length Aβ by a seeding mechanism and is resistant to degradation, allowing these peptides to persist in biological fluids and tissues [38]. The formation of pE-Aβ is a multi-step process (Figure 1.2). Naturally occurring enzymatic removal of the first two amino acid residues of Aβ and pyroglutamylation of Glu3 produces Aβ species of elevated toxicity, i.e., $pEA\beta_{3\text{-}40}$ [47,48].

$pEA\beta_{3\text{-}40}$ is more hydrophobic than $A\beta_{1\text{-}40}$ due to the loss of negative charges from the Asp1 and Glu3 residues, and formation of the lactam ring in the pE residue. $A\beta_{pE3\text{-}40}$ aggregates earlier and acts as a seed for Aβ aggregation by self-aggregation and co-aggregation with $A\beta_{1\text{-}40/42}$, playing a critical role in the early stage of amyloid formation in AD displaying an enhanced cytotoxicity [49].

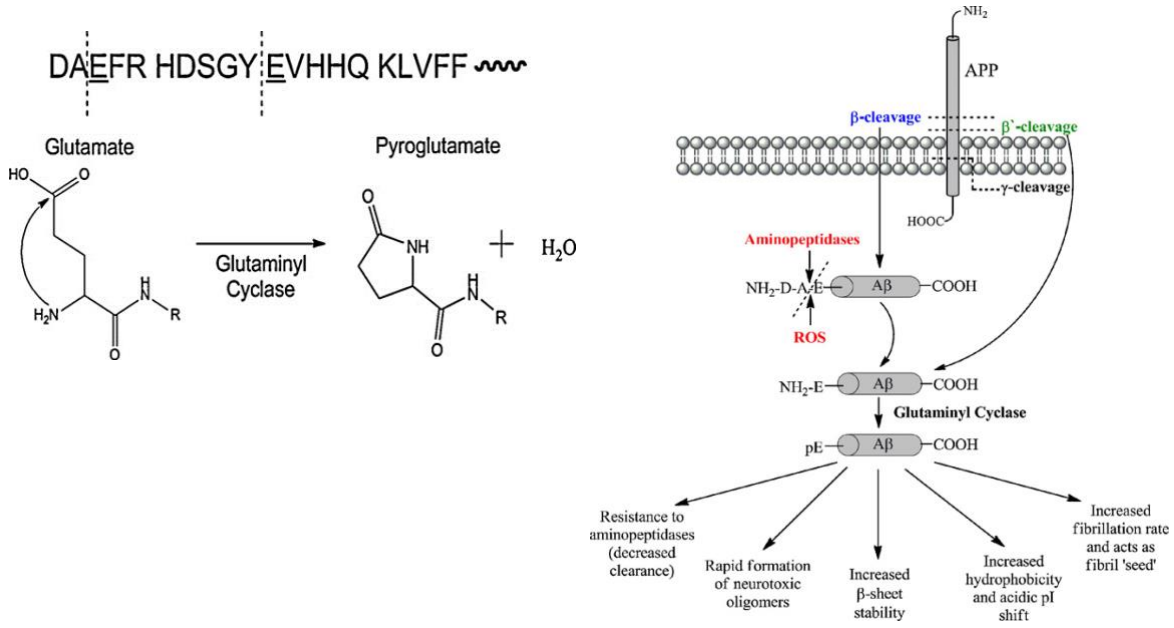

Figure 1. 2: **(**Left) N- truncations can generate Aβ peptides with exposed glutamate at position 3 or 1. Aβ peptide sequence is shown for the first 20 residues. Glutaminyl cyclase (QC) converts exposed glutamate residues to the more hydrophobic and aminopeptidase resistant pyroglutamate residue. (Right) Schematic representation of pE-Aβ formation and the resulting biophysical and biochemical effects. Multiple potential mechanisms for Aβ N-terminal truncation have been proposed—the exact mechanism could involve one or more of these pathways or a yet unidentified cleavage process. Source: Gunn et al. [46].

Circular dichroism (CD) data showed that in trifluoroethanol (TFE)/water (1:5, v/v) mixture, pEA$\beta_{3\text{-}40}$ displayed an increased β-sheet propensity while A$\beta_{1\text{-}40}$ formed α-helical structure [50]. In addition, thioflavin-T (ThT) fluorescence assay identified typical sigmoidal aggregation kinetics for pEA$\beta_{3\text{-}40}$ whereas A$\beta_{1\text{-}40}$ showed no ThT signal, indicating resistance to fibrillogenesis. Transmission electron microscopy (TEM) identified β-sheet-rich fibrils for pEA$\beta_{3\text{-}40}$. Finally, NMR data showed significant structural differences in the N-terminal regions

of $A\beta_{1-40}$ and $pEA\beta_{3-40}$, which decreases monomer stability of the latter peptide and promotes cross β-sheet fibril formation.

By performing the analysis of senile plaques, the aggregated individual pEAβ and unmodified Aβ as well as their heterogeneous intermixed were found.[51] further study had shown that the immunohistochemical examination of postmortem brains of different ages revealed that plaques in brains of younger subjects contained mostly pEAβ, and the ratio Aβ/pEAβ increased with age, suggesting that deposition of pEAβ leads that of the Aβ.[51] The pEAβ load in postmortem human brains correlated with hyperphosphorylated tau protein and predicted AD better than unmodified Aβ.[52] Harigaya et al. had shown that even though the $pEA\beta_{3-42}$ was a major component of senile plaques in AD brains (25% of total $A\beta_{1–42}$), $pEA\beta_{3-40}$ formed deposits mainly in the cerebral vasculature.[52]

Wulff et al. [53] demonstrated that AβpE has higher susceptibility to mechanical stress and fragmentation of the fibrils. This report has been challenged by other studies, arguing that pE-Aβ assemblies have similar content of β -sheet structure, are more resistant to fibrillogenesis [55-57], and exert cytotoxic effect similar to unmodified Aβ [54,56,57].

The structure, aggregation and neurotoxicity of a peptide affected strongly by N-terminal pyroglutamylation. In murine brains, $pEA\beta_{3-40}$ inhibited hippocampal long-term potentiation [58]and utilized stronger cytotoxic effect on cultured rat hippocampal neurons than $A\beta_{1-40}$, $A\beta_{1-42}$, and even $pEA\beta_{3-42}$.[59] The molecular basis of the greater toxicity of pEAβ remains obscure. Whereas in some studies have shown that the aggregation into β-sheet-rich assemblies for $pEA\beta_{3-40}$ more readily than $A\beta_{1-40}$,[47,48,50] others have found similar toxicities[60] and structural features of unmodified and pyroglutamylated Aβ peptides in fibrillar or oligomeric states[61] and lengthier aggregation of pEAβ,[62] leaving the issue unclear.

The structural and aggregation properties of unmodified Aβ and pE-Aβ are important for their respective cytotoxic effects. However, these biophysical characteristics have not been firmly established. Therefore, the main focus of this project is on comparative characterization of aggregation and accompanying structural changes of $A\beta_{1-40}$ and $pEA\beta_{3-40}$ separately and in combination.

In addition, smaller fragments of Aβ have studied in this project in order to identify the specific regions of the peptide initiating α-helix to β-sheet transition, aggregation, and fibril formation. Several studies performed experiments use peptide fragments related or unrelated to Aβ sequence to inhibit Aβ aggregation and hinder Aβ-induced cytotoxicity. [63-75] The peptide fragment's inhibitory effect on Aβ aggregation and toxicity originates from their capacities to intercalate into Aβ assemblies and prohibit the formation of toxic oligomers, which may or may not be associated with their own self-aggregation propensities. Therefore, a mutated peptide, KLVFWAK, imitating the $A\beta_{16-22}$ (KLVFFAE) which had minimal self-aggregation propensity but favorably interrelated with oligomeric and fibrillar structures of Aβ.[76] On the other hand, the natural sequence of $A\beta_{16-22}$ has been known as a fibrillogenic segment that forms antiparallel β-sheet aggregates stabilized by ionic interactions between terminal side chains and nonpolar interactions between internal hydrophobic residues. [77,78] Cheng et al. [69] had shown that $A\beta_{16-22,}$ among several Aβ segments integrated in a full-length peptide, inhibited $A\beta_{1-40}$ aggregation and cytotoxicity. These effects were inferred in terms of binding of the fragment peptide to Aβ oligomers and inhibition of fibril nucleation. Simultaneously, the same $A\beta_{16-22}$ peptide, as well as the hydrophobic C-terminal stretch from Lys_{28} onward, were established to be the most fibrillogenic regions in the perspective of several Aβ species containing 38 to 43 amino acids. [84] Coherent with these outcomes, the peptides $A\beta_{28-42}$ and $A\beta_{29-42}$ exhibited fast

aggregation and β-sheet fibril formation propensities contrasting some other C-terminal Aβ peptide fragments. [83] Furthermore, midst twelve C-terminal $A\beta_{1-42}$ fragments $A\beta_{28-42}$ exerted extreme toxic effect on cultured PC-12 cells [83] and insinuated correlation between amyloidogenicity and toxic effects of the peptides. Additionally, by interfering with formation of toxic oligomers two C-terminal fragments, $A\beta_{31-42}$ and $A\beta_{39-42}$, were capable to rescue neuronal cells from $A\beta_{1-42}$ cytotoxicity [79].

Therefore, by direct interaction with full-length peptide Aβ fragments of Aβ appear to affect the aggregation and toxicity of full-length one. Reports on the aspects of binding of fragments to the full-length peptide exposed various modes of interaction. The study of Aβ fragment $A\beta_{33-37}$ (GLMVG) shown that it binds with C- terminus of $A\beta_{1-42,}$ probably the homologous sequence, and suppress its aggregation, neuronal membrane damage and synaptotoxicity [70]. Surprisingly, another short C-terminal fragment, $A\beta_{39-42}$, favorably interrelated with the N-terminus of $A\beta_{1-42}$ in oligomeric form [80-82]. The aforementioned mutated peptide, KLVFWAK, also interacted in a non-homologous manner with the C-terminus of Aβ aggregates [76].

These outcomes suggest that Aβ aggregation can be essentially modulated by Aβ-derived peptide fragments. Nevertheless, a comprehensive understanding of the variant effects of Aβ segments along the whole $A\beta_{1-42}$ sequence has not been attained. This work aimed at systematic studies on 10 amino acid residue long overlapping fragments of $A\beta_{1-42}$ to understand their intrinsic β-sheet formation and fibrillogenesis properties and their effects on same properties of the parent peptide. Here structural and aggregation properties of the parent $A\beta_{1-42}$ peptide and

seven overlapping peptide fragments have been studied, i. e. $A\beta_{1-10}$ (P1), $A\beta_{6-15}$ (P2), $A\beta_{11-20}$ (P3), $A\beta_{16-25}$ (P4), $A\beta_{21-30}$ (P5), $A\beta_{26-36}$ (P6), and $A\beta_{31-42}$ (P7).

1.3 Protein Structure

The protein structure is the three-dimensional arrangement of atoms in the amino acid chain molecule. Proteins are polymers, which are formed by amino acid sequences. A single amino acid monomer can also be referred to as a residue implying a repeating unit of the polymer. Proteins are formed by amino acids that undergo condensation reactions, where the amino acids lose one water molecule each time they react and are connected to each other through peptide bonds. By convention, chains of less than 30 amino acids are usually identified as peptides, not proteins.

In order to perform its biological functions, proteins are driven by a series of non-covalent interactions (such as hydrogen bonds, ionic interactions, van der Waals forces, and hydrophobic packaging) to fold into one or more specific spatial conformations. To understand the functions of proteins at the molecular level, it is often necessary to determine their three-dimensional structure. This is the subject of structural biology science, which uses techniques such as Fourier Transform Infrared (FTIR) spectroscopy, Circular dichroism (CD), X-ray crystallography, nuclear magnetic resonance spectroscopy, cryo-electron microscopy (cryoEM), and dual polarization interferometry to define the structure of proteins.

The size of the protein structure varies from dozens to thousands of amino acids. According to their physical size, proteins are classified as nanoparticles, between 1 and 100 nm. Very large protein complexes can be formed from protein subunits.

The primary structure of a protein indicates to the sequence of amino acids in the polypeptide chain. The primary structure is held together by peptide bonds formed during protein

biosynthesis. According to the nature of the free groups at both ends, the ends of the polypeptide chain are called carboxyl terminus (C-terminus) and the amino terminus (N-terminus) respectively. The residue count always starts from the N-terminal end (NH_2- group), which is the end where the amino group does not participate in the peptide bond. The primary structure of a protein is determined by the gene for the protein. A specific sequence of nucleotides in DNA is transcribed into mRNA, which the ribosome reads in a process called translation. The sequence of the protein is unique to the protein and defines the structure and function of the protein. The sequence of the protein can be determined by methods such as tandem mass spectrometry. However, it is usually read directly from the gene sequence using the genetic code. It is strictly recommended to use the term "amino acid residues" when talking about proteins, because when a peptide bond is formed, a water molecule is lost, so proteins are composed of amino acid residues. Post-translational modifications such as phosphorylation and glycosylation are usually considered part of the primary structure and cannot be read in genes.

The next level of protein structure, the secondary structure, indicates to the partially folded structure formed in the polypeptide due to the interaction between the backbone atoms. (The main chain refers only to the polypeptide chain other than the R group; the secondary structure does not include the R group atoms.) The most common types of secondary structure are α- helices and β-sheets. Both structures maintain their shape through hydrogen bonds, which are formed between the carbonyl C=O of one amino acid and the amide NH of the other amino acid.

In the α-helix, the carbonyl group (C = O) of the amino acid forms a hydrogen bond with the amino group H (N-H) of the 4 amino acids in the chain. This bonding pattern draws the polypeptide chain into a helical structure that resembles a curled ribbon, each turn of the spiral

containing 3.6 amino acids. acid. The R groups of amino acids protrude from the alpha helix, where they can interact freely.

In β-sheets, two or more segments of the polypeptide chain are arranged next to each other to form a sheet-like structure, which is held together by hydrogen bonds. A hydrogen bond is formed between the carbonyl group and the amino group of the skeleton, and the R group extends above and below the plane of the sheet. The strands of the folded sheet β can be parallel, pointing in the same direction (meaning that its N- and C-termini coincide), or anti-parallel, pointing in the opposite direction (meaning that the N-terminus of one strand is positioned next to the C-terminus of the other). Some amino acids are more or less likely to appear in alpha helices or beta sheets. For example, the amino acid proline is sometimes called a "helix breaker" because its unusual R group (attached to an amino group to form a ring) creates a bend in the chain and is incompatible with helix formation. Proline is generally found in curved, unstructured regions between secondary structures. Similarly, amino acids with a large ring structure in the R group, such as tryptophan, tyrosine, and phenylalanine, are often found in β sheets, which may be because the β sheet structure provides sufficient side chains.

The general three-dimensional structure of a polypeptide is called the tertiary structure. The tertiary structure is mainly due to the interaction between the R groups of the amino acids that make up the protein. The R group interactions that contribute to the tertiary structure include hydrogen bonds, ionic bonds, dipole-dipole interactions, and London dispersion forces - basically the full range of non-covalent bonds. For example, R groups with the same charge repel each other, while groups with opposite charges can form ionic bonds. Similarly, polar R groups can form hydrogen bonds and other dipole-dipole interactions. Also important for tertiary structure is hydrophobic interaction, in which amino acids with nonpolar hydrophobic R groups

are brought together inside the protein, while hydrophilic amino acids are left outside to interact with surrounding water molecules. Ultimately, there is a special type of covalent bond that promotes the tertiary structure: disulfide bonds. Disulfide bonds, the covalent bonds between the side chains of sulfur-containing cysteine, are much stronger than other types of bonds that contribute to the tertiary structure. They act as molecular "safety pins", making the various parts of the polypeptide firmly connected to each other

Many proteins are composed of a single polypeptide chain and only have a tertiary structure. However, some proteins are made up of multiple polypeptide chains, also called subunits. When these subunits are grouped together, they give the protein a quaternary structure.

An example of a protein with a quaternary structure: hemoglobin. Hemoglobin carries oxygen in the blood and is composed of four subunits, two for each type α and β. Another example is DNA polymerase, an enzyme that synthesizes new DNA strands, composed of ten subunits.

Generally speaking, the same types of interactions that contribute to the formation of tertiary structures (mainly weak interactions, such as hydrogen bonds and London scattering forces) also combine subunits to form quaternary structures.

1.4 Protein-Protein Interaction

Protein-protein interaction (PPI) deals with a wide range of biological processes, including cell-cell interactions and developmental and metabolic control. Protein-protein interaction is becoming one of the main objectives of systems biology. Non-covalent contact between the side chains of the residues is the basis for protein folding, protein assembly, and PPI. These contacts induce various interactions and associations between proteins. According to its comparative structural and functional characteristics, PPI can be classified in a variety of

ways. Based on their interaction surface, they can be homologous or heterogeneous; from their stability, they may or may not be obligated; in terms of their persistence, they can be temporary or permanent. The given PPI can be a combination of these three specific pairs. Transient interactions will form signal pathways, while permanent interactions will form stable protein complexes.

Generally, proteins rarely act as isolated species when they perform their functions in vivo. It has been found that more than 80% of proteins do not act alone but in the form of complexes. An extensive analysis of validated proteins showed that proteins involved in the same cellular process were repeatedly found to interact with each other. The study of PPI is also important for inferring the function of proteins in cells. The function of unknown proteins can be predicted from the evidence of their interaction with the protein, and the function of the protein has been revealed. The detailed study of PPI has accelerated the modeling of functional pathways to illustrate the molecular mechanisms of cellular processes. Characterizing the interactions of proteins in a given proteome is very useful for revealing the biochemistry of cells. There are many ways to determine the result of two or more proteins interacting with a defined functional target. Phizicky and Fields have outlined the important characteristics of PPI. [151] PPIs can change the kinetic properties of enzymes; as a general mechanism to allow the substrate to pass through; it constructs new binding sites for small effector molecules; Inactivate or inhibit proteins; Change the specificity of the protein to its substrate through interaction with different binding partners; Play a regulatory role at the upstream or downstream level.

Revealing information about protein-protein interaction can help determine drug targets. Studies have shown that proteins with a large number of interactions (centers) can include families of enzymes, transcription factors, and inherently disordered proteins [152,153].

However, the PPI involves more heterogeneous processes, and its regulatory scope is greater. To understand its importance in cells more precisely, it is necessary to identify various interactions and determine the consequences of the interactions.

1.5 Protein Solubility

Protein solubility is a thermodynamic parameter defined as the concentration of protein in a saturated solution that is in equilibrium with a solid phase, either crystalline or amorphous, under a given set of conditions. Depending on pH conditions, proteins can be positively charged (cations) or negatively charged (anions). When the positive and negative charges on the protein are equal, the net charge is zero. The characteristic pH value of the solution when the net charge of the protein is zero (the positive and negative charges are equal) is defined as the isoelectric point (pI). Under conditions of pH below its isoelectric point, the protein will carry a net positive charge and will behave as a cation. At a pH above its isoelectric point, the protein will have a net negative charge. The isoelectric point of a protein is an important characteristic, because at this point the solubility of the protein is lowest and therefore unstable. It should be noted that proteins are soluble below and above the isoelectric point (pI).

Salt bridges are ionic bonds between positively charged and negatively charged amino acid side chains. An example is the attraction between the $-COO^-$ ion of glutamic acid and the NH^{+3} ion of lysine. Increasing the pH by adding a base will convert NH^{+3} ions into neutral NH_2 groups. Lowering the pH by adding acid will convert $–COO^-$ ions into neutral COOH groups. In each case, the ionic attraction disappears, and the shape of the protein unfolds. Additionally, salt concentration (ionic strength) is also very important for protein solubility. At low salt concentrations protein solubility increases and at high salt concentration protein solubility decreases.

1.6 Basic Aspects in Protein Stability

The influence of salt on the structure and function of non-halophilic proteins has been well resolved. The presence of high salt content in the protein solution will have the following effects: interference of the local water structure around the protein; reduction of the tendency of intermolecular hydrogen bonds to affect the solubility, binding, stability and crystallization of the protein; Increase the surface tension of water, striping off the essential water layer from the protein surface and increase the hydrophobic interaction, which leads to the aggregation and precipitation of proteins. However, a high concentration of salt can adversely affect the structure of proteins and their subsequent function.

Protein denaturation refers to the loss of biological activity caused by changes in protein structure caused by physical or chemical factors such as pH, temperature, salt, detergents, organic solvents, or chaotropic agents. Secondary, tertiary, or quaternary structure is greatly affected by denaturation. Some important mechanisms of protein denaturation are (http://class.fst.ohio-state.edu/FST822/lectures/Denat.htm):

- High temperature weakens the inherent bonds in proteins. The additional heating will destroy the hydrogen bonds in the protein and establish new hydrogen bonds with the surrounding water molecules, thus destroying the helical structure.
- Water miscible solvent (less polar than water) reduce the dielectric constant of the system, thus strengthening electrostatic interactions between molecules. The protein unfolds to a great extent, exposing the hydrophobic group to the solvent, leading to aggregation and precipitation.

- Proteins are usually more soluble in dilute salt solutions because the salts in their ionic forms associate with opposite charges within the protein moiety, leading to increased hydration of the surface. However, at very high salt concentration, the increased surface tension of water generates a competition between protein and salt ions for hydration. Salts strip off the essential layer of water molecules from the protein surface eventually denaturing the protein.

- Protein denaturation caused by urea can occur through direct or indirect mechanisms. Urea can directly interact with the protein through the hydrogen bond with the polarized region of the protein surface, weakening the intermolecular bond and structure of the protein. Guanidine hydrochloride (GdmCl) has a similar mechanism, but it is a more effective denaturant than urea. In an indirect mechanism, urea can change the structure of water and cause protein instability.

CHAPTER 2: RESEARCH STRATEGY

2.1 Fourier Transform Infrared (FTIR) Spectroscopy

For identification and analysis of structure of chemical compound, mid-infrared (IR) spectroscopy is a well-establish technique. The excitation of vibrational modes of the molecules in the sample and the association with other chemical bonds and functional groups in the molecules are represented the various peaks in the IR spectrum. Therefore, the infrared spectrum of a compound is one of its most characteristic physical properties and can be regarded as its "fingerprint".

The molecular absorption of electromagnetic radiation in the infrared region of the spectrum (Figure 2.1) promotes the transition between the rotational energy level and the vibratory energy level of the electronic energy state of the ground (lower). This is in contrast to the more energetic absorption of visible and ultraviolet radiation, which causes the transition between the energy levels of vibration and rotation of different electronic energy state. Infrared spectroscopy mainly involves molecular vibrations, because the transition between individual rotational states can only be measured in the infrared spectra of small molecules in the gas phase.

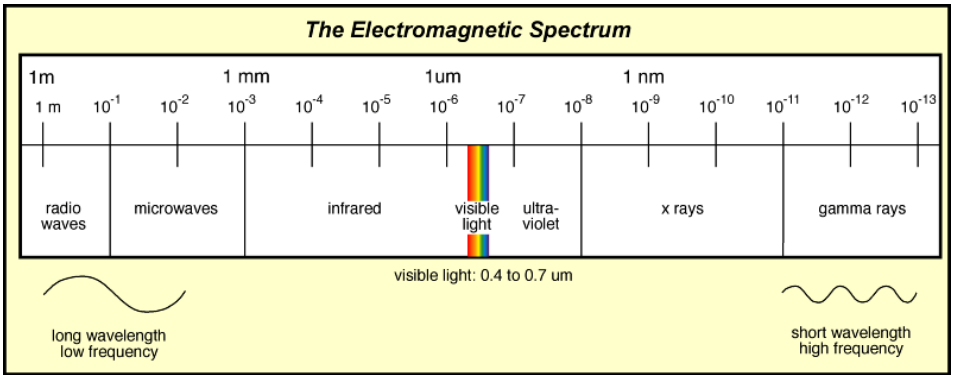

Figure 2. 1: The regions of the electromagnetic spectrum.

A nonlinear molecule composed of N atoms is said to have 3N degrees of freedom, because if the position of each atom is described by three coordinates (for example, x, y, z in the Cartesian coordinate system), then the position, shape and the orientation of the molecules in three-dimensional space will be completely defined. Since a total of three coordinates are required to describe the translation of the molecule (for example, along the x, y, and z axes), the molecule has three translational degrees of freedom. The other three degrees of freedom represent the rotation of the molecule around three axes. The remaining 3N-6 degrees of freedom correspond to vibratory motion, and the molecule is said to have normal 3N-6 modes of vibration. These vibration modes can be described by bond stretching and various types of bending vibrations (see Figure 2X). In the case of linear molecules, there are only two rotational degrees of freedom, because rotation around the bond axis is impossible. Therefore, linear molecules have a normal vibration mode of 3N-5.

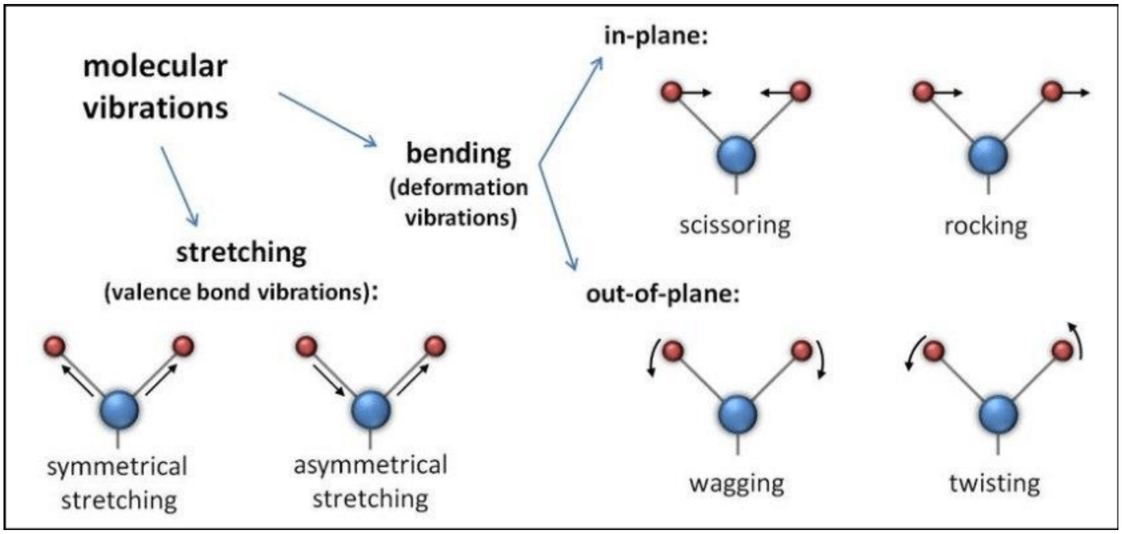

Figure 2. 2: Visualization of all different molecular vibrations, arrows indicate movements resulting from repulsion caused by electronegativity. Specific molecules move on a specific frequency, which absorbs energy when it equals light frequencies (source: USDA)

Therefore, a simple diatomic molecule A-B has (3 x 2) − 5 = 1 vibration mode, which corresponds to stretching with the A-B bond. This stretching vibration is similar to the vibration of two objects connected by a spring. Hence, in the first approximation, the harmonic oscillator model can be used to describe this vibration, and then the restoring force (F) on the bond is given by Hooke's law:

$$F = -kx \quad \dots (1)$$

where k is the force constant of the bond, and x is the displacement.

In this approximation, the vibrational frequency ν is given by:

$$\nu = \left(\frac{1}{2\pi}\right)\left(\frac{k}{\mu}\right)^{1/2} \quad \dots (2)$$

with μ is the reduced mass of the system,

$$\mu = \frac{m_A . m_B}{m_A + m_B} \quad \ldots (3)$$

where m_A and m_B are the individual atomic masses of A and B.

The unit of frequency (ν) is reciprocal seconds (sec^{-1}). However, by convention, band positions in infrared spectra are given in wavenumbers ($\overline{\nu}$), expressed in units of reciprocal centimeters (cm^{-1}), and are often termed "band frequencies." In older literature, band positions are often reported in units of wavelength (λ), The relation between these units is given by equations (4) and (5):

$$\overline{\nu} = \frac{1}{\lambda} \quad \ldots (4)$$

$$\nu = \frac{c}{\lambda} \quad \ldots (5)$$

where c = velocity of light.

The situation for a many-atom molecule is more complicated than equation (2) because the measured vibrational frequencies do in general, correspond to mixtures of different vibrations rather than pure vibrations. Additionally, electrical effects, steric effects, the nature, size and electronegativity of neighboring atoms, phase changes and hydrogen bonding may all cause shifts in frequency. Instead, the above process is the basis of the group frequency concept. According to this concept, it is expected to show a characteristic absorption frequency that can establish from the IR spectrum that various functional groups are present in the compound.

The quantum mechanical treatment of molecular vibration leads to the modification of the harmonic oscillator model. Although the above treatment of Hooke's law shows the continuity of the vibrational states, the molecular vibrational energy levels are quantized:

$$E = \left(n + \frac{1}{2}\right) h\nu \quad \ldots\ldots (6)$$

where h is Planck's constant, n is the vibrational quantum number, and ν is the fundamental vibrational frequency.

Therefore, only when the frequency is consistent with the frequency of one of the basic vibration modes of the molecule, the molecule will absorb infrared radiation of a specific frequency. It can be seen from equation (6) that in the harmonic oscillator approximation, quantum mechanical processing predicts equidistant vibration energy levels. It also predicts that at room temperature, only the transition from the ground state vibrational energy level (n = 0) to the first excited vibrational energy level (n = 1) will occur. However, through experiments, harmonic bands are observed, corresponding to the transition to higher vibration levels, and their frequencies are slightly lower than integer multiples of the fundamental vibration frequency. These effects are due to the anharmonic nature of molecular vibrations. Anharmonicity also produces a combining band, which represents the simultaneous excitation of two fundamental vibration modes. The harmonic and combined bands, which are "forbidden" bands, are about an order of magnitude weaker than the basic mode. Near infrared (NIR) spectroscopy involves the study of such bands in the near infrared region of the spectrum (12800-4000 cm^{-1}).

Lastly, it is significant to note that all molecular vibrations will not produce infrared absorption bands. Only when the excitation of this vibration causes the dipole moment of the molecule to change, the fundamental vibration mode will be "active IR". Therefore, N_2, O_2, and other homonuclear diatoms will not produce IR absorption bands. Correspondingly, the symmetric

stretching of linear X-Z-X molecules (see Figure 2) (like CO_2) will not be an active infrared vibration. Additionally, the symmetry of the molecule influences the number of absorption bands that will appear in its infrared spectrum. For example, due to molecular symmetry, when two vibrations have the same energy (degenerate vibration), they will produce a single IR absorption band. The expectation of the number of bands observed in the infrared spectrum of molecules based on molecular structure and symmetry is the domain of group theory.

FTIR is widely used in biophysical/structural characterization of biomolecules. Specific spatial arrangements of atoms in defined secondary structural geometries, which are stabilized by hydrogen bonding of certain strength that is inversely proportional to covalent bond strength, produce absorption bands at characteristic frequencies. This allows one to evaluate the molecule's overall secondary structure by analysis of the spectrum. Proteins generate a number of "amide" bands, of which the amide I band, a composite vibrational mode involving mostly the C=O stretching vibration, is the most conformation-sensitive feature. For example, α-helix and β-sheet structures generate absorption bands around 1655 cm^{-1} and 1630 cm^{-1} [85], so an α / β protein will produce an amide I band with two major components at these wavenumbers, and its structure can be determined from the relative weights of these components, with correction for respective extinction coefficients. FTIR spectroscopy, along with some other spectroscopic methods such as circular dichroism, are considered "low resolution" techniques. These techniques provide the global structure of proteins bot not the precise 3-dimensional structure at an atomic level, unlike some other methods such as X-ray crystallography and NMR. The advantage of these "low resolution" methods is their accessibility, which allows collection of valuable structural information in a short time (~1 hour), using tiny amounts (~0.01-0.1 mg) of sample. In addition, proteins are studied in their natural milieu, i.e. an aqueous environment,

rather than crystals or organic solvents. FTIR is practically free of light scattering problems because of the long wavelengths, and is not restricted by the protein size, like NMR [86]. In addition, membrane proteins, which are very difficult to crystallize, are being easily studied by FTIR, using either lipid vesicle-reconstituted proteins or by attenuated total reflection FTIR on proteins embedded in supported membranes. Sine FTIR measurements are conducted in D_2O-based buffers (H_2O absorbs in the amide I region), solvent exposure of the protein interior upon structural changes or unfolding results in amide hydrogen exchange (NH to ND), which downshifts the amide II band by ~100 cm^{-1}, from 1540 cm^{-1} to 1440 cm^{-1}. This allows evaluation of the tertiary structural changes in proteins by following the kinetics of amide hydrogen exchange.

2.2 Circular Dichroism (CD) Spectroscopy

CD is electronic spectroscopy based on chirality of molecules. Since amino acids contain a C_α chiral atom (except for glycine), CD is widely used in structural studies of proteins [65-67]. CD spectroscopy is used extensively to study chiral molecules of all types and sizes, but it is in the study of large biological molecules where it finds its most important applications.

A chromophore that is asymmetric in nature or a symmetrical chromophore in an asymmetric environment will interact differently with left and right circularly polarized light, resulting in two related phenomena. Since the refractive index of right circularly polarized light and left circularly polarized light are different, circularly polarized light will pass through the optically active medium at different speeds, which is called optical rotation or circular birefringence. The change in optical rotation as a function of wavelength is called optical rotation dispersion (ORD). Due to the different extinction coefficients of the two polarized light called circular

dichroism (CD), left and right circularly polarized light will also be absorbed to different degrees at certain wavelengths. Optical rotating scattering allows chiral molecules to rotate the plane of polarized light. The ORD spectrum is dispersive (called the single band's cotton effect), while the circular dichroic spectrum is absorbent. These two phenomena are related to the so-called König -Kramers transformation.

It can be exhibited that if right- and left-handed circularly polarized light is absorbed to different degrees at any wavelength, there will be a difference in refractive index at almost all wavelengths. ORD scattering is also the reason why CD is a more sensitive analytical technique. Unlike the dispersive ORD phenomenon, circular dichroism can only occur in the normal absorption band and therefore requires inherent asymmetric chromophores (uncommon) or symmetric chromophores in asymmetric environments.

Electromagnetic radiation consists of an electric (E) and magnetic (B) field that oscillate perpendicular to one another and to the propagating direction, a transverse wave. While linearly polarized light occurs when the electric field vector oscillates only in one plane, circularly polarized light occurs when the direction of the electric field vector rotates about its propagation direction while the vector retains constant magnitude. At a single point in space, the circularly polarized vector will trace out a circle over one period of the wave frequency, hence the name. The two diagrams below (Figure 2.3) show the electric field vectors of linearly and circularly polarized light, at one moment of time, for a range of positions; the plot of the circularly polarized electric vector forms a helix along the direction of propagation (k). For left circularly polarized light (LCP) with propagation towards the observer, the electric vector rotates

counterclockwise. For right circularly polarized light (RCP), the electric vector rotates clockwise.

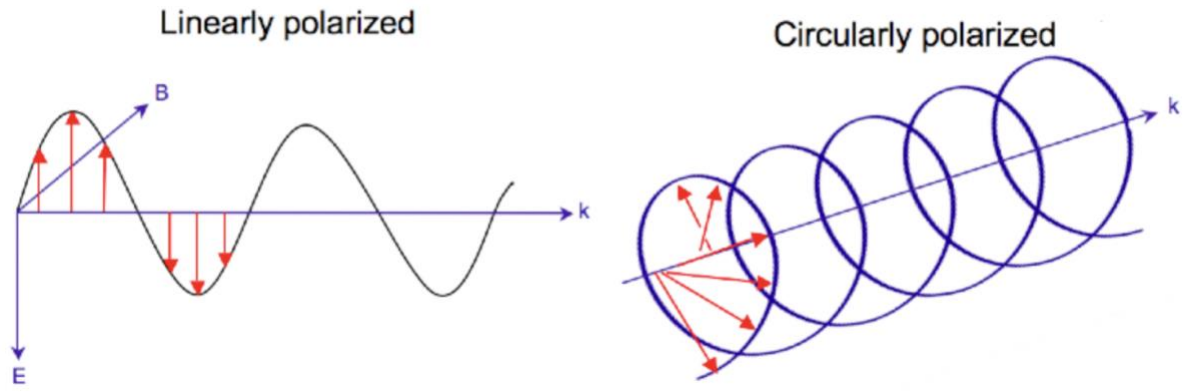

Figure 2. 3: Linearly (left) and circularly (right) polarized light.

The different absorption of radiation polarized in two directions as a function of frequency is called dichroism. When applied to plane polarized light, this is called linear dichroism; for circularly polarized light, circular dichroism. The linearly polarized light is the result of two of equal amplitude opposite circular polarizations. After passing the optically active sample, the circularly polarized light will change in two ways. These two components are still circularly polarized, but the size of the E component that rotates in the opposite direction will no longer be the same, because the molar extinction coefficients of the left polarized light and the right polarized light are not equal. The E-vector direction no longer draws a circle but an ellipse (actually an elliptical spiral, if not limited to projection) due to the difference in refractive index, the major axis of the ellipse will also rotate.

Generally, ellipticity is a unit of circular dichroism, defined as the tangent of the ratio of the minor axis to the major axis of the ellipse axis. An axial ratio of 1:100 will result in an ellipticity of 0.57 degrees. Modern CD instruments have millisecond accuracy. Although CD is now

measured as the difference in absorbance of left and right circularly polarized light as a function of wavelength, the unit ellipticity still exists. Each type follows Lambert Beer's law, so the difference in extinction coefficient (left and right) at a given wavelength is equal to the difference in absorbance divided by the product of optical path length and concentration.

CD instruments (known as spectropolarimeters) measure the difference in absorbance between the L and R circularly polarized components ($\Delta A = A_L - A_R = (\epsilon_L - \epsilon_R)lc$), where the subscripts R and L signify right and left polarization, *l* is the optical pathlength (thickness) of the sample, and *c* the solute concentration. Differential absorption of right- and left- polarized lights results in conversion of a plane-polarized light into elliptically polarized light (note that the plane-polarized light can be presented as a sum of right- and left-polarized components of equal amplitudes). The ellipticity (θ), is simply the ratio of the minor and major semiaxes of the ellipse (Figure 2.4).

$$\tan\theta = \frac{r_{minor}}{r_{major}} = \frac{E_L - E_R}{E_L + E_R}$$

For small θ, $\tan\theta = \theta$

It can be shown that, $\theta\ (deg) = 180 \times \ln 10 \times \frac{\Delta A}{4\pi} = 32.98\ \Delta A$

In practice, the molar ellipticity is used: $[\theta] = 100\ \theta\ /cl = 3298 \Delta\epsilon$

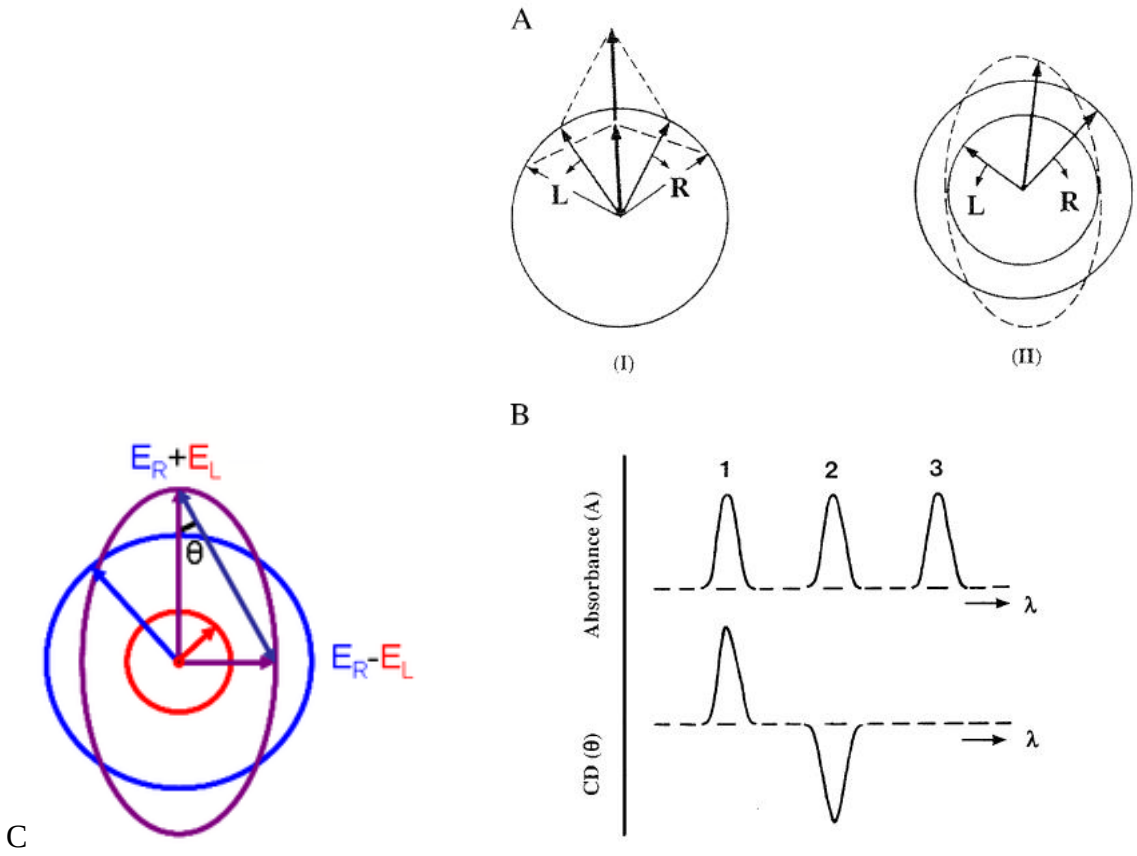

Figure 2. 4: Origin of the CD effect. (A) The left (L) and right (R) circularly polarized components of plane polarized radiation: (I) the two components have the same amplitude and when combined generate plane polarized radiation; (II) the components are of different magnitude and the resultant (dashed line) is elliptically polarized. (B) The relationship between absorption and CD spectra. Band 1 has a positive CD spectrum with L absorbed more than R; band 2 has a negative CD spectrum with R absorbed more than L; band 3 is due to an achiral chromophore. (C) Elliptical polarized light (violet) is composed of unequal contributions of right (blue) and left (red) circular polarized light.

n-π^* transitions involve moving an electron from a nonbonding electron pair to a antibonding π^* orbital. They tend to have molar absorbtivities less than 2000 and undergo a blue shift with solvent interactions (a shift to higher energy and shorter wavelengths). This is because the lone

pair interacts with the solvent, especially a polar one, such that the solvent aligns itself with the ground state. When the excited state emerges, the solvent molecules do not have time to rearrange in order to stabilize the excited state. This causes a lowering of energy of the ground state and not the excited state. Because of this, the energy of the transition increases, hence the "blue shift". The n-π^* transition in peptides occurs at 210-225 nm ($\epsilon \approx 100$ M^{-1} cm^{-1}). The strong band responsible for the absorbance of most peptide bonds is the π-π^* transition. The π-π^* transitions involve moving an electron from a bonding $\pi\pi$ orbital to an antibonding $\pi^*\pi^*$ orbital. They tend to have molar absorptivities on the order of 10,000 and undergo a red shift with solvent interactions (a shift to lower energy and longer wavelengths). This could either be due to a raising of the ground state energy or lowering of the excited state energy. If the excited state is polar, then it will be solvent stabilized, thus lowering its energy and the energy of the transition. Using CD, these different transitions are more distinctly evident. The two types of π-π^* transitions occur around 210 and 190 nm ($\epsilon \approx 7{,}000$ M^{-1} cm^{-1}).

A CD spectrum of a protein is usually measured in the 180 nm to 350 nm ultraviolet (UV) region. The far-UV signal between 180 and 250 nm is sensitive to protein's secondary structure. The α-helical structure produces two minima around 208 and 222 nm and a maximum around 192-195 nm, and β-sheet structure generates a minimum at 216 nm and a maximum around 195 nm [68, 69]. Unordered proteins produce a weak maximum around 220 nm and a deep minimum around 195-200 nm [68, 69]. The CD signal in the near-UV region (~ 280 nm) is generated by the side chains of aromatic amino acids (Trp, Tyr, Phe) that "borrow" dichroic properties from the nearby backbone C_α atoms. It is often used to characterize the protein's tertiary structure, the signal increases with increasing compactness of the protein's fold. CD thus can be used to observe how the secondary and tertiary structures of a protein or peptide change with

environmental conditions (pH, temperature, salt concentration) or upon interaction with other molecules. Structural, kinetic and thermodynamic information about macromolecules can be derived from circular dichroism spectroscopy.

2.3 Fluorescence Spectroscopy (FS)

FS is electronic spectroscopy that is based on light absorption and emission by certain molecules. The incident light, usually in the UV or visible regions, is absorbed by electronic transition from the ground state to the higher energy excited state. Both ground and excited states have many vibrational energy levels that are spaced more closely compared to the energy difference between the ground and excited levels. The excited electron loses some of its energy by adopting the lowest vibrational level. Before returning, the electron also loses some of its energy by various mechanisms, mostly by "solvent relaxation", i.e. reorienting the polar solvent molecules, such as H_2O. Then, within about 10 ns, the electron returns to the ground state, emitting light. Through the aforementioned mechanisms, the emitted light carries less energy and thereby the emission occurs at longer wavelengths than the excitation (Stokes shift) [92]. As molecules may drop down into any of several vibrational levels in the ground state, the emitted photons will have different energies, and thus wavelengths, producing an emission band with nearly Gaussian distribution of intensities.

Best known fluorescent organic molecules are the aromatic rings. Three out of twenty amino acids found in proteins, i.e. tryptophan (Trp), tyrosine (Tyr), and phenylalanine (Phe), have such rings and therefore are intrinsically fluorescent. The location of the emission band relative to the excitation along the wavelength axis indicates how strong the solvent relaxation is. Stronger solvent relaxation occurs for proteins with more open, solvent accessible tertiary

structure, which is manifested by a higher emission wavelength (red shift). Proteins with more compact tertiary structure display emission at shorter wavelength (blue shift), closer to the excitation wavelength. Thus, FS is sensitive to protein's tertiary structure, and together with CD is used for comprehensive structural characterization of proteins.

2.4 Peptide Preparation

2.4.1 Preparation for Structure and Aggregation of Aβ1-40 and Pyroglutamylated pEAβ3-40 Separately and Combined.

Synthetic $A\beta_{1-40}$ and $pEA\beta_{3-40}$ peptides were purchased from Innovagen (Lund, Sweden). Recombinantly expressed, uniformly 13Clabeled $A\beta_{1-40}$ was from rPeptide (Watkinsville, GA, USA). All peptides were ≥98% pure as confirmed by HPLC and mass spectrometry. Salts, buffers, hexafluoroisopropanol (HFIP), ThT, and other chemicals were from Fisher Scientific (Hanover Park, IL, USA) or Sigma-Aldrich (St. Louis, MO, USA). Quartz cuvettes for CD and fluorescence measurements were purchased from Starna Calls, Inc. (Atascadero, CA, USA). CaF2 FTIR windows were from Buck Scientific (East Norwalk, CT, USA). D2O (99.8% pure) was from Cambridge Isotope Laboratories (Andover, MA, USA).

The lyophilized peptides were dissolved in HFIP at total peptide concentration of 50 μM, and CD spectra were monitored and measured on a J-810 spectropolarimeter equipped with a fluorescence attachment and a temperature controller (Jasco, Tokyo, Japan) at 25^0C, using a 4 mm × 4 mm rectangular quartz cuvette. Under a gentle stream of nitrogen, the same peptide sample was used to remove the solvent. Then the sample was put inside of a desiccator chamber for around 1 h, and later the sample was put into J-810 spectropolarimeter to record CD spectra of dry peptides. Aqueous buffer (25-mM NaCl, 25-mM Na,K-phosphate, 20 μM ThT, pH 7.2) was then added to the dry peptide to obtain a peptide concentration of 50 μM, and the top of the

cuvette was wrapped with Parafilm and rotated on a Fisherbrand™ Multi-Purpose Tube Rotator. Three samples were conducted in parallel, that is, $A\beta_{1-40}$, $pEA\beta_{3-40}$, and their 1:1 molar combination. At defined time points, CD (180–350 nm) and ThT fluorescence (400–600 nm with excitation at 435 nm) spectra were recorded on same peptide samples on the J-810 instrument. CD and fluorescence measurement were continued for 200 h.

By plotting ThT fluorescence at 480 nm as a function of time of incubation in buffer the kinetics of fibrillogenesis was analyzed, and from the time dependence of the ellipticity ratio $\theta\rho/\theta\beta$, where $\theta\rho$ and $\theta\beta$ are the ellipticities representing unordered and β-sheet structures the kinetics of structural transitions were determined. These plots were fitted with single-exponential curves, which provided the rate constants and the limiting values of ThT fluorescence and secondary structural changes.

For FTIR experiments on peptides in aqueous buffer, HFIP solution of the peptide was placed in small glass vials and the solvent was removed by desiccation. D_2O-based buffer containing 25-mM NaCl and 25-mM Na,K-phosphate, adjusted to pH* 6.8, was added to the dry peptide to achieve 50 μM concentration and stirred for 1.5 h using a magnetic stir bar. Here, pH* is the pH-meter reading and corresponds to pD 7.2 after correction for the 0.4 pH unit isotopic shift.[93] 70μL of the peptide solution was placed between two CaF2 disks (32 mm in diameter, 3 mm thick), separated by a 50 μm-thick Teflon spacer, and transmittance spectra were measured at 2 cm^{-1} nominal resolution, using a Vector-22 FTIR spectrometer (Bruker Optics, Billerica, MA, USA) equipped with a liquid nitrogen cooled Hg-Cd-Te detector. Transmittance spectra of the blank buffer were measured and used as reference to calculate the absorbance spectra.

For FTIR measurements of dry peptides and those hydrated from gas phase, 35 μL of 200 μM HFIP solution of Aβ peptide were spread on the surface of a CaF_2 disk and air dried, followed by desiccation for 15 min. The disk was installed on a sample holder, and FTIR transmittance spectra of the dry peptide were measured. This was followed by measurements of spectra of the peptide that was slowly hydrated by stepwise exposure to D_2O vapor. D_2O was used because H_2O absorbs in the amide I region and thereby affects the conformation sensitive amide I band intensity and line shape. Around 10 mL of D_2O in a small beaker was placed on a hotplate, covered with a larger glass beaker, and brought to ~90^0C to maximize evaporation. The peptide sample was placed inside the large beaker and thereby exposed to D_2O vapors for a defined number of seconds, and then the spectrum of the partially hydrated peptide was measured. Care was taken to thermally isolate the peptide and avoid its heating during hydration from gas phase. Absorbance spectra were obtained using the transmittance spectrum of the bare CaF2 disk as reference. This procedure was continued multiple times until spectral changes in the amide I and amide II regions saturated. Precisely, the amide II absorbance band intensity at 1550–1530 cm^{-1} gradually decreased due to amide hydrogen-deuterium (H/D) exchange and the amide I peak shifted to lower wavenumbers due to α-helix to β-sheet transition. The kinetics of structural changes were analyzed by plotting the ratio of β-sheet and α-helix structures against time of exposure to D_2O vapor. The amount of α-helix at time t was considered proportional to the absorbance at α-helical wavenumber, α_t / $A_{w\,\alpha,t}$. Values of α-helical wavenumbers, W_α, were determined based on the spectra of dry peptides, which were α-helical. Upon hydration by D_2O vapor, $A_{w\,\alpha,t}$ gradually decreased and the β-sheet signal emerged and grew in intensity at β-sheet wavenumber, W_β. Because the α-helical amide I band has nonzero intensity at W_β, which we denote $A_{x,t}$, the amount of β-sheet at time t is proportional to the rise in intensity at W_β with

respect to $A_{x,t}$, that is, $\beta_t \propto A_{w\,\beta,t} - A_{x,t}$. As the peptide hydration progresses, $A_{x,t}$ decreases by a time-dependent factor $A_{w\,\alpha,t}/A_{w\,\alpha,o}$:

$$A_{x,t} = A_{w\,\beta,0}\frac{A_{w\,\alpha,t}}{A_{w\,\alpha,0}}$$

The β-sheet/α-helix ratio is then given as follows:

$$\frac{\beta_t}{\alpha_t} = \frac{A_{w\,\beta,t}}{A_{w\,\alpha,t}} - \frac{A_{w\,\beta,0}}{A_{w\,\alpha,0}}$$

2.4.2 Preparation for Segmental Aggregation and Structural Propensities of Amyloid beta (Aβ) Peptide

The synthetic $A\beta_{1\text{-}42}$ peptide was from Innovagen (Lund, Sweden) and was >98% pure. Synthetic peptide fragments, acetylated at N-terminus and amidated at C-terminus, was purchased from Peptide 2.0 Inc. (Chantilly, VA, USA) and were 98-99% pure, as verified by high performance liquid chromatography and mass-spectrometry. Hexafluoroisopropanol (HFIP), thioflavin-T (ThT), salts, buffers, and most of other reagents were purchased from Sigma- Aldrich (St. Louis, MO, USA) or Fisher Scientific (Hanover Park, IL, USA). Quartz cuvettes for circular dichroism (CD) measurements were from Starna Calls, Inc. (Atascadero, CA, USA). CaF_2 windows for Fourier transform infrared (FTIR) studies were from Buck Scientific (East Norwalk, CT, USA). D_2O (99.8% pure) was from Cambridge Isotope Laboratories (Andover, MA, USA).
Circular dichroism (CD) and fluorescence spectra were measured using a J-810 spectropolarimeter equipped with a fluorescence attachment and a temperature controller (Jasco, Tokyo, Japan) at 25 °C. Lyophilized peptides was dissolved in HFIP at a desired concentration and CD spectra were measured using a 4 mm × 4 mm rectangular quartz cuvette. Then, the solvent was removed by desiccation and CD spectra of the dry peptide stuck on the walls of the

cuvette were measured. This was followed by addition of aqueous buffer (25 mM NaCl, 25 mM Na,K-phosphate, 20 μM ThT, pH 7.2) to achieve a target peptide concentration. The cuvette was capped with a Teflon stopper, sealed with parafilm, and rotated on a Fisherbrand™ Multi-Purpose Tube Rotator for several days. CD, ThT or intrinsic peptide fluorescence, and light scattering at 90 degrees were measured periodically on same sample, at pre-determined time pints, to follow the time dependence of structural changes and aggregation/fibrillogenesis of the peptides, using the multifunctional J-810 instrument. Measurements of these parameters on same samples in real time excluded sample to sample errors. For each peptide system, time-dependent spectroscopic measurements were repeated in three or four independent experiments.

ThT fluorescence was averaged between 475 and 485 nm, when excited at 435 nm, and plotted against time of incubation in buffer. For fluorescence RET experiments, incident light at 220 nm was used for predominant excitation of phenylalanine as compared to tyrosine, and spectra were measured between 200 and 400 nm. For each donor/acceptor peptide pair, the fluorescence of individual peptides was measured at 100 μM concentration, then spectra were recorded for the two peptides mixed at 50 μM each to maintain the same total peptide concentration. For light scattering, incident light at 550 nm was used to avoid generation of fluorescence signal and scattered light intensity at 90 degrees was measured between 530 and 570 nm. The signal intensity was averaged between 553 and 557 nm and plotted as a function of time.

The degree of inhibition of fibrillization of $A\beta_{1-42}$ by peptide fragments was evaluated based on ThT fluorescence data. Total saturating ThT fluorescence between 32 and 48 hours in the presence of both $A\beta_{1-42}$ and a given fragment was considered as a sum of fluorescence due to each component. Then, fluorescence owing to $A\beta_{1-42}$ fibrils in the presence of a fragment, F^*,

was determined by subtracting the signal measured for the fragment alone from total fluorescence. Fluorescence signal measured for pure fragments was corrected for concentration before subtraction, i.e. multiplied by 0.7, assuming a linear relationship between fluorescence and peptide concentration. Inhibition percentage of $A\beta_{1-42}$ fibrillogenesis was calculated as $IP = (1 - F^*/F_0)\times 100\%$, where F_0 is ThT fluorescence of $A\beta_{1-42}$ in the absence of fragments.

For FTIR spectroscopy**,** HFIP solution of the peptide was placed in small glass vials and the solvent was removed by desiccation. D_2O-baseb buffer containing 25 mM NaCl and 25 mM Na,K-phosphate, adjusted to pD 7.2, was added to the dry peptide to achieve 50 μM concentration for the full-length peptide $A\beta_{1-42}$ and 50 μM for the fragments. Peptide samples were stirred by a small (3 mm in diameter) magnetic stir bar over 100 hours. At defined time points, a 70-μL peptide sample was placed between two CaF_2 disks (32 mm in diameter, 3 mm thick), separated by a 50 μm thick Teflon spacer, and FTIR spectra were measured at 2 cm^{-1} nominal resolution, using a Vector-22 FTIR spectrometer (Bruker Optics, Billerica, MA, USA) equipped with a liquid nitrogen-cooled Hg-Cd-Te detector. Transmittance spectra of the blank buffer were measured and used as reference to calculate the absorbance spectra. For measurements of FTIR spectra of dry peptide sample, HFIP solution of the peptide was spread on a CaF_2 disk, dried for 15 minutes in a desiccator, followed by measurement of the transmission spectrum. A transmission spectrum of the clean CaF_2 disk was used as reference to calculate the absorbance spectrum. The instrument was continuously purged with dry air to avoid contribution of H_2O vibrational/rotational features in the amide I region. Absorbance spectra of atmospheric H_2O were measured separately and subtracted from spectra of peptides when such contribution was detected.

CHAPTER 3: RESULTS AND DISCUSSION

3.1 Structure and Aggregation of Aβ1-40 and Pyroglutamylated pEAβ3-40 Separately and Combined.

3.1.1 Kinetics of Fibrillogenesis:

Due to the unstable, polymorphic structural behavior [94-96] of Aβ peptide, to avoid sample to sample errors, it is very important to measure the aggregation and structural change on same sample at same time. The kinetics of fibrillogenesis and the accompanying structural changes of $A\beta_{1\text{-}40}$, $pEA\beta_{3\text{-}40}$, and their equimolar combination have been monitored by near-simultaneous measurements of Th-T fluorescence and CD spectra of same samples, using a spectropolarimeter with a fluorescence attachment.

Incubation of all three peptide samples in aqueous buffer, Th-T fluorescence around 480 nm (λexcitation = 435 nm) gradually increased (Figure 3.1.1). To estimate fibrillogenesis propensities of the peptides, the time dependence of Th-T fluorescence and their amplitudes have been observed. For $A\beta_{1\text{-}40}$, Th-T fluorescence reached ~0.23 relative units and then gradually decreased as shown in Figure 3.1.1 a, d. Single-exponential fit of the fluorescence increase yielded a rate constant of $k = 0.029 \pm 0.004\ h^{-1}$ (Table 3.1.1) (here and below: average ± SD from triplicate experiments). It has been reported that for various forms of Aβ, the ascending and descending wings of the time dependence of Th-T fluorescence were observed which later interpreted in terms of formation of dense, Th-T-impermeable clumps of fibrils. [51,57,97]

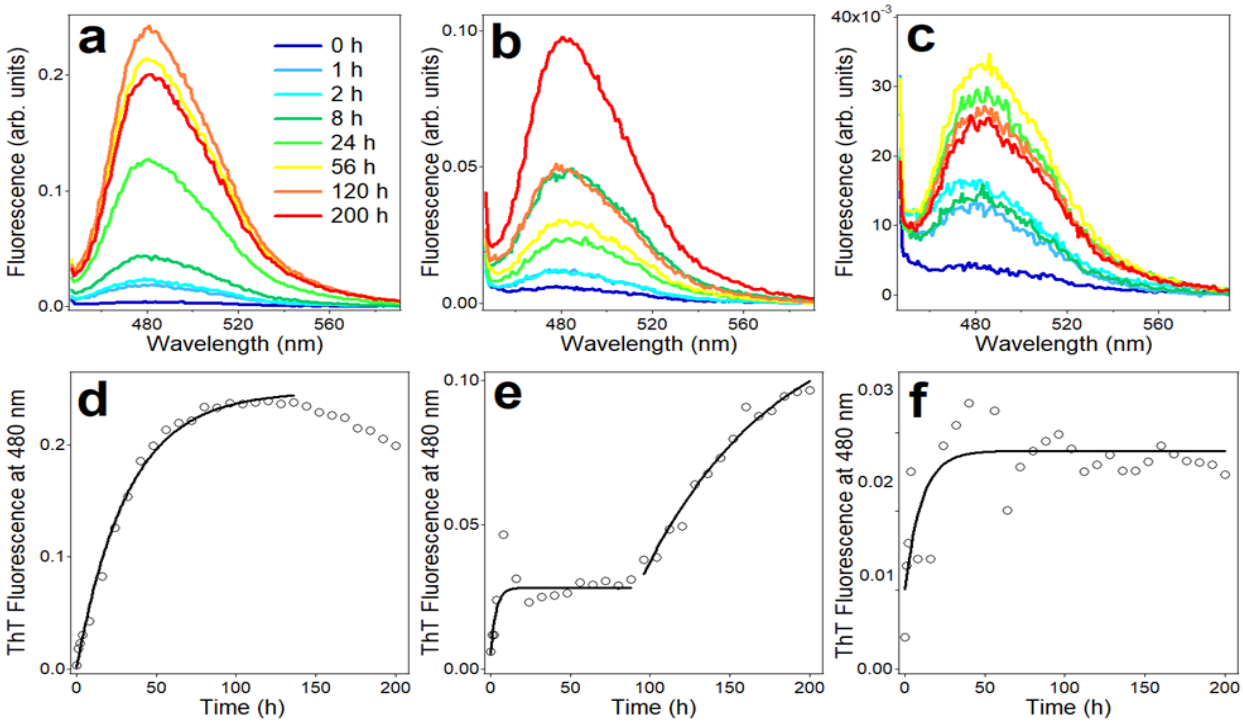

Figure 3.1. 1: Th-T fluorescence spectra of 50 µM $A\beta_{1\text{-}40}$ (a) $pEA\beta_{3\text{-}40}$ (b), and their equimolar combination (c) incubated in aqueous buffer containing 25 mM NaCl, 20 µM Th-T, 25 mM Na,K-phosphate (pH 7.2) at 25°C. All samples have been constantly mixed in a rotatory mixer between measurements for 200 hours. Only spectra at selected time intervals, indicated in panel a, are shown. Excitation was at 435 nm. Panels d, e, and f show the time courses of Th-T fluorescence and the single-exponential fits of data in panels a, b, c, respectively. For each peptide sample, data from a selected experiment are shown. The rate constants from these particular experiments are as follows: k = 0.031 h^{-1} for $A\beta_{1\text{-}40}$ (d), k1 = 0.300 h^{-1} and k2 = 0.012 h^{-1} for $pEA\beta_{3\text{-}40}$ (e), k = 0.095h^{-1} for the 1:1 mixture (f).

For $pEA\beta_{3\text{-}40}$, the nature of time dependence of Th-T fluorescence was different compared to $A\beta_{1\text{-}40}$. Two distinct kinetic components of Th-T fluorescence change over time have been observed (Figure 1b, e). With a rate constant of k1 = 0.320 ± 0.042 h^{-1}, The first component was comparatively fast and reached 0.025 units. On the other hand, the second component with a rate

constant k2 = 0.014 ± 0.002 h^{-1}, was slow and it reached an overall fluorescence intensity of ~0.1 units at 200 hours of incubation in buffer.

A very weak Th-T fluorescence was observed for the equimolar combination of the two peptides. The Th-T fluorescence reached around 0.025 units with single-exponential fit rate constant of k = 0.092 ± 0.015 h^{-1}(Figure 3.1.1c, f and Table 3.1.1). All these data clearly indicate that compare to the peptide pEA$\beta_{3\text{-}40}$, A$\beta_{1\text{-}40}$ undergoes fibrillogenesis through distinct pathway. Within 4 days of incubation in buffer, A$\beta_{1\text{-}40}$ forms mature fibrils and then the fibrils incline to form supramolecular assemblies. The sample pEA$\beta_{3\text{-}40}$ rapidly obtains a conformation that produces low Th-T fluorescence compared to A$\beta_{1\text{-}40}$. This indicates in the sample of pEA$\beta_{3\text{-}40}$, a very small fraction of the sample undergoes fibrillogenesis and the remaining follows with a much slower rate. An initial rapid increase of Th-T fluorescence of the pEA$\beta_{3\text{-}40}$ sample followed by a second, slower phase, a biphasic aggregation kinetics of pEA$\beta_{3\text{-}40}$ was observed in earlier experiments.[48]

Table 3.1. 1: Rate constants of the increase in Th-T fluorescence of A$\beta_{1\text{-}40}$, pEA$\beta_{3\text{-}40}$, and their equimolar combination upon incubation in aqueous buffer.

Sample	Th-T fluorescence
A$\beta_{1\text{-}40}$	k = 0.029 ± 0.004 h^{-1}
pEA$\beta_{3\text{-}40}$	k1 = 0.320 ± 0.042 h^{-1} k2 = 0.014 ± 0.002 h^{-1}
Combination (1:1)	k = 0.092 ± 0.015 h^{-1}

A resistance of fibrillogenesis was observed for the A$\beta_{1–40}$/pEA$\beta_{3–40}$ equimolar combination. The Th-T fluorescence was saturated at a low level, similar to the initial phase of pEA$\beta_{3–40}$.

Overall, the data indicates that the small fraction of $pEA\beta_{3-40}$ sample forms fibrils but inhibits the formation of fibril in larger scale separately or in equimolar combination with $A\beta_{1-40}$.

3.1.2 Peptide Structure from Circular Dichroism

To achieve monodisperse solution (free from preformed aggregates), the lyophilized form of $A\beta_{1-40}$ and $pEA\beta_{3-40}$ peptides were dissolved in 1,1,1,3,3,3-hexafluoro-2-propanol (HFIP).[98] For each peptide and their equimolar combination, the CD spectra of HFIP solution were measured. A deep minimum around 205-208 nm and a weak minimum at 222 nm were observed from those spectra (Figure 3.1.2). The dry sample of all three peptides (after the solvent was removed) shows two minima at around 211 and 223 nm. The intensities of CD spectra for solvent samples and dry samples were almost equal. It has been reported in previous experiments that the minima around 208-211 nm and 221-224 nm are regions of α-helical structure of a peptide, produced by π–π^* and n–π^* electronic transitions. [99-101] This can only imply that in separated or in combination, the peptides in HFIP solvent and in dry state adopt α-helical conformation. For distorted α-helices or proteins containing several short helices with "distorted" edges are associated with red-shifted n–π^* transition and larger $\theta_{n-\pi^*}/\theta_{\pi-\pi^*}$ ratios [102]. Additionally, red shift of n–π^* transition can occur because of low polarity of the protein's environment.[100] Hence, more flexible α-helices or large number of shorter α-helices are present in the peptide sample in dry state compared to peptide sample in HFIP can represented in terms of the slight red shift of the bands and significantly larger $\theta_{n-\pi^*}/\theta_{\pi-\pi^*}$ ratios. A lower polarity of the dry samples compared with HFIP solutions may also contribute to the difference. In APP, the sequences of Aβ are usually dehydrated which is the part of α-helical transmembrane segment of the protein [103,104]. So, for analysis of the structural transition following cleavage

and mixed with an aqueous solution, the α-helical conformation of dry peptide can serve as a reasonable initial point.

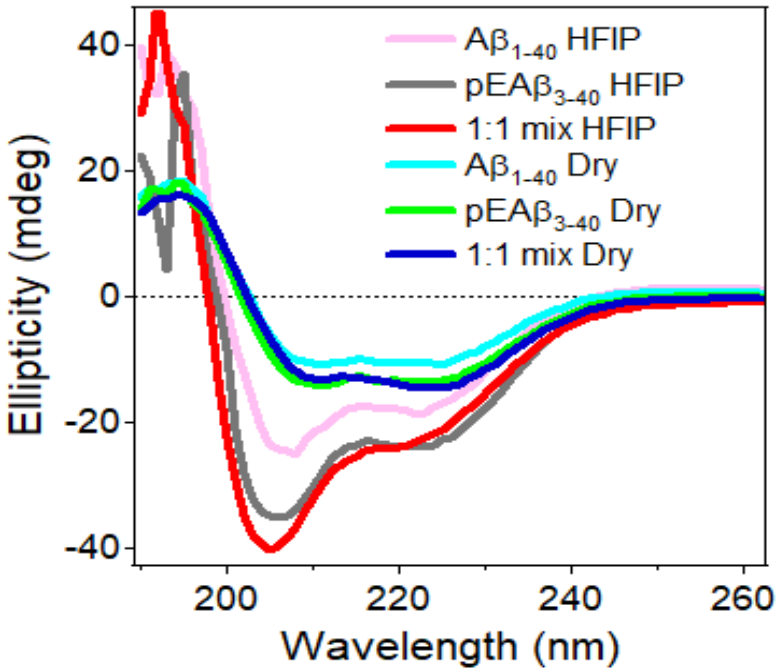

Figure 3.1. 2: Circular dichroism spectra of $A\beta_{1-40}$, $pEA\beta_{3-40}$, and their 1:1 molar combination dissolved in HFIP at 50 μM total peptide concentration and in dry state, as indicated.

After exposed to aqueous buffer all samples of peptides ($A\beta_{1–40}$, $pEA\beta_{3–40}$, and their equimolar combination) achieved the unordered structure as indicated by negative ellipticity between 198 and 204 nm (Figure 3.1.3). This can only mean that the dry peptide sample is still in the wall of testing cuvette and the suspension from the wall of cuvette into the buffer can be monitored by observing the gradual increment of the signal intensity. After several hours of incubation, $A\beta_{1–40}$ sample developed a distinct CD spectra minimum at 217 nm (Figure 3.1.3a) which can be interpreted as the sample have transitioned from unorder structure to β-sheet structure. For $pEA\beta_{3–40}$, the CD spectra minimum was at 222 nm (Figure 3.1.3b). Depending on peptide structural details, β-sheet n–π* band can reach 225 nm [77,80]. On the other hand, $pEA\beta_{3–40}$ may

contain a fraction of α-helical structure with n–π* transition around 222 nm[99,100] and/or type I or type II β-turns with CD minima between 220 and 225 nm.[69] For the equimolar combination of $A\beta_{1-40}$ and $pEA\beta_{3-40}$, unordered conformation was acquired in aqueous buffer (negative ellipticity around 203 nm) then the sample have transitioned to β-sheet structure with CD minimum at 217 nm (Figure 3.1.3c).

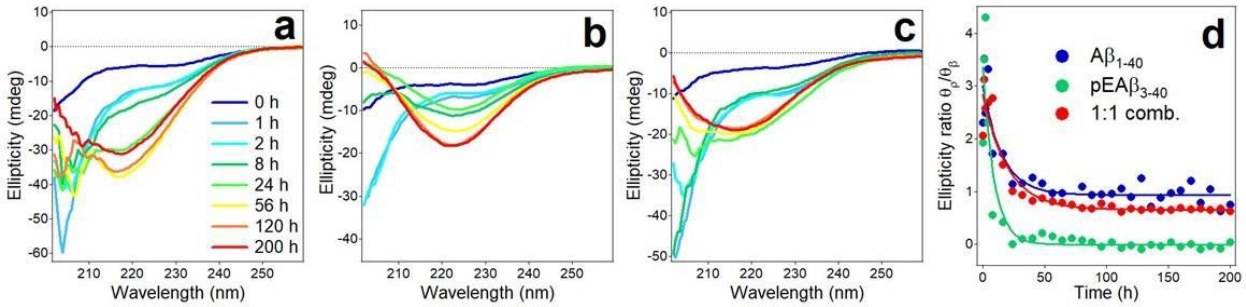

Figure 3.1. 3: Circular dichroism spectra of $A\beta_{1-40}$ (a), $pEA\beta_{3-40}$ (b), and their 1:1 molar combination (c) incubated in aqueous buffer (25 mM NaCl, 20 μM ThT, 25 mM Na,K-phosphate, pH 7.2) at 50 μM total peptide concentration for time periods indicated in panel a (color code is the same in panels a, b, c). Kinetics of transition from unordered structure to β-sheet structure are presented in panel d as $\theta_{205}/\theta_{217}$ for $A\beta_{1-40}$ and the 1:1 combination and $\theta_{205}/\theta_{222}$ for $pEA\beta_{3-40}$. Lines are single-exponential fits with rate constants of 0.064 h^{-1} for $A\beta_{1-40}$, 0.109 h^{-1} for $pEA\beta_{3-40}$, and 0.049 h^{-1} for the combined sample. For each peptide sample, data from a selected experiment are shown.

Even though there is no definitive isodichroic points were present in the CD data, the $A\beta_{1-40}$ spectra tend to converge at around 208 nm except for the first observation data since most of the peptide were still in the wall of testing cuvette (Figure 3.1.3a). Overall, the time dependence CD data suggested that the peptide sample $A\beta_{1-40}$ most likely have two-component transition from the unorder structure to β-sheet structure. In contrast, of $pEA\beta_{3-40}$ and their equimolar

combination have more complex transition involving additional structural components, consistent with above discussion and with the two-phase kinetics of fibrillogenesis (Figure 3.1. 1e).

It has been observed that after 200 hours of incubation in buffer the peptide $A\beta_{1–40}$, the ellipticities have got saturated in the range 217-222 nm after 100h of incubation faster than that of $pEA\beta_{3–40}$ and the 1:1 combination. This indicates that the quantity of β-sheet in $A\beta_{1–40}$ exceeds that of $pEA\beta_{3–40}$ and the 1:1 combination by a factor of 1.5 to 2 (Figure 3.1.3a–c), in qualitative agreement with ThT fluorescence data (Figure 3.1.1). The time dependence of the ellipticity ratio $\theta\rho/\theta\beta$ i.e the kinetics of the transition from unordered to β-sheet structure were quantify by the single-exponential curves with the following rate constants: $k = 0.059 \pm 0.010\ h^{-1}$ for $A\beta_{1–40}$, $k = 0.118 \pm 0.015\ h^{-1}$ for $pEA\beta_{3–40}$, and $k = 0.045 \pm 0.007\ h^{-1}$ for the 1:1 molar combination ($\theta\rho$ and θ_β are the ellipticities corresponding to unordered and β-sheet structures, respectively) (Figure 3.1.3d and Table 3.1.2).

Table 3.1. 2: Rate constants of the transition from unordered to β-sheet structure of $A\beta_{1–40}$, $pEA\beta_{3–40}$, and their equimolar combination upon incubation in aqueous buffer.

Sample	Transition to β-sheet
$A\beta_{1–40}$	$k = 0.059 \pm 0.010\ h^{-1}$
$pEA\beta_{3–40}$	$k = 0.118 \pm 0.015\ h^{-1}$
Combination (1:1)	$k = 0.045 \pm 0.007\ h^{-1}$

To avoid errors due to spectral noise at lower wavelength ellipticity at 205 nm was chosen for $\theta\rho$. By analyzing all these data, it can say that the transition to β-sheet structure was faster for

sample pEA$\beta_{3–40}$ compared to A$\beta_{1–40}$ and their equimolar combination undergoes slower transition to β-sheet structure than that of the two peptides separately.

Overall, the CD data imply that (i) A larger fraction β-sheet of A$\beta_{1–40}$ forms compare than pEA$\beta_{3–40}$ or the A$\beta_{1–40}$/pEA$\beta_{3–40}$ (1:1) combination, (ii) pEA$\beta_{3–40}$ undergoes transition to β-sheet structure and may involve fractions of α-helix and/or β-turn structures during the transition, and (iii) the rate of the secondary structural transition decreases in the sequence: pEA$\beta_{3–40}$ > A$\beta_{1–40}$ > A$\beta_{1–40}$/pEA$\beta_{3–40}$ combination.

The faster transition to β-sheet structure but lower intensity in ThT fluorescence (Figure 3.1.1b) and weaker CD intensity (Figure 3.1.3b) of pEA$\beta_{3–40}$ compared with A$\beta_{1–40}$ can be interpreted as the former peptide forms intermediate β-sheet structure which can be represented as seeds for the growth of fibril. The two-phase ThT fluorescence of pEA$\beta_{3–40}$ (Figure 3.1.1e), fast nucleation phase and a slow elongation (fibril growth) phase interpretation is coherent with the former statement. In earlier study, it has been documented that for both pEA$\beta_{3–40}$ and pEA$\beta_{3–42}$ the aggregation initiates rapidly by a seeding process,71 is in agreement with our findings.
From the red-shifted CD spectra of pEAβ3–40 (Figure 3.1.3b) it can be said that the sample pEA$\beta_{3–40}$ generates heterogeneous secondary conformation compared to unmodified peptide with the mostly β-sheet fibrillar structure. The equimolar combination of A$\beta_{1–40}$/ pEA$\beta_{3–40}$ shows a similar phase of structural conversion as the initial short phase as pEA$\beta_{3–40}$, as it reaches around 0.025 relative units of fluorescence. Furthermore, it stays as that level at least for 200 hours (Figure 3.1.1f). Even though the equimolar combination of A$\beta_{1–40}$/ pEA$\beta_{3–40}$ might be able to produce mature fibrils at later time, the data implicated that the fibril formation had delayed by the presence of pEA$\beta_{3–40}$. Overall, the peptide sample kept in a prefibrillar form for slower time.

3.1.3 Peptide Structure from FTIR Spectroscopy

To provide furthermore understanding into the secondary structural information, $A\beta_{1-40}$, $pEA\beta_{3-40}$, and their combination in aqueous buffer were monitored by FTIR spectroscopy. All the three samples show FTIR amide I band (Figure 3.1.4) after calculating the absorbance spectra from transmission spectrums. To enhance the amide I band second derivative resolution has been obtained where two major components was identified where 1673 cm^{-1} is assigned at as β-turn and other 1623 cm^{-1} is assigned to β-sheet. [105-107] The lower frequency at 1623 cm^{-1} had suggested as the formation of intermolecular, aggregated β-sheet. [106,108] The weaker components at 1657 and 1647 cm^{-1} can be assigned to residual α-helix and either unordered structure or amide-deuterated α-helix, respectively. Spectral features at 1636 and 1689 cm−1 have assigned as a small fraction of intra-molecular β-sheet and the higher frequency counterpart of antiparallel β-sheet structure. [104–106]

It has been reported in various studies that the FTIR is accomplished of differentiate between α-helix, β-sheet, and β-turn structures way improved than that CD because the structural features are spectrally overlapped at the latter measurement. Thereby, FTIR analysis identifies the existence of β-turn and α-helical structures with the β-sheet structure not only in $pEA\beta_{3-40}$ sample, as insinuated by CD data, but also in $A\beta_{1-40}$ and their equimolar combination. The arrangement of β-sheets is at least partially antiparallel. These data also have suggested that the structural conformation of the equimolar combination of the two peptides looks like that of $pEA\beta_{3-40}$ more than $A\beta_{1-40}$, coherent with CD and ThT fluorescence data. While it remains ambiguous whether various structural components are existent in same peptide molecules or different molecules adopt different structures, resulting in a heterogeneous peptide samples,

FTIR data show that the transition from the initial α-helical conformation to β-sheet structure is more intricate than a two-component transition.

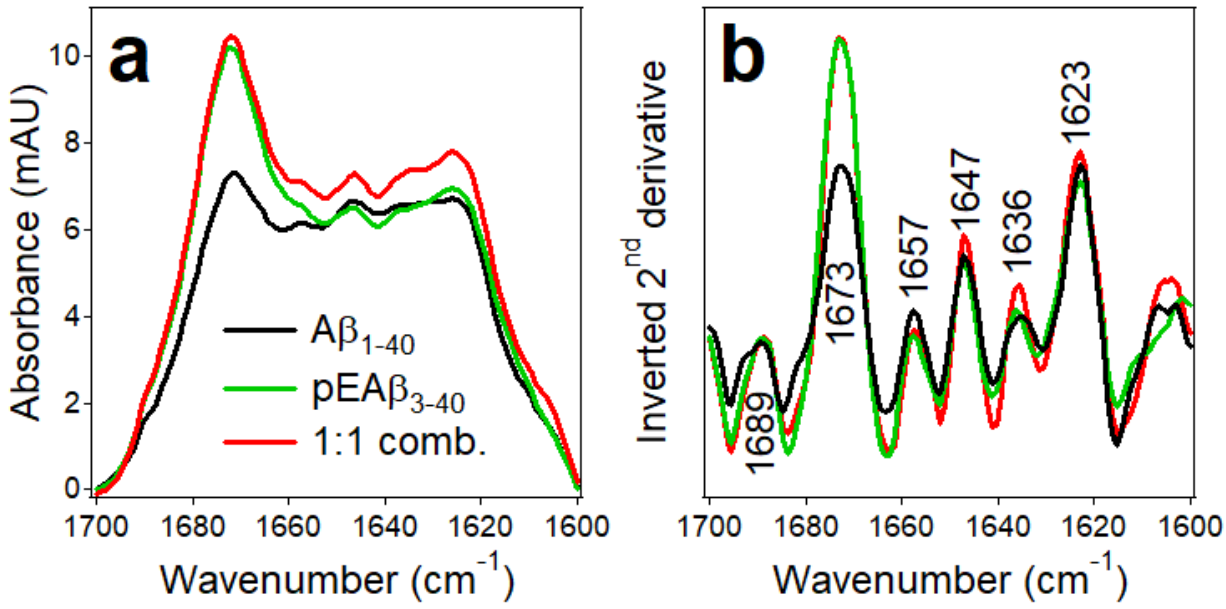

Figure 3.1. 4: FTIR spectra (a) and inverted second derivatives (b) of $A\beta_{1\text{-}40}$, $pEA\beta_{3\text{-}40}$, and their 1:1 combination, as indicated in panel (a), incubated in aqueous buffer of 25 mM NaCl, 25 mM Na,K-phosphate in D_2O, pD 7.2, for 1.5 – 2.0 hours.

3.1.4 Kinetics of Structural Transition upon Hydration from Gas Phase

From previous recorded data, it can be said that in dry state the peptide Aβ adopts α-helical structure and transitions to a β-sheet conformation in aqueous buffer but neither the preliminary α-helical structure of Aβ that is just cleaved off from APP nor the fibrils β-sheet conformation exert the cytotoxic effect. The intermediate, transient prefibrillar structures are the major toxic species. Hence, it is very imperative to determine the structural features of intermediate forms of Aβ and analyze these transitions. Here, we have developed a novel biophysical approach to accomplish this goal, that is, slow hydration of the peptide from gas phase to slow down the

structural transition, coupled with FTIR spectroscopy to apprehend the intermediate structures. The peptide Aβ were dissolved in HFIP solutions. Then the sample was put on CaF_2 glass window and dried the sample before the measurement of FTIR spectra. Then the sample was exposed to the D_2O vapor for specific time periods for gradual hydration monitored by FTIR measurements. A spectral region covering the amide I and amide II modes was analyzed. The amide I band is generated mostly by the main-chain C=O stretching vibration and is conformation sensitive. On the other hand, the amide II band, results mostly from the amide N–H in-plane bending mode and is less sensitive to the peptide's secondary structure. The amide group is expected to undergo H/D exchange due to the presence of D_2O, resulting in a ~100 cm^{-1} down- shift of the amide II band and progressive decline of intensity in the 1560- to 1540-cm^{-1} region. Thus, to evaluate peptide hydration spectral changes, the amide II region were used, and to measure the secondary structural changes, the amide I region were used.

The dry sample of $A\beta_{1-40}$ have a peak at 1657 cm^{-1}(Figure 3.1.5a) in amide I region which indicate α-helical structure. When the sample was exposed to D_2O vapor, the α-helical structure peak slowly decreased meanwhile a new component peak around 1630 cm^{-1} were generate which is the conformation wavenumber for β-sheet structure. Gradual hydration of the peptide by exposed to D_2O vapor is monitored by observe the decrease of the amide II band intensity around 1544 cm^{-1} , which suggests the amide H/D exchange. The single- exponential kinetics of the secondary structural change was characterized with a rate constant of $k = 1.49 \pm 0.37$ min^{-1} and a limiting β-sheet/α-helix ratio of 1.58 ± 0.28 (Figure 3.1.5b, Table 3.1.3).

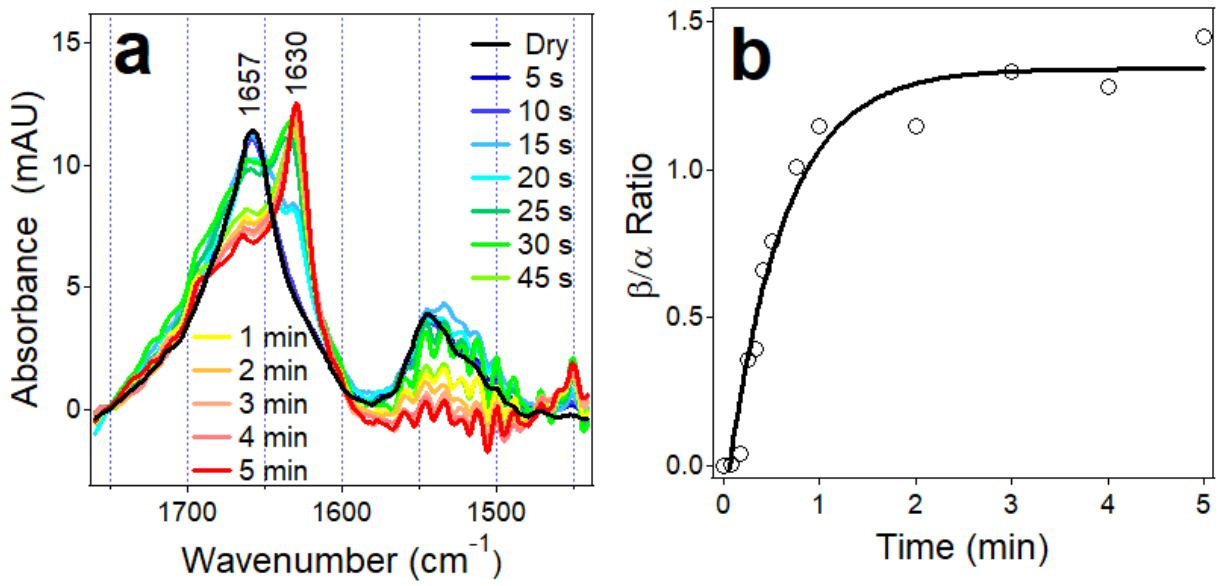

Figure 3.1. 5: (a): FTIR spectra of $A\beta_{1\text{-}40}$ in dry state and after exposure to D_2O vapor from 5 sec to 5 min, as indicated. (b): Dependence of β-sheet/α-helix ratio on time of hydration from gas phase is fitted with a single-exponential line with a rate constant of k =1.49 min^{-1}.

It has been reported in various studies that the peptides Aβ and pEAβ are existed in brain cell individually as well as combined, heterogeneous complexes [28,31]. So, it is very essential to distinguish the structural conformation of $A\beta_{1–40}$ and $pEA\beta_{3–40}$ separately and intermixed. Though circular dichroism (CD) is proficient of determination of structure of peptides but it is futile when the dissection of the structures of both peptides in a binary sample necessary which can be done by using isotope-edited FTIR spectroscopy. In this method uniformly 13C-labeled $A\beta_{1–40}$ (^{13}C-$A\beta_{1–40}$) and unlabeled $pEA\beta_{3–40}$ were used for intermixed peptides. 13C-labeling of a protein results in a 40–45 cm^{-1} downshift of its amide I band, which stipulates spectral resolution of both 13C-labeled and unlabeled proteins when combined in one sample.[107]

In FTIR spectroscopy, ^{13}C-$A\beta_{1–40}$ show a peak at 1616 cm^{-1} in the amide I region which indicates α-helical structure and illuminating the isotopic shift of the vibrational frequency

(downshift by 41 cm^{-1}). After exposed by D_2O vapor, the sample peak at 1616 cm^{-1} gradually decrease and a new peak arise around 1588 cm^{-1}, the β-sheet component in amide I region. During the measurement it has been observed that the amide I region also confined a component around 1677 cm^{-1} that was not perceptive to amide H/D exchange. This feature has been reported previously in 13C-Aβ_{1-42} and other peptides and assigned to residual trifluoroacetic acid.[85] As expected, the amide II band shows downshift from 1544 cm^{-1} to 1529 cm^{-1} due to 13C-labeling to unmodified peptide. The amide II had exhibited multiple spikes in some measurements, which are produced by the vibrational/rotational hyperfine structure of D_2O bending mode [109,110] and do not comprise spectral noise. Amide H/D exchange was monitored in the gradual regression of amide II band intensity and correlated with the transition from α-helix to β-sheet conformation, as described in Figure 3.1.6d. The kinetics of α-helix to β-sheet transition was illustrated with a single-exponential rate constant $k = 1.31 \pm 0.25$ min^{-1} and a limiting β-sheet/α-helix ratio of 1.72 ± 0.33 (Table 3.1.3).

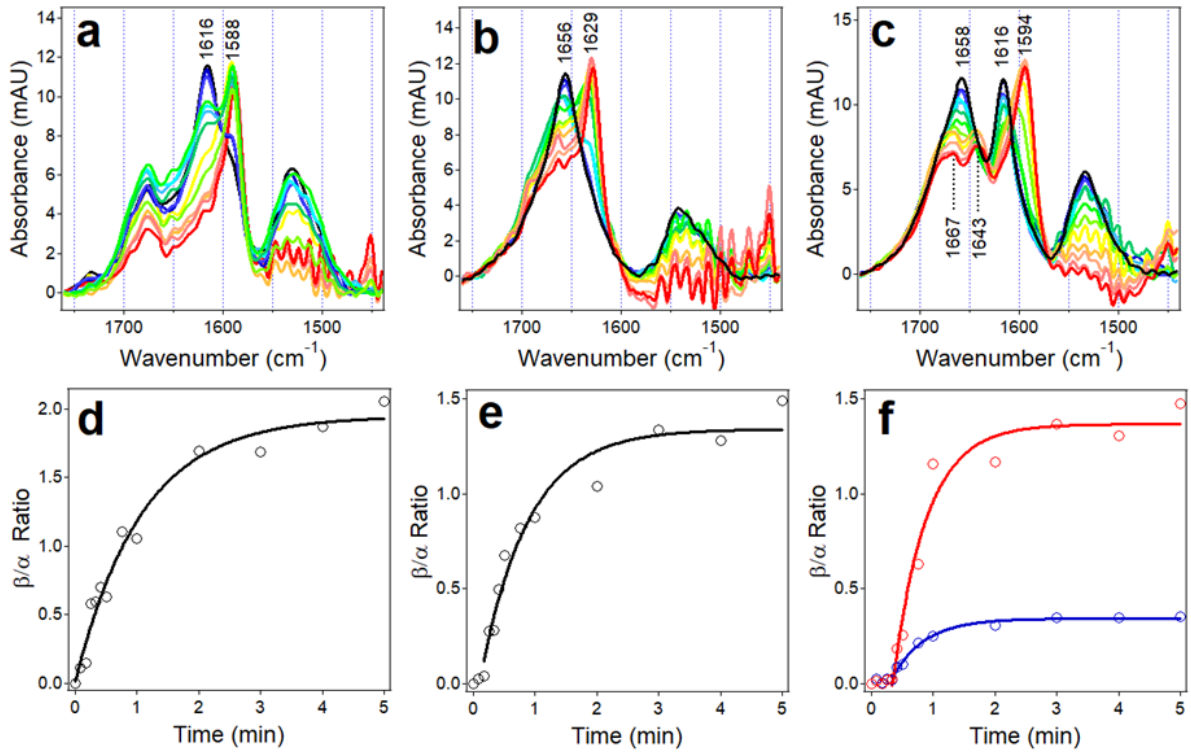

Figure 3.1. 6: FTIR spectra of 13C-A$\beta_{1\text{-}40}$ (a), pEA$\beta_{3\text{-}40}$ (b), and their 1:1 combination (c) in dry state (black) and exposed to D_2O vapor from 5 s (dark blue) to 5 min (red). The color code is the same as in Figure 5. Kinetics of α-helix to β- sheet transitions of 13C-A$\beta_{1\text{-}40}$, pEA$\beta_{3\text{-}40}$ and the combination are presented in panels d, e, f, respectively. Data are fitted with single-exponential lines with rate constants k = 0.93 min^{-1} for 13C-A$\beta_{1\text{-}40}$ and k = 1.29 min^{-1} for pEA$\beta_{3\text{-}40}$, measured individually. For the combined peptide sample, structural transitions of 13C-A$\beta_{1\text{-}40}$ and pEA$\beta_{3\text{-}40}$, following the short lag period, are characterized with rate constants k = 1.84 min^{-1} and k = 1.88 min^{-1} (red and blue lines in panel f, respectively).

Table 3.1. 3: Rate constants (k, min^{-1}) and limiting β-sheet/α-helix ratios ((β/α)max) for α-helix to β-sheet transitions of $A\beta_{1–40}$, 13C-$A\beta_{1–40}$, and $pEA\beta_{3–40}$ separately and in equimolar combination upon exposure to D_2O vapor of dry peptide samples.

Sample	Separate		Combined	
	k	$\left(\beta/\alpha\right)_{max}$	k	$\left(\beta/\alpha\right)_{max}$
$A\beta_{1-40}$	1.49 ± 0.37	1.58 ± 0.28	N/A	N/A
13C-$A\beta_{1-40}$	1.31 ± 0.25	1.72 ± 0.33	1.67 ± 0.34	1.22 ± 0.23
$pEA\beta_{3-40}$	1.14 ± 0.19	1.25 ± 0.21	1.74 ± 0.26	0.37 ± 0.06

The dry sample of $pEA\beta_{3–40}$ shows amide I peak at around 1656 cm-1 and after exposed to D_2O vapor the new peak arise at 1629 cm-1 (Figure 3.1.6b), indicating the transition from the α-helical conformation to β-sheet structure. Simultaneously, hydration was supplemented with decline in the intensity of the amide II band around 1542 cm^{-1} because of amide H/D exchange. The kinetics of α-helix to β-sheet transition was illustrated with a single-exponential rate constant k = 1.14 ± 0.19 min^{-1} and a limiting β-sheet/α-helix ratio of 1.25 ± 0.21 (Table 3.1.3). After compare the saturating values of β-sheet/α-helix ratios of $pEA\beta_{3–40}$ with those of 13C-labeled or unlabeled $A\beta_{1–40}$, it indicates $pEA\beta_{3–40}$ contain less β-sheet and more α-helix when aqueous solution was added which is consistent with weaker ThT fluorescence and CD signal of this peptide (Figures 3.1.1b, e and 3.1.3b). The equimolar combination of 13C-$A\beta_{1–40}$/$pEA\beta_{3–40}$ display two peaks in amide I region around at 1658cm^{-1} and 1616cm^{-1} (Figure 3.1.6c) in dry state indicates the α-helical structure of both unlabeled and 13C-labeled peptides respectively. After exposed to D_2O vapor those α-helical peaks diminished and new peaks develop at around 1643 cm^{-1} and 1594 cm^{-1} and observe increment of intensity after time interval increase which

characterize β-sheet structure for unlabeled pEAβ$_{3–40}$ and 13C-Aβ$_{1–40}$, respectively. The amide II band arisen at around 1540 cm^{-1} to 1530-cm^{-1} region and declined upon exposure to D_2O vapor due to amide H/D exchange. In a combined sample, the kinetics of α-helix to β-sheet transitions showed a longer lag time compared with that seen for pEAβ$_{3–40}$ (Figure 3.1.6e and 3.1.6f) and were characterized with single-exponential rate constants k = 1.67 ± 0.34 min^{-1} and k = 1.74 ± 0.26 min^{-1} and limiting β-sheet/α-helix ratios of 1.22 ± 0.23 and 0.37 ± 0.06 for 13C-Aβ$_{1–40}$ and pEAβ$_{3–40}$, respectively (Figure 3.1.6f, Table 3.1.3).

There are several interesting effects reveal while comparing the spectra of individual peptides with their equimolar combination. The first thing it was observed that the frequencies of β-sheet structure of individual peptides (1588 and 1629 cm^{-1} for 13C-Aβ$_{1–40}$ and pEAβ$_{3–40}$, respectively) considerably lower than those of their equimolar combination (1594 and 1643 cm^{-1}). This kind of frequency shifts may occur because of (a) transition dipole coupling (TDC) effects, that is, frequency shifts due to interactions between amide I oscillators [111,112] and (b) structural differences between individual and combined peptides. It has been reported that the unperturbed amide I frequency between 1680 and 1672 cm^{-1} is generated by Unordered proteins with no H-bonding and no interaction between amide oscillators. [103-106] The specific secondary structures formation causes the oscillators of amide I into one-another's force field, resulting in transition dipole coupling (TDC) and producing characteristic frequencies, such as those presented by individual peptides (Figure 3.1.6a, b). The resultant of β-sheet signals at higher frequencies might occurred because of mutual intercalations of 13C-Aβ$_{1–40}$ and pEAβ$_{3–40}$ molecules intrude with TDC between both 13C-labeled and unlabeled amide units. Various studies suggested that aggregated β-sheets with intramolecular H-bonding generate amide I signal at 10- to 15-cm^{-1} higher frequencies than intermolecular β-sheets. [106,108] So there is

possible fact developed in the difference between the observed frequencies of β-sheet structure of the peptides in separately and combined. The peptides format intermolecular β-sheets when it hydrated individually and format β-hairpin-like structures with intramolecular H-bonding when hydrated combined. Here, equimolar combined unlabeled peptides would generate higher amide I frequency while in aqueous buffer compared to that of the peptides in separately. Oppose to this probability, the data of figure 3.1.4b display that $A\beta_{1-40}$, $pEA\beta_{3-40}$, and the 1:1 combination, all three samples produce generate β-sheet peaks at same frequencies: a major one at 1623 cm^{-1} and a minor one at 1636 cm^{-1}. Therefore, the upshifted amide I frequencies of the combined sample (Figure 3.1.6c), can be completely ascribed to TDC effects. This information insinuates that the 13C-$A\beta_{1-40}$ and $pEA\beta_{3-40}$ equimolar combination produces intertwined conformation, diminishing TDC between like molecules and thus the higher vibrational frequencies are generated. Previous study had been done with FTIR analysis on 13C-$A\beta_{1-42}$ and $pEA\beta_{3-42}$ where similar amide I spectral upshifts were identified for both peptide in their combination.[113] Although, in contradiction of the 13C-$A\beta_{1-40}$/$pEA\beta_{3-40}$ system, the spectra of individual peptide had showed residual higher frequency signals, which became primary in samples are in mixed, suggesting that the spectral upshift could not explained by TDC alone. The separated $A\beta_{1-42}$ and $pEA\beta_{3-42}$ peptides form amide I at lower frequencies represents intermolecular H-bonding, however in combination, they form intramolecular H-bonding. The study of $A\beta_{1-40}$/$pEA\beta_{3-40}$ system has shown the spectral shift, which is totally result from TDC effects, inhibiting propositions of transition in the H-bonding pattern while the peptides in combination. Moreover, the peak at 1643 cm^{-1} for $pEA\beta_{3-40}$ in equimolar combination when exposed in D_2O vapor is considerably weaker than that of 13C-$A\beta_{1-40}$, additionally the spectrum shows an added peak at 1667 cm^{-1}(Figure 3.1.6c, red line). This can be assigned to a more flexible α_{II}-helix that

absorbs at higher frequencies, in the 1667- to 1665-cm^{-1} spectral region, [114,115] proposing that pEA$\beta_{3–40}$ sustains a fraction of disordered α-helix structure at the expense of β-sheet when in aqueous environment. This result indicates that however 13C-A$\beta_{1–40}$ transition from α-helix to β-sheet structure in the combined sample, pEA$\beta_{3–40}$ forms β-sheet structure only partially and maintains a fraction of flexible, or disordered, α-helical structure.

Afterward, the data that were collected from FTIR spectroscopy have been analyzed to determine the β-sheets of hydrated peptide were either parallel or antiparallel. The second derivatives of spectra of dry and hydrated samples were done graphically which emphasize the α-helical peaks of dry peptides and the presence of β-sheet features upon hydration (Figure 3.1.7). For individual peptides, in addition to the major β-sheet component at 1629–1628 cm^{-1} (1586 cm^{-1} for 13C-A$\beta_{1–40}$), a spectral feature is observed at 1695 cm^{-1} (1651 cm^{-1} for 13C-A$\beta_{1–40}$) (Figure 3.1.7a–c), which is represented to the high-frequency counterpart of antiparallel β-sheet.[105-107] For equimolar combined sample, the spectra of β-sheet peaks for 13C-A$\beta_{1–40}$ and pEA$\beta_{3–40}$ are demonstrated at 1592- and 1645- to 1635-cm^{-1} regions, respectively, but the feature in the high-frequency region (~1692 cm^{-1}) is either nonexistent or faded (Figure 3.1.7d).

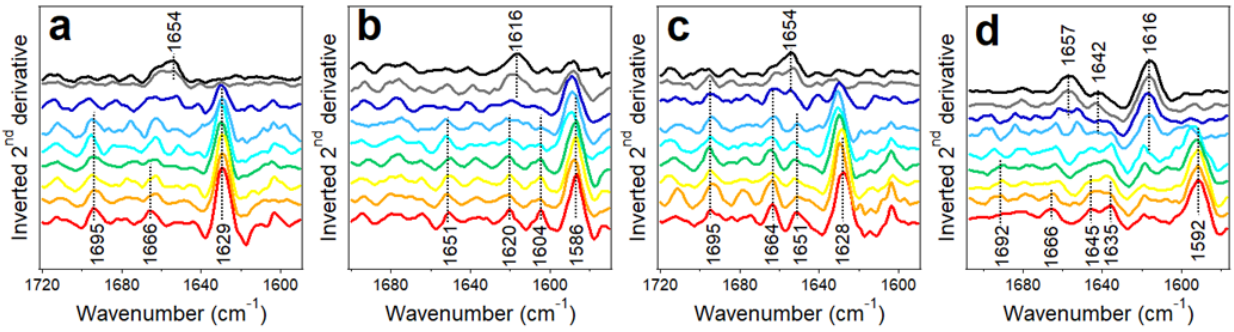

Figure 3.1. 7: Inverted second derivatives of FTIR spectra of $A\beta_{1\text{-}40}$ (a), 13C-$A\beta_{1\text{-}40}$ (b), $pEA\beta_{3\text{-}40}$ (c), and the 1:1combination of 13C-$A\beta_{1\text{-}40}$ and $pEA\beta_{3\text{-}40}$ (d) in dry state (black line) and exposed to D_2O vapor for 10 s, 20 s, 30 s, 1 min, 2 min, 3 min, 4 min, and 5 min (gray to red), derived from spectra shown in Figures 5 and 6. The wavenumbers of most prominent spectral features are indicated.

This finding insinuated that the individual peptides obtain antiparallel β-sheets structure in presence of aqueous system and form mostly parallel β-sheets when they are in combination together. Nonetheless, FTIR data on the peptides in bulk buffer exhibit the high-frequency antiparallel β-sheet component in the combined sample as well (Figure 3.1.4b). There is a possibility that the peptides form mixed antiparallel and parallel β-sheets, with a shift toward the parallel β-sheets in the combined sample hydrated from gas phase, as stated for $A\beta_{1\text{–}40}$ aggregated on ganglioside-containing membranes.[116] Spectral features at 1666–1664 and 1651 cm^{-1} (1620 and 1604 cm^{-1} for 13C-$A\beta_{1\text{–}40}$) are assigned to residual disordered or regular (amide deuterated) α-helical structures, respectively.

Lastly, the transition's kinetics from α-helix to β-sheet for 13C-$A\beta_{1\text{–}40}$ and $pEA\beta_{3\text{–}40}$ their equimolar combination implies that both peptides develop β-sheet structure quicker than the

separated peptides except the β-sheet/α-helix ratios reach low quantitatively and this tendency is much more noticeable for pEA$\beta_{3–40}$ compare to that of 13C-A$\beta_{1–40}$ (Table 3.1.3). Furthermore, the formation of onset β-sheet structure is led by a lag time for pEA$\beta_{3–40}$ but not 13C-labeled or unlabeled A$\beta_{1–40}$, and the lag period is slower for both peptides in the mixed sample (Figure 3.1.6d–f). The repetition of low β-sheet propensity of pEA$\beta_{3–40}$ and indicates mutual suppression of β-sheet fibril formation by the two peptides. The data collected from isotope edited FTIR spectroscopy corroborate the finding from CD and ThT fluorescence studies that compare to the peptide A$\beta_{1–40}$, the transition from α-helix to β-sheet conformation pEA$\beta_{3–40}$ comprises a reduced fraction of β-sheet fibrils. Previous studies suggested that A$\beta_{1–40}$ have greater helical propensity compared with pEA$\beta_{3–40}$ in H_2O/TFE environment [70,117] evidently indicate the helix forming effect TFE and are not in disagreement with present data collected in pure aqueous medium. In the equimolar combination, pEA$\beta_{3–40}$ maintains a fraction of α-helical structure and decreases β-sheet fibril formation propensity compare to A$\beta_{1–40}$. The inclination of pEA$\beta_{3–40}$ to inhibit fibrillogenesis may play a role in its increased cytotoxicity as the prefibrillar assemblies are known to employ the major toxic effect.

3.2 Segmental Aggregation and Structural Propensities of Amyloid beta (Aβ) Peptide

Structural and aggregation properties of the parent Aβ_{1-42} peptide and seven overlapping peptide fragments have been studied, i. e. Aβ_{1-10} (P1), Aβ_{6-15} (P2), Aβ_{11-20} (P3), Aβ_{16-25} (P4), Aβ_{21-30} (P5), Aβ_{26-36} (P6), and Aβ_{31-42} (P7), as shown in Figure 3.2.1, to identify the region(s) of Aβ responsible for aggregation and fibrillogenesis and to use those fragments to inhibit Aβ aggregation.

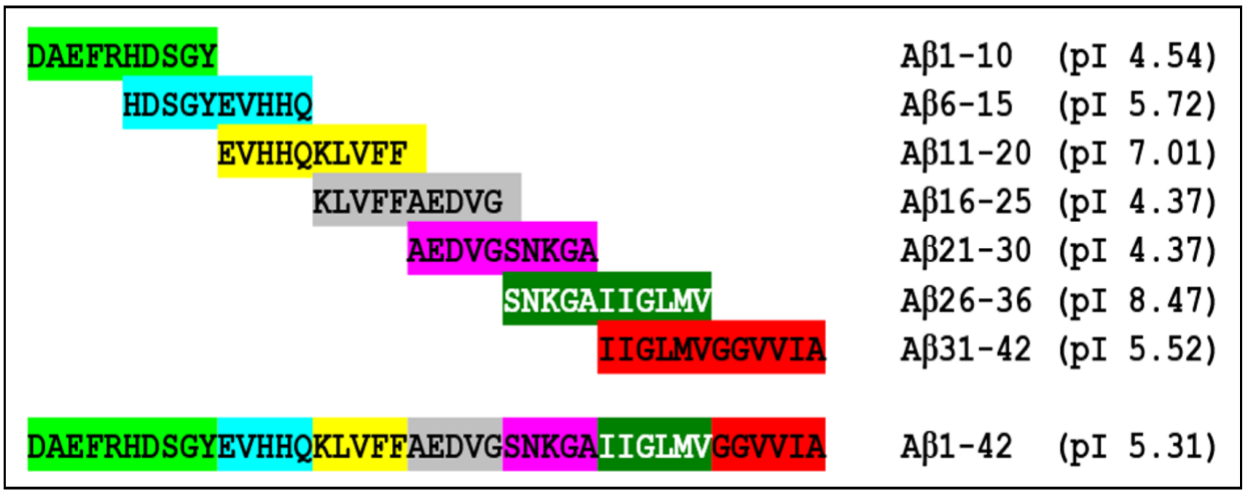

Figure 3.2. 1: Overlapping Aβ peptide fragments and the parent $A\beta_{1-42}$ peptide, presented as single single-letter sequences, along with the theoretical isoelectric point (pI) values.

3.2.1 Peptide Secondary Structure from FTIR Spectroscopy

FTIR spectroscopy was used to analyze the structural transitions in the peptides.

To disperse possible pre-existing aggregates, the lyophilized peptides were dissolved in hexafluoroisopropanol (HFIP).[98] $A\beta_{1-42}$ peptide in HFIP solution was span over a CaF_2 disk , air-dried with gentle stream of N_2 gas and desiccated for 15 minutes, followed by measurement of Fourier transform infrared (FTIR) spectra. The dry peptide obtains α-helical structure displayed by a sharp amide I peak at 1658 cm^{-1} (Figure 3.2.2). Most of the Aβ sequence corresponds to the transmembrane α-helix embedded in neuronal membranes, before cleavage from APP. [104] Therefore, this result is coherent with the intrinsic α-helical propensity of the $A\beta_{1-42}$ sequence in dry state. Instead, determining the structure of the dehydrated peptide is essential for analysis of structural transitions once the peptide is exposed to an aqueous medium.

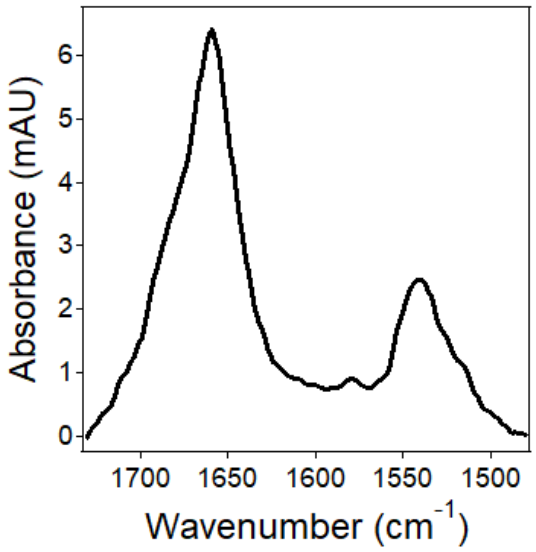

Figure 3.2. 2: FTIR spectrum of $A\beta_{1-42}$ dried on a CaF_2 disk from 50 μM HFIP solution. Amide I and amide II peaks are located around 1657 cm^{-1}, amide II around 1537 cm^{-1}, respectively.

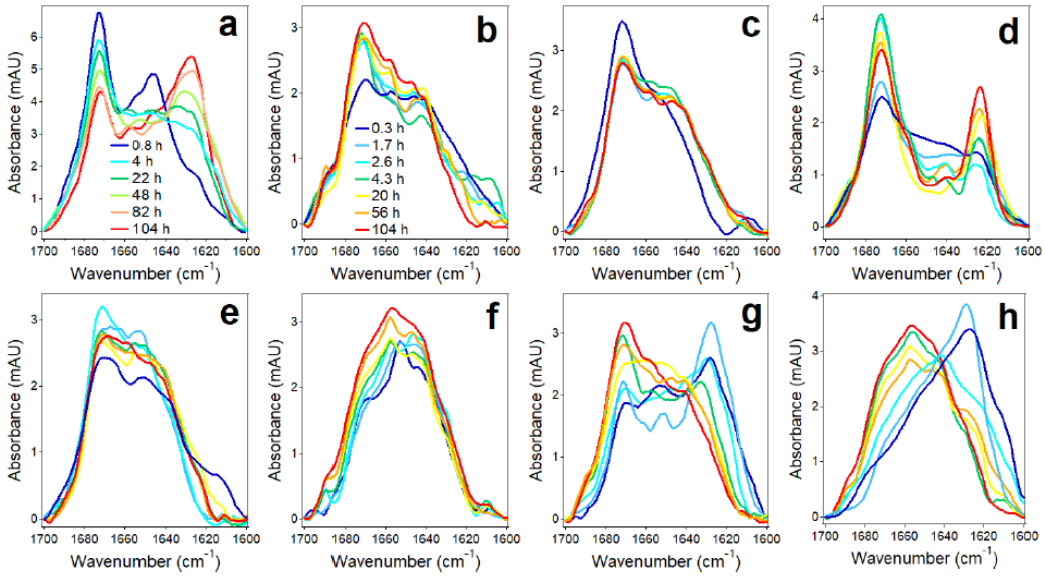

Figure 3.2. 3: FTIR spectra at indicated times of incubation in D_2O-based buffer (25 mM NaCl, 25 mM Na,K-phosphate, pD 7.2) for $A\beta_{1-42}$ (a) and peptides P1 (b), P2 (c), P3 (d), P4 (e), P5 (f), P6 (g), and P7 (h) at 25ºC. The concentrations of the peptides were 50 µM for $A\beta_{1-42}$ and 100 µM for the fragments. Times of incubation in buffer of all fragments are indicated in panel b.

Afterward, $A\beta_{1-42}$ and the seven peptide fragments in HFIP solution were dried separately in glass vials and aqueous (D_2O) buffer was added to reach concentrations of 50 μM for $A\beta_{1-42}$ and 100 μM for the peptide fragments. With a small magnetic stir bar, the samples were constantly stirred, and spectra of 70 μL volume of sample were measured periodically over 100 hours to observe structural changes of the peptides. Initially, the amide I spectrum of $A\beta_{1-42}$ exhibited two noticeable components at 1672 and 1647 cm^{-1}, suggesting mostly β-turn and unordered or loop conformations [107] (Figure 3.2.3). the peak at 1647 cm^{-1} was gradually replaced by a component at 1627 cm^{-1}, upon incubation in buffer, suggesting the formation of intermolecular β-sheet structure [107] which is consistent with the fibrillar structure of $A\beta_{1-42}$ containing β-sheet and β-turn/loop conformations [118-120] (Figure 3.2.1) and implies that through intermolecular H-bonding, formation of turn/loop structures leads aggregation and fibrillogenesis.

The distinct structural transitions were observed from the peptide fragments when they add in aqueous buffer. Each peptide fragments except P7 initially generates significant fraction of β-turn structure in supplement to irregular structure, indicated by amide I components in 1672-1670 cm^{-1} and 1640 cm^{-1} regions, respectively (Figure 3.2.3). Only P3 and P6 displayed β-sheet component at 1628-1623 cm^{-1}, among these 6 peptides (Figure 3.2.3d, g). In case of P3, both β-turn and β-sheet structures developed at the expense of irregular structure (Figure 3.2.3d), whereas in P6 the β-turn became the principal structure upon continued incubation in buffer (Figure 3.2.3g). P7 exhibited a distinctive behavior; it rapidly produced β-sheet structure with a distinctive peak around 1626 cm^{-1}, which gradually shifted to higher wavenumbers possibly reflecting transition to turn and/or α-helix structures. Therefore, peptides P3, P6, and P7 display

β-sheet formation propensity with diverse dynamics of structural transitions while the other four peptides incline to adopt β–turn/loop conformations.

3.2.2 Peptide Secondary Structure from Circular Dichroism (CD) Spectroscopy

For further analysis, the structural transition of peptides in aqueous buffer were monitored by a complementary biophysical method, circular dichroism (CD). The question "how the structural transitions of the peptides are corelated to fibrillogenesis", was focused at the same time which was accomplished by simultaneous measurements of CD spectra, light scattering, and thioflavin-T (ThT) fluorescence of same peptide samples in aqueous buffer for over 100 hours.

CD spectra of peptides dissolved in HFIP, in dry state, and in aqueous buffer were measured.

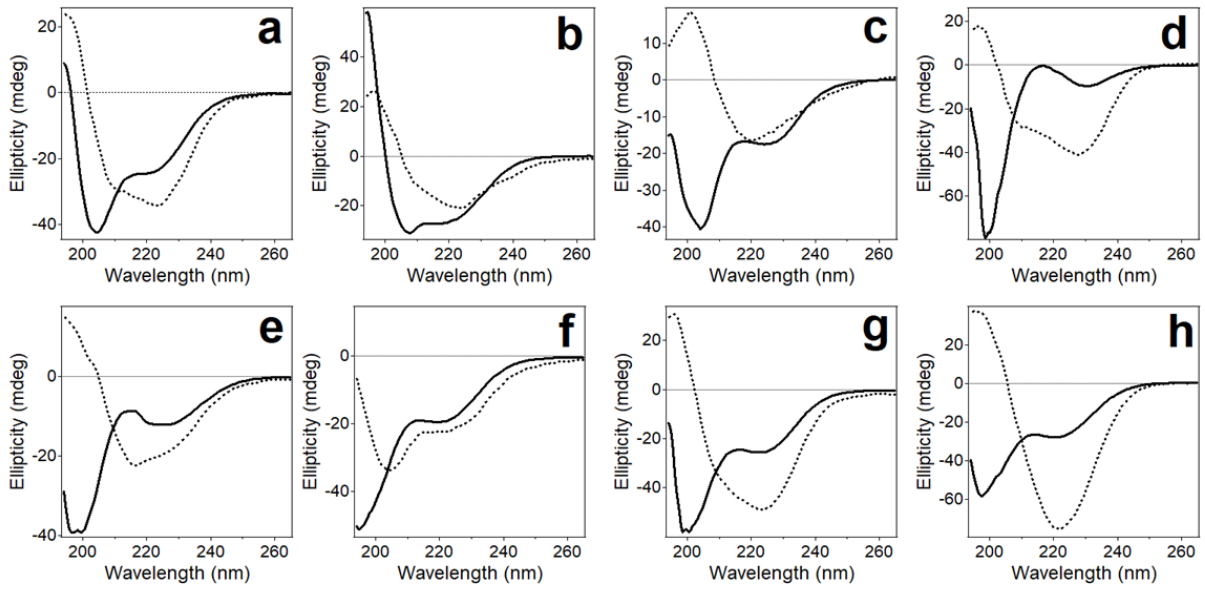

Figure 3.2. 4: CD spectra of $A\beta_{1-42}$ (a), P1 (b), P2 (c), P3 (d), P4 (e), P5 (f), P6 (g), and P7 (h) dissolved in HFIP (solid) and in dry state (dotted). The concentration of $A\beta_{1-42}$ in HFIP is 35 µM and that of the fragments is 100 µM. The spectra of dry peptides are scaled up by a factor of 5 for better comparison. Averaged from three experiments.

A deep minimum at 204 nm and a shoulder around 220 nm (Figure 3.2.4) were generated for the CD spectrum of the full-length $A\beta_{1-42}$ peptide in HFIP, suggesting the presence of type I and II β-turns, β-strand, and possibly α-helix conformations [102,121]. CD spectra of seven peptide fragments exhibited two negative ellipticities as well. CD spectra of seven peptide fragments exhibited two negative ellipticities as well. The stronger component arisen in the 205-208 nm region (P1 and P2) or 195-200 nm region (P3 through P7) (Figure 3.2.4b-h), appointed to β-turn and unordered structures, respectively [91,99-100]. Between 220 and 230 nm, the weaker component was detected which can be assigned to α-helix, β -turn and β-strand conformations.

By desiccation the solvent was removed and CD spectra of dry peptides were measured. Upon drying the structure of each peptide changes significantly. $A\beta_{1-42}$ adopted mostly α-helical structure, demonstrated by a negative component at 223 nm and weaker one at 208 nm, which are produced by the n-π^* and π-π^* electronic transitions [100,102]. The similar CD spectra were observed for P1, P3, and P6. The weaker intensity of the π-π^* transition can be accredited to a more flexible or distorted α-helix [102]. For peptides P4 and P5, the π-π^* transition was stronger, suggesting the formation of more stable α-helix in CD spectra. Just one component around 220-223 nm was shown for dry peptides P2 and P7, which is most likely to represent type-I β-turn and β-strand structures [99,121].

The aqueous buffer was added to the peptides in dry state and structural transitions were observed by recording of consecutive CD spectra.

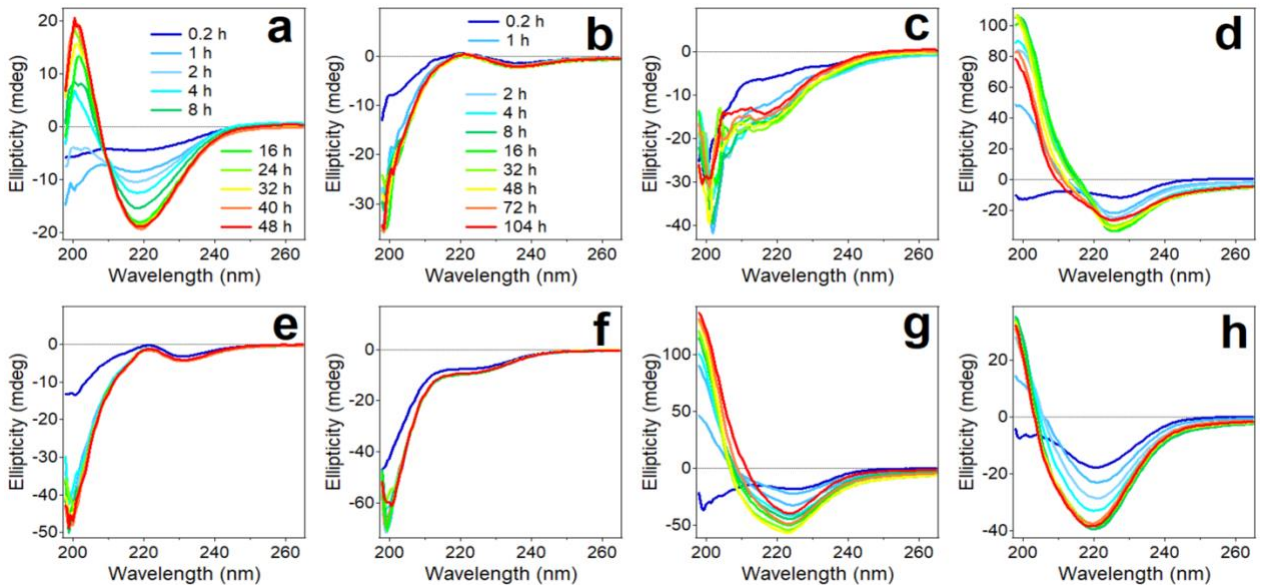

Figure 3.2. 5: CD spectra of 50 µM $A\beta_{1-42}$ (a) and 100 µM of peptides P1 (b), P2 (c), P3 (d), P4 (e), P5 (f), P6 (g), and P7 (h) constantly stirred by a tube rotator in buffer (25 mM NaCl, 25 mM phosphate, pH 7.2) for time periods indicated in panel (a) for $A\beta_{1-42}$ and in panel (b) for all fragments. All measurement were conducted at 25°C. Average data from three independent experiments.

Initially, the CD spectra showed a shallow negative band around 217 nm for $A\beta_{1-42}$, which became a well-defined band accompanied with a positive component of nearly equal intensity around 200 nm upon incubation in buffer for up to 48 hours, clearly indicating formation of β-sheet structure (Figure 3.2.5a). The peptide fragments were examined for longer time since their structural transition occurred at slower rate. Peptide fragments P1, P2, P4, and P5 exhibit strong negative ellipticity around 200 nm and weaker one between 225 and 235 nm (217 nm for P2), indicating these peptides assume mostly unordered conformation with fractions of β-turn/β-strand structures (Figure 3.2.5 b,c,e,f). On the other hand, peptides P3, P6, and P7 readily adopted defined secondary structures within less that 1 hour (Figure 3.2.5 d,g,h). The CD spectra of these three peptide fragments exhibit a negative *n*-π* band around 220-225 nm of moderate

intensity and strong positive ellipticity in the π-π* region (<200 nm). These spectral features can be assigned to twisted β-sheet structure, as the intense π-π* transition is indication of twisted β-strands, and the n-π* band can be significantly red-shifted depending on the degree of strand twist [91,99,100,102,122,123]. Since the long optical path-length (4mm) of the cuvette was used for simultaneous light scattering and fluorescence measurements with CD spectra, the excessive noise below 200 nm was observed. Nevertheless, this does not undermine above interpretations of CD spectra in terms of peptides' structural features.

From FTIR and CD measurements, some differences have been observed in peptide structures, such as different relative contents of β-turn and irregular structures. This divergence might occur due to non-identical sample preparation and handling protocols, as Aβ structure is exquisitely sensitive to sample preparation conditions, including the method of sample stirring [94]. Furthermore, both N-terminal acetylation and C-terminal amidation initiate additional amide bonds that generate FTIR signal in the unordered region, i.e. between 1650 and 1638 cm^{-1}. Nevertheless, both FTIR and CD data uncover important common structural trends of these peptide fragments, i.e., P3, P6, and P7 stand out by displaying strong β-sheet propensity, resembling the parent peptide $A\beta_{1-42,}$ whereas other peptides P1, P2, P4, and P5 incline to stay in β-turn or unordered conformations.

3.2.3 Aggregation and Fibrillogenesis

To examine the kinetics of aggregation and fibrillogenesis of the peptides in aqueous buffer, ThT fluorescence and static light scattering at 90 degrees were monitored. To exclude sample to sample errors, these measurements were conducted in parallel with CD on same samples, which permitted analysis of structural changes, peptide aggregation and fibril formation in real time.

The indication of increase in ThT fluorescence around 480 nm when excited at 435 nm (Figure 3.2.6 a,b) suggest that without delay $A\beta_{1-42}$ underwent fibrillogenesis . By around 1 day of incubation in buffer with constant stirring on a rotary mixer, ThT fluorescence was reached saturated state. At 550 nm light scattering increased with steeper initial rate and approached saturation by 10-20 hours of incubation (Figure 3.2.6 c,d). The difference in the initial kinetics of fluorescence and light scattering may reflect rapid formation of non-fibrillar aggregates that do not bind ThT.

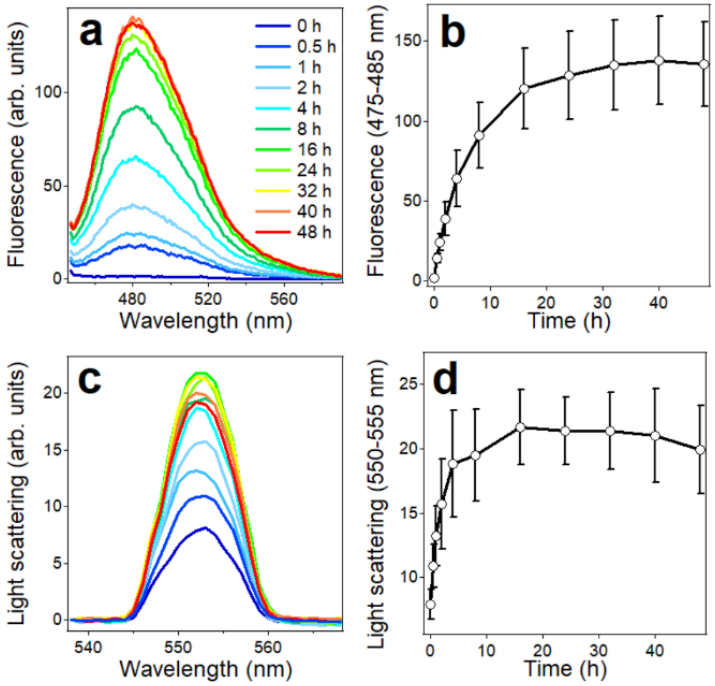

Figure 3.2. 6: ThT fluorescence with excitation at 435 nm (a) and light scattering with incident light at 550 nm (c) of 35 µM $A\beta_{1-42}$ in buffer (25 mM NaCl, 25 mM Na,K-phosphate, pH 7.2) stirred by a tube rotator for time periods indicated in panel (a). Time dependence of ThT fluorescence averaged between 475 and 485 nm and of light scattering averaged between 550 and 555 nm are presented in panels (b) and (d), respectively. Average data from three independent experiments.

A very weak ThT fluorescence was monitored for peptide fragments P1, P2, P4, and P5 (Figure 3.2.7a,b,d,e). Peptides P3 and P6 produced higher level of ThT fluorescence, and peptide 7 constructed maximum ThT fluorescence (Figure 3.2.7c,f,g), unraveling a sequence of fibrillogenesis propensity P7 > P6 ≈ P3 >> P4 ≈ P5 ≈ P2 ≈ P1 ≈ 0 (Figure 3.2.7h).

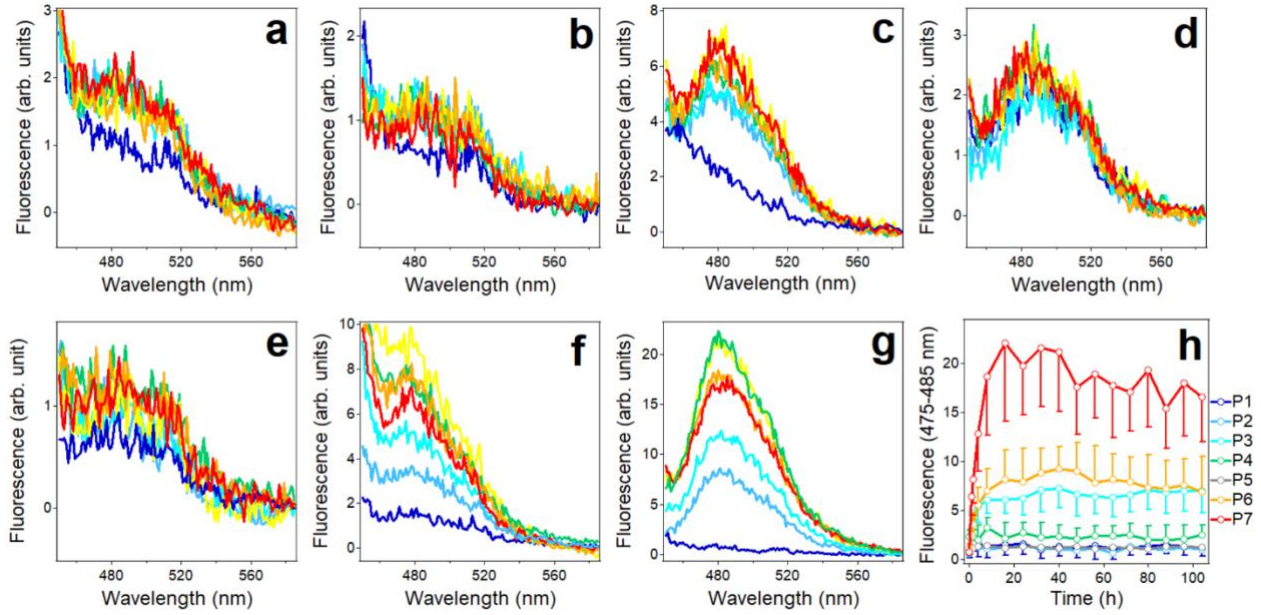

Figure 3.2. 7: ThT fluorescence spectra of P1, P2, P3, P4, P5, P6, and P7 (panels 1 through g, respectively) with excitation at 435 nm, at 25^{o}C. Time of incubation of peptide samples in buffer (25 mM NaCl, 25 mM Na,K-phosphate, pH 7.2) at 100 µM concentration with constant stirring by a tube rotator is as follows: 0.1 h (dark blue), 2.0 h (light blue), 4.0 h (turquoise), 16.0 h (green), 40.0 h (yellow), 64.0 h (orange), 104.0 h (red). Panel h shows the time dependence of ThT fluorescence averaged between 475 and 485 nm for all seven peptides. Average data from three independent experiments. Error bars are shown only for P1, P3, P4, P6, P7 to maintain clarity. Error bars for P2 and P5 are of similar magnitude as for those of P1 and P4.

Contemporary light scattering measurements implied relatively weak signal for peptides P1, P2, P4, and P5 and about 3-fold higher signal for peptides P3, P6, and P7 (Figure 3.2.8).

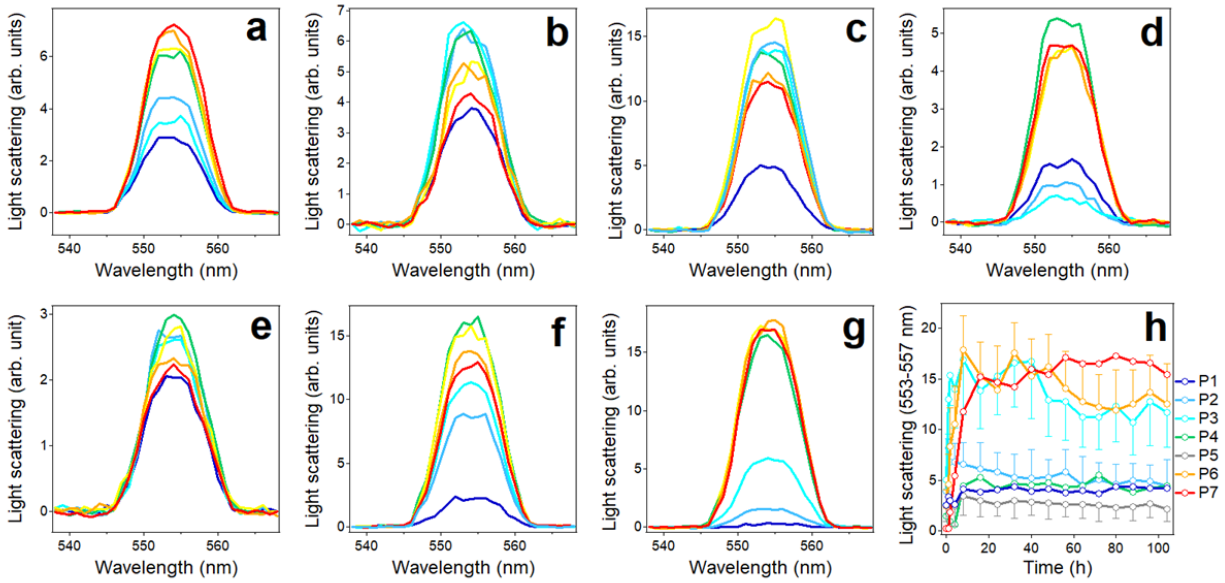

Figure 3.2. 8: Time progression of light scattering spectra of peptides P1 (a), P2 (b), P3 (c), P4 (d), P5 (e), P6 (f), and P7 (g) at 100 µM. Color code in panels (a) through (g) is the same as in Figure 3.2.7. Panel (h) shows time course of light scattering for all seven peptides. Standard deviation bars from three experiments are only shown for selected peptides to maintain clarity. Error bars for other peptides are of similar magnitude.

The peptide fragments P1,P2,P4 and P5 exhibit little ThT fluorescence but substantial light scattering indicates the formation of non-fibrillar aggregation. Greater level of ThT fluorescence by P7 compared to P3 and P6 but comparable light scattering (Figure 3.2.7h and 3.2.8h) insinuates a more extensive ThT binding capacity of P7, probably due to its higher hydrophobicity and/or a larger number of amino acid residues. Generally, these data provide

evidence that peptides P3, P6, and P7 possess significant aggregation/fibril formation capability as compared to the other four Aβ peptide fragments. In concurrence with structural data, it appears that the aggregation/fibrillogenesis property of these peptides correlates with their β-sheet formation ability.

3.2.4 Effects of Aβ Fragments on Aβ Fibrillogenesis

If the strong fibrillogenesis propensity were demonstrated by some of peptide fragments, they might be capable of intercalate into the assemblies of the full-length parent peptide by binding to respective stretches and thereby impede with its aggregation. Fibrillogenesis of $A\beta_{1\text{-}42}$ was measured in the absence and presence of all seven peptide fragments at two-fold molar excess to test this hypothesis.

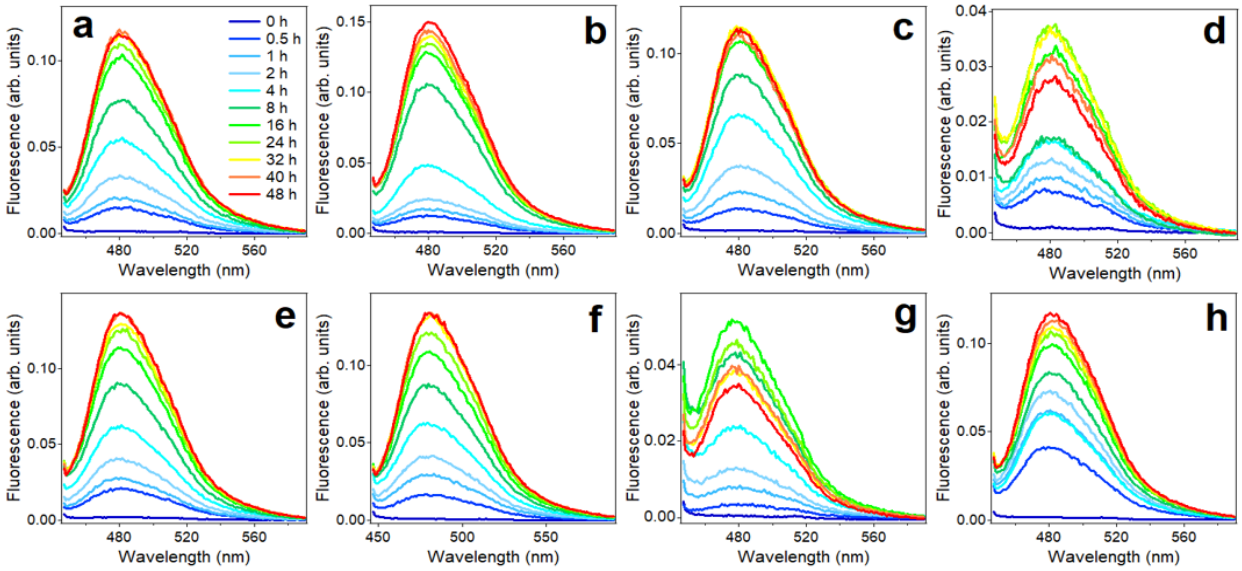

Figure 3.2. 9: Time progression of ThT fluorescence spectra (excitation= 435 nm) of $A\beta_{1\text{-}42}$ in aqueous buffer at 35 μM (a), and with 70 μM of P1 (b), P2 (c), P3 (d), P4 (e), P5 (f), P6 (g), and P7 (h). Buffer: 25 mM NaCl + 25 mM phosphate (pH 7.2).

In the presence of peptides P1, P2, P4, P5, and P7, ThT fluorescence of $A\beta_{1-42}$ samples progressively increased and levelled off by 48 hours of incubation with little effect of these fragments (Figure 3.2.9 b,c,e,f,h). The intensity values for wavelength 480 nm vs time of incubation were plotted for every sample. Here it has been observed that the fluorescence intensity gradually increased over increase of incubation time for samples of $A\beta_{1-42}$ mixed with P1, $A\beta_{1-42}$ mixed with P2, $A\beta_{1-42}$ mixed with P4, $A\beta_{1-42}$ mixed with P5, $A\beta_{1-42}$ mixed with P7 and reach more than 0.1 arbitrary units where $A\beta_{1-42}$ mixed with P3 and $A\beta_{1-42}$ mixed with P6 samples fluorescence around 480 nm were increase initially up to incubation for 16 hours but by 24 hours of incubation the intensity decreases get saturated for further observation by remaining the intensity around 0.025 arbitrary units. In contrast, P3 and P6 strongly reduced the level of ThT fluorescence (Figure3.2.9 d,g). Despite relatively large standard deviations among three experiments, which reflects the inherent polymorphism of Aβ, the distinctive inhibitory effects of P3 and P6 was statistically significant (Figure 3.2.10).

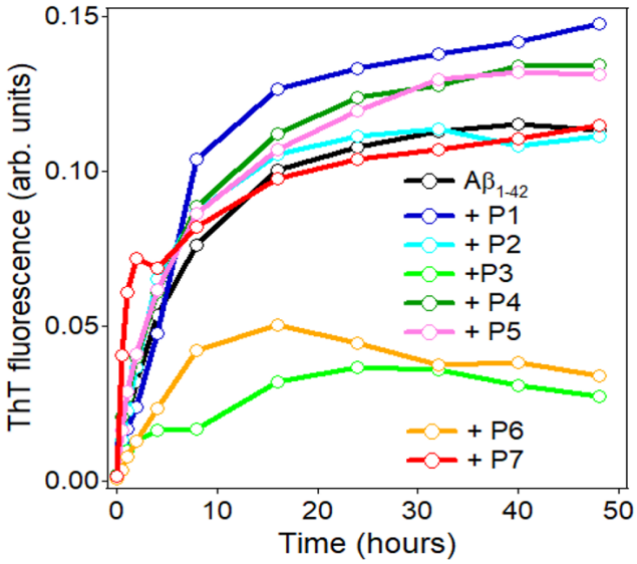

Figure 3.2. 10: Time dependence of ThT fluorescence at 480 nm (excitation= 435 nm) of $A\beta_{1-42}$ alone and in the presence of 2-fold molar excess of peptides 1 to 7, as indicated. Buffer: 25 mM NaCl + 25 mM phosphate, pH 7.2.

Quantitative evaluation of inhibition of $A\beta_{1-42}$ fibril formation by peptide fragments was performed by calculating the inhibition percentages (*IP*) for each fragment.

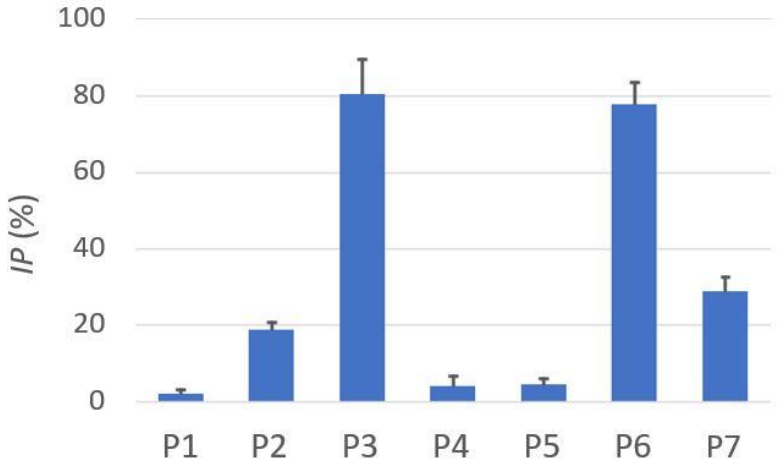

Figure 3.2. 11: Inhibition percentages for P1 through P7 calculated based on ThT fluorescence data (Figures 3.2.6, 3.2.7, 3.2.10) averaged between 32 and 48 hours of incubation of $A\beta_{1-42}$ alone and with each peptide fragment at 2-fold molar excess in buffer (25 mM NaCl, 25 mM Na,K-phosphate, pH 7.2). See details in Materials and Methods.

P3 and P6 strongly inhibited $A\beta_{1-42}$ fibrillization by 80.5±9.0% and 77.7±5.8%, respectively (Figure 3.2.11). Peptides P2 and P7 exhibited moderate inhibitory potencies (*IP* = 18.8±2.1% and 28.7±3.8%, respectively), and the other three peptides (P1, P4, and P5) were not potent inhibitors (*IP* < 5.0%).

This work details an analysis of structural and aggregation propensities of $A\beta_{1-42}$ fragments and their effects on $A\beta_{1-42}$ fibrillogenesis. The results facilitate a better understanding of segment-specific properties of $A\beta_{1-42}$ and distinguish peptide fragments capable of inhibiting its aggregation. We selected 10 to 12-residue overlapping fragments because fragments shorter than 10 residues might be incapable to demonstrate vigorous secondary structure formation and fibrillogenesis abilities because of insufficient length. Although short Aβ fragments comprising

6-8 residues have been shown to adopt parallel or antiparallel β-sheets in crystal form [124,125], the hydrophobic C-terminal sequences of $A\beta_{1-42}$ containing eight amino acid residues, as well as an 11-residue stretch ($A\beta_{32-42}$), did not aggregate into β-sheet fibrils in aqueous buffer even at concentrations exceeding 100 μM [83]. On the other hand, use of overlapping sequences was important for characterization of segments at boundaries of consecutive stretches; properties of the boundary between P(*i*) and P(*i+2*) were reflected in P(*i+1*), which covers the C- and N-termini of flanking sequences.

Peptides P1 and P2 represent the N-terminus of Aβ, which has been consistently found in unordered conformation in the context of $A\beta_{1-40}$ or $A\beta_{1-42}$ [94,118,120,126]. The $A\beta_{1-8}$ fragment was found in extended coil confirmation in complex with a monoclonal antibody [94]. Despite its proposed role in stabilizing Aβ fibrils [127], above data and our findings indicate that the N-terminus of Aβ is intrinsically unordered and unable to undergo fibrillogenesis. This feature is evidently related with the amino acid composition of these segments; the paucity of nonpolar side chains and the excess negative charge (pI 4.54 and 5.72 for P1 and P2, respectively) may inhibit aggregation due to electrostatic repulsion and absence of hydrophobic interactions. P1 is also a poor inhibitor of $A\beta_{1-42}$, whereas P2 demonstrates moderate inhibitory activity (Figure 3.2.11), which probably stems from its C-terminal part, as P3 is highly aggregation prone and a potent inhibitor of $A\beta_{1-42}$ fibrillogenesis.

The P3 segment corresponds to one of the two major β-strands of $A\beta_{1-40}$ fibrillar structure $A\beta_{1-42}$ [94] (Figure 3.2.1). The whole P3 sequence or at least its central part are in β-strand conformation in fibrils formed by of $A\beta_{1-42}$ as well [118-120] (Figure 3.2.1). P3 has one glutamic acid (Glu) and one lysine (Lys) residues and nearly zero net charge (pI = 7.01). These features

would allow the peptide to form β-strand-like non-H-bonded out of register aggregates in antiparallel sense with oppositely charged side chains facing each other, as shown in Figure 3.2.12.

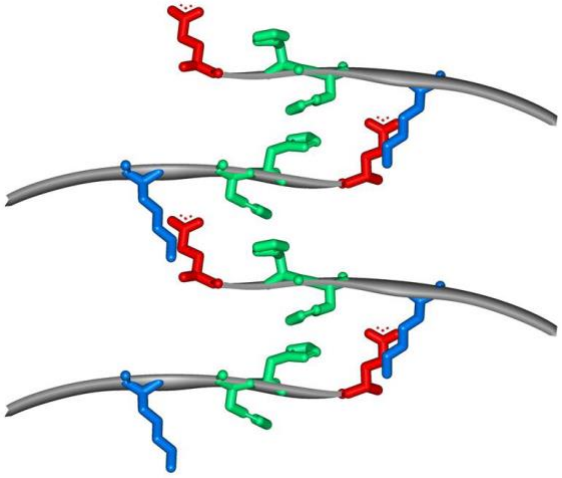

Figure 3.2. 12: Proposed mode of aggregation of P3. Red, blue, and green side chains are those of Glu11, Lys16, and His 13 and 14. All other side chains are omitted for clarity. The monomer β- strand structure is shown as a gray ribbon. The fibril would grow by means of intermolecular H-bonding perpendicular to the plane of the image.

This arrangement will juxtapose one Glu-Lys pair and one histidine pair between strands so the structure will be stabilized by Glu-Lys salt bridges and π-π stacking interactions between histidines [134,135]. As a fraction of imidazole side chains will be protonated due to the close-to-neutral pK = 6.3±0.1 [136], His-His attraction will be further strengthened by nucleophile-electrophile interactions. This structure may grow laterally beyond tetramer until decreasing internal energy is compensated by decreasing entropy at a minimum of free energy. The fibril will grow by means of parallel β-sheet formation stabilized by H-bonding perpendicular to the plane of side chains. The nonpolar overhangs may form turn or parallel β-sheet structure

stabilized by hydrophobic interactions and π-π stacking interactions between C-terminal phenylalanines [134]. In order to test the model of P3 aggregation, assuming the interaction in stabilized by electrostatic forces. It can be tested it in two different ways:

First, The observation of fibrillogenesis at low pH. At pH 3, the negative charge of Glu (pI 3.22) side chain will be neutralized and the Glu-Lys ionic bond will be eliminated.

The second way would be using high salt concentration, such as a buffer containing same concentration of phosphate buffer and 1 M NaCl. Increase in salt concentration at 1.0 M caused a decrease in protein solubility. At very high salt concentrations, the increase in surface tension of water creates competition for hydration between protein and salt ions. Salt removes the necessary layer of water molecules from the surface of the protein and ultimately denatures the protein.

In earlier observations of dimer formation by $A\beta_{10-23}$ peptide, it has exhibited that the peptide develops into β-sheet fibrillar structure [137]. FTIR data (Figure 3.2.3d) show a low frequency (1623 cm^{-1}) β-sheet component without a high-frequency counterpart diagnostic for antiparallel β-sheet, consistent with parallel β-sheet formation. Figures 3.2.9, 3.2.10, and 3.2.11 show that P3 forms fibrils and substantially blocks the fibrillogenesis of $A\beta_{1-42}$. Inhibition of $A\beta_{1-42}$ fibrillogenesis presumably occurs through intercalation of P3 aggregates between $A\beta_{1-42}$ molecules and/or binding of P3 to the homologous or other segments of $A\beta_{1-42}$. Consistent with our findings, it was reported earlier that Aβ segment 11-17 (EVHHQKL), i.e. 0.7 part of P3, but not other Aβ-derived short peptides, effectively blocked $A\beta_{1-40}$-induced Ca^{2+} influx into cultured cells possibly by inhibiting aggregation of $A\beta_{1-40}$ into a membrane pore-forming structure [129]. P3 is apparently able to bind not only to various parts of Aβ but to other biomolecules as well. For example, the 12-18 stretch of Aβ (VHHQKLV) has been found to bind to heparin and thereby mediate the effects of heparin on Aβ plaque formation [138].

Aβ region corresponding to P4 ($A\beta_{16-25}$) contains the central hydrophobic core 17-LVFFA-21 that is deemed to be important for Aβ aggregation. Molecular modeling and a variety of experimental studies have shown that the $A\beta_{16-22}$ fragment (KLVFFAE) forms antiparallel in-register β-sheet stabilized by nonpolar contacts between the central segment and ionic interactions between the side chains of N- and C-terminal Lys and Glu residues [123,128,139-140]. Monomeric $A\beta_{16-25}$ was in coil or extended β-strand-like conformation and transitioned into antiparallel β-sheet through intermediate α-helical structure [141]. Our data show unordered plus β-strand conformation for P4 in HFIP in monomeric form (Figure 3.2.4e) but transition to β-sheet in aqueous buffer is not observed (Figures 3.2.3e and 3.2.4e). This difference seemingly results from the supplementary three residues in P4 compared to $A\beta_{16-22}$. The presence of an additional anionic side chain of aspartic acid at position 23 results in excess negative charge and a low pI of 4.37 (Figure 3.2.1). These considerations suggest that long-range electrostatic repulsion between short peptides may interfere with initial peptide aggregation and subsequent fibrillization. Furthermore, an analogue of $A\beta_{16-22}$ with N-methyl amino acids in alternating positions was a potent inhibitor of $A\beta_{1-40}$ fibrillogenesis unlike the unmodified peptide [133], which is coherent with our data of negligible inhibitory effect of P4 on $A\beta_{1-42}$ fibril formation (Figures 3.2.10h and 3.2.11).

P5 encompasses the Aβ region that forms a loop between two major β-strands of $A\beta_{1-40}$ fibrils characterized by two- or three-fold symmetry [94] and has been viewed as a folding nucleus for Aβ [143,144]. This region is mostly in loop conformation in fibrils of $A\beta_{1-42}$ as well [118-120] (Figure 3.2.1). In complex with an affibody protein, $A\beta_{1-40}$ was found in a β-hairpin conformation with residues 24-29 forming a loop between two β-strands but without the Asp_{23}-

Lys_{28} salt bridge present in $A\beta_{1-40}$ fibrils of two-fold symmetry [145]. The isolated P5 segment itself was mostly unordered [83] or formed a loop with a central β-turn structure formed by residues 24 and 27 and stabilized by ionic interactions of Lys_{28} with Glu_{22}/Asp_{23} and nonpolar contacts between Val_{24} and Lys_{28} [143]. P5 did not undergo aggregation in aqueous medium [83,143], in accord with sequence-based calculation of low aggregation propensity. Transmission electron microscopic studies shown relatively large (25-120 nm) globular particles produced by P5 with uncapped termini whereas the N-acetylated/C-amidated peptide formed smaller particles, implying low aggregation tendency [144]. Our FTIR data for P5 display broad amide I band dominated by signal in the1670-1640 cm^{-1} range Figure 3.2.3f), revealing mostly unordered/turn structure of the peptide. This is confirmed by CD spectra with a deep minimum around 200 nm and a shallow negative band around 228 nm (Figure 3.2.4f). Figure 3.2.8e, h and 3.2.7e, h display negligible light scattering and ThT fluorescence in P5 peptide samples, and Figures 3.2.10h and 3.2.11 document the inability of P5 to affect $A\beta_{1-42}$ fibrillogenesis, inferring a poor potency of P5 towards homo- or hetero-aggregation.

P6 ($A\beta_{26-36}$) resembles the $A\beta_{25-35}$ peptide, which has been studied extensively due to its highly cytotoxic nature. In aqueous buffer at pH 4.0-5.5, the $A\beta_{25-35}$ peptide underwent concentration-dependent unordered-to-β-sheet transition whereas its C-amidated counterpart was in random coil state [146]. At close to neutral pH, the N-acetylated/C-amidated peptide attained β-sheet/β-turn structures [147]. In detergent micelles and in HFIP/water (80/20) environment, $A\beta_{25-35}$ was α-helical in the C-terminal region and less ordered or turn conformation in the N-terminus (25-28), and in HFIP/water (20/80) the C-terminus became unordered [148,149]. ThT and transmission electron microscopy assays revealed fibril formation by $A\beta_{25-35}$ [128,129] and β-sheet breaking short peptides inhibited fibrillogenesis and cytotoxicity of the peptide [129].

Slight sequence differences in this region of Aβ resulted in significant differences in structural and aggregation properties. Biophysical and computational studies produced $A\beta_{26\text{-}36}$ and $A\beta_{25\text{-}35}$ structural models as β-hairpins containing two short β-strands separated by a turn [112], in accord with our FTIR data (Figure 3.2.3g). P6 formed β-sheet structure in aqueous buffer with red-shifted (~220 nm) n-π* CD band and exhibited higher fibril formation capability than similar undecapeptides $A\beta_{25\text{-}35}$ and $A\beta_{24\text{-}34}$ [150], consistent with our results (Figures 3.2.4g and 3.27h).

P7 ($A\beta_{31\text{-}42}$) represents the most hydrophobic C-terminal stretch of Aβ and plays an important role in its aggregation into β-sheet oligomers and fibrils [83,132]. Dynamic light scattering experiments identified two populations of $A\beta_{1\text{-}42}$ aggregates with hydrodynamic radii (R_H) 8-12 nm and 20-60 nm, which upon elongated incubation in buffer exceeded 500 nm, while the P7 fragment formed large aggregates with R_H around 100 nm [83,132]. In combination, P7 affected the aggregation of $A\beta_{1\text{-}42}$ in a nontrivial way; it increased the abundance of larger particles but reduced the rate of their formation. Molecular modeling simulations showed that P7 intercalates into $A\beta_{1\text{-}42}$ aggregates and thereby inhibits formation of toxic assemblies of $A\beta_{1\text{-}42}$ [132]. The CD experiments showed that structural transitions of C-terminal fragments of $A\beta_{1\text{-}42}$ were concentration dependent; at 62 μM, P7 gradually transitioned from unordered state to β-sheet structure during 96 hours of incubation in buffer and formed fibrils [83], in very consistent with our finding (Figures 3.2.4h and 3.2.7g,h).

The characterization of the intrinsic aggregation and structural properties of overlapping peptide segments throughout the $A\beta_{1\text{-}42}$ sequence and the effects of these fragments on $A\beta_{1\text{-}42}$ fibrillogenesis are done here. Though aforementioned studies have exploited a similar approach and have focused on certain parts of $A\beta_{1\text{-}42}$, such as the C-terminal hydrophobic stretch,

systematic dissection and analysis of the whole $A\beta_{1-42}$ sequence has not been reported. Or data identify Aβ fragments that are capable of self-aggregation and β-sheet structure formation and substantially inhibit fibrillogenesis of $A\beta_{1-42}$, presumably by intervention into forming aggregates or prevention of efficient intermolecular contacts between $A\beta_{1-42}$ molecules. However, the self-aggregation/β-sheet propensities of the peptide fragments are not universally correlated to the inhibitory effect of fragments on $A\beta_{1-42}$ fibril formation. For example, P7, the most hydrophobic segment that undergoes efficient fibrilization (Figure 3.2.10h) and β-sheet formation (Figures 3.2.3h and 3.2.4h) is a relatively week inhibitor of $A\beta_{1-42}$ fibrillization of (Figures 3.2.10h and 3.2.11). Finally based on our overall findings, it can be said that peptide fragments with high homo-aggregation propensity prefer self-association rather than forming hetero-aggregates with the full-length peptide.

CHAPTER 4: CONCLUSION

Here, the first work aims to clarify the structural transformation of $A\beta_{1-40}$ and $pEA\beta_{3-40}$ during fibril formation, either separately or in equimolar combination. Fluorescence data from ThT indicate that $pEA\beta_{3-40}$ rapidly forms a small fraction of fibers, which tend to grow slowly, and when combined with $A\beta_{1-40}$, it can inhibit fibril formation. The CD data have shown that when dissolved in HFIP and in the dry state, both peptides exhibit an α-helix structure and are converted to a β-sheet structure in an aqueous buffer. Nevertheless, $pEA\beta_{3-40}$ acquired a unique conformation, possibly involving an α-helical structure. The combination of the two peptides exhibited a reduced fraction of the β sheet, consistent with the weaker ThT fluorescence. Isotope-edited FTIR spectroscopy analyzes the structural transition of each peptide when combined in a sample. The shifted frequency of amide I indicates that the unmodified and pyroglutamylated peptides form an intertwined structure and a mutual structural effect, that is, inhibition of the β-sheet / α-helix ratios. The FTIR data confirmed the retention of the residual α-helical structure of $pEA\beta_{3-40}$ in individual and in the combined sample during hydration. Because mature fibrils are composed of cross β-sheet structure, the presence of heterogeneous secondary structures (including α-helix) will hinder fibril formation, as shown by ThT fluorescence data, and and will favor a longer lifetime for smaller assemblies that are known to be more toxic. Therefore, our data provide a molecular explanation for the hypertoxicity of pEAβ alone and in combination with unmodified Aβ.

The second work has done based on the characterization the intrinsic aggregation and structural characteristics of overlapping peptides in the complete sequence of $A\beta_{1-42}$, and the influence of these fragments on the formation of $A\beta_{1-42}$ fibrils. FTIR data shows that the full-length $A\beta_{1-42}$ exhibit β-sheet and β-turn/loop conformations in the presence aqueous environment, and it

indicates that the intermolecular H-bonding, formation of turn/loop structures which leads aggregation and fibrillogenesis. Where peptide fragments P3, P6, and P7 display β-sheet structure where the other four peptides (P1, P2, P4, P5) incline to adopt β–turn/loop conformations. The CD data established the findings of these peptide fragments, that P3, P6 and P7 stand out for showing a strong β-sheet propensity, comparable to the parent peptide $A\beta_{1-42}$, whilst other peptides P1, P2, P4 and P5 incline to remain in β-turn or disorderly conformation. ThT fluorescence and light scattering data provide evidence that, compared with the other four Aβ peptide fragments, peptides P3, P6, and P7 have significant aggregation ability. Based on structural data, the aggregation/fibrillation properties of these peptides appear to be related to their ability to form β-sheets. Fibrillogenesis of $A\beta_{1-42}$ was monitored in the absence and presence of all seven peptide fragments at two-fold molar excess to test the hypothesis of if certain peptide fragments exhibit a strong tendency to fibrillate, they may be able to be embedded in the full-length parent peptide segment by binding to the corresponding fragments to inhibit their aggregation. This observation indicates that P3 and P6 strongly inhibit $A\beta_{1-42}$ fibrillation, in which peptides P2 and P7 show moderate inhibitory potency, while the other three peptides (P1, P4, and P5) are not effective inhibitors, indicating that all three peptides (P1, P4 and P5) are not effective inhibitors and there is no universal correlation between them. Fragment self-aggregation / β-sheet tendency and inhibition of $A\beta_{1-42}$ fibril formation. However, effective inhibition of $A\beta_{1-42}$ aggregation by peptides P3 and P6 may help to develop new DNA, mRNA, or peptide-based anti-AD treatment strategies.

REFERENCE

[1] Ferreira D, Nordberg A, Westman E. Biological subtypes of Alzheimer disease: a systematic review and meta-analysis. Neurology. 2020;94(10):436-448.

[2] Thal, D. R., Walter, J., Saido, T. C., & Fändrich, M. (2015) Neuropathology and biochemistry of Aβ and its aggregates in Alzheimer's disease. Acta neuropathologica, 129(2), 167-182.

[3] Masters, C. L., & Selkoe, D. J. (2012) Biochemistry of amyloid β-protein and amyloid deposits in Alzheimer disease. Cold Spring Harbor Perspectives in Medicine, 2(6), a006262.

[4] Musiek, E. S., & Holtzman, D. M. (2015) Three dimensions of the amyloid hypothesis: time, space and 'wingmen'. Nature Neuroscience, 18(6), 800.

[5] Hardy, J., & Allsop, D. (1991) Amyloid deposition as the central event in the aetiology of Alzheimer's disease. Trends in Pharmacological Sciences, 12, 383-388.

[6] Lal, R., Lin, H., & Quist, A. P. (2007) Amyloid beta ion channel: 3D structure and relevance to amyloid channel paradigm. Biochimica et Biophysica Acta (BBA)-Biomembranes, 1768(8), 1966-1975.

[7] Arispe, N., Diaz, J. C., & Simakova, O. (2007) Aβ ion channels. Prospects for treating Alzheimer's disease with Aβ channel blockers. Biochimica et Biophysica Acta (BBA)-Biomembranes, 1768(8), 1952-1965.

[8] Gillman, A. L., Jang, H., Lee, J., Ramachandran, S., Kagan, B. L., Nussinov, R., & Teran Arce, F. (2014) Activity and architecture of pyroglutamate-modified amyloid-β (AβpE3-42) pores. The Journal of Physical Chemistry B, 118(26), 7335-7344.

[9] Ferreiro, E., Oliveira, C. R., & Pereira, C. M. (2008) The release of calcium from the endoplasmic reticulum induced by amyloid-beta and prion peptides activates the mitochondrial apoptotic pathway. Neurobiology of Disease, 30(3), 331-342.

[10] Ferreiro, E., Baldeiras, I., Ferreira, I. L., Costa, R. O., Rego, A. C., Pereira, C. F., & Oliveira, C. R. (2012) Mitochondrial-and endoplasmic reticulum-associated oxidative stress in Alzheimer's disease: from pathogenesis to biomarkers. International Journal of Cell Biology, vol. 2012, Article ID 735206, 23 pages.

[11] Demuro, A., & Parker, I. (2013) Cytotoxicity of intracellular aβ42 amyloid oligomers involves Ca^{2+} release from the endoplasmic reticulum by stimulated production of inositol trisphosphate. Journal of Neuroscience, 33(9), 3824-3833.

[12] Resende, R., Ferreiro, E., Pereira, C., & De Oliveira, C. R. (2008) Neurotoxic effect of oligomeric and fibrillar species of amyloid-beta peptide 1-42: involvement of endoplasmic reticulum calcium release in oligomer-induced cell death. Neuroscience, 155(3), 725-737.

[13] Reddy, P. H., Tripathi, R., Troung, Q., Tirumala, K., Reddy, T. P., Anekonda, V., Shirendeb, U.P., Calkins, M.J., Reddy, A.P., Mao, P. (2012) Abnormal mitochondrial dynamics and synaptic degeneration as early events in Alzheimer's disease: implications to mitochondria-targeted antioxidant therapeutics. Biochimica et Biophysica Acta (BBA)-Molecular Basis of Disease, 1822(5), 639-649.

[14] Pagani, L., & Eckert, A. (2011) Amyloid-Beta interaction with mitochondria. International Journal of Alzheimer’s Disease, vol. 2011, Article ID 925050, 12 pages.

[15] Correia, S.C., Santos, R.X., Santos, M.S., Casadesus, G., Lamanna, J.C., Perry, G., Smith, M.A. & Moreira, P.I. (2013) Mitochondrial abnormalities in a streptozotocin-induced rat model of sporadic Alzheimer's disease. Current Alzheimer Research, 10(4), 406-419.

[16] Chi, T. Y., Wang, L. H., Ji, X. F., Shen, L., & Zou, L. B. (2013) Protective effect of xanthoceraside against β-amyloid-induced neurotoxicity in neuroblastoma SH-SY5Y cells. Journal of Asian Natural Products Research, 15(9), 1013-1022.

[17] Lei, H., Zhao, C. Y., Liu, D. M., Zhang, Y., Li, L., Wang, X. L., & Peng, Y. (2014) L-3-n-butylphthalide attenuates β-amyloid-induced toxicity in neuroblastoma SH-SY5Y cells through regulating mitochondrion-mediated apoptosis and MAPK signaling. Journal of Asian Natural Products Research, 16(8), 854-864.

[18] Malinow, R. (2012) New developments on the role of NMDA receptors in Alzheimer's disease. Current Opinion in Neurobiology, 22(3), 559-563.

[19] Kim, T., Vidal, G. S., Djurisic, M., William, C. M., Birnbaum, M. E., Garcia, K. C., Hyman, B.T., Carla, J. et al. (2013) Human LilrB2 is a β-amyloid receptor and its murine homolog PirB regulates synaptic plasticity in an Alzheimer's model. Science, 341(6152), 1399-1404.

[20] Benilova, I., Karran, E., & De Strooper, B. (2012) The toxic Aβ oligomer and Alzheimer's disease: an emperor in need of clothes. Nature Neuroscience, 15(3), 349.

[21] Agostinho P, Pliassova A, Oliveira CR & Cunha RA (2015) Localization and trafficking of amyloid-b protein precursor and secretases: impact on Alzheimer's disease. J Alzheimers Dis 45(2015), 329–347.

[22] Naldi, M., Fiori, J., Pistolozzi, M., Drake, A. F., Bertucci, C., Wu, R., Mlynarczyk, K., Filipek, S., Simone, A.D. et al. (2012) Amyloid β-peptide 25–35 self-assembly and its inhibition: a model undecapeptide system to gain atomistic and secondary structure details of the Alzheimer's disease process and treatment. ACS Chemical Neuroscience, 3(11), 952-962.

[23] Spies, P. E., Verbeek, M. M., van Groen, T., & Claassen, J. A. (2012) Reviewing reasons for the decreased CSF Abeta42 concentration in Alzheimer disease. Front Biosci, 17, 2024-2034.

[24] Serpell, L. C. (2000) Alzheimer's amyloid fibrils: structure and assembly. Biochimica et Biophysica Acta (BBA)-Molecular Basis of Disease, 1502(1), 16-30.

[25] Estrada, L. D., & Soto, C. (2006) Inhibition of protein misfolding and aggregation by small rationally-designed peptides. Current pharmaceutical design, 12(20), 2557-2567.

[26] Connelly, L., Jang, H., Teran Arce, F., Capone, R., Kotler, S. A., Ramachandran, S., Kagan, B.L., Nussinov, R. & Lal, R. (2012) Atomic force microscopy and MD simulations reveal pore-like structures of all-D-enantiomer of Alzheimer's β-amyloid peptide: relevance to the ion channel mechanism of AD pathology. The Journal of Physical Chemistry B, 116(5), 1728-1735.

[27] Supnet, C., Grant, J., Westaway, D., & Mayne, M. (2006) Amyloid-β-(1-42) increases ryanodine receptor-3 expression and function in neurons of TgCRND8 mice. Journal of Biological Chemistry, 281(50), 38440-38447.

[28] Lin, H. A. I., Bhatia, R., & Lal, R. (2001) Amyloid β protein forms ion channels: implications for Alzheimer's disease pathophysiology. The FASEB Journal, 15(13), 2433-2444.

[29] Petkova, A. T., Ishii, Y., Balbach, J. J., Antzutkin, O. N., Leapman, R. D., Delaglio, F., & Tycko, R. (2002) A structural model for Alzheimer's β-amyloid fibrils based on experimental constraints from solid state NMR. Proceedings of the National Academy of Sciences of USA, 99(26), 16742-16747.

[30] Coles, M., Bicknell, W., Watson, A. A., Fairlie, D. P., & Craik, D. J. (1998) Solution Structure of Amyloid β-Peptide (1− 40) in a Water− Micelle Environment. Is the Membrane-Spanning Domain Where We Think It Is? Biochemistry, 37(31), 11064-11077.

[31] Alomar-Dominguez C, Dostal L, Thaler J, Putz G, Humpel C, Lederer W. Beta-amyloid peptides(1-42) and (1-40) in the cerebrospinal fluid during pregnancy: a prospective observational study. Arch Womens Ment Health. **2021** Jun;24(3):455-461.

[32] Lin, Y., Sahoo, B. R., Ozawa, D., Kinoshita, M., Kang, J., Lim, M. H., Masaki O. et al. (2019) Diverse Structural Conversion and Aggregation Pathways of Alzheimer's Amyloid-β (1-40). ACS Nano Article ASAP DOI: 10.1021/acsnano.9b01578.

[33] Anand, B. G., Prajapati, K. P., & Kar, K. (2018) Aβ1-40 mediated aggregation of proteins and metabolites unveils the relevance of amyloid cross-seeding in amyloidogenesis. Biochemical and Biophysical Research Communications, 501(1), 158-164.

[34] Baldassarre, M., Baronio, C. M., Morozova-Roche, L. A., & Barth, A. (2017) Amyloid β-peptides 1–40 and 1–42 form oligomers with mixed β-sheets. Chemical Science, 8(12), 8247-8254.

[35] Leite JP, Gimeno A, Taboada P, Jiménez-Barbero JJ, Gales L. Dissection of the key steps of amyloid-β peptide 1-40 fibrillogenesis. Int J Biol Macromol. **2020** Dec 1;164:2240-2246.

[36] Okada, Y., Okubo, K., Ikeda, K., Yano, Y., Hoshino, M., Hayashi, Y., Kiso, y., Watanabe, H.I., Naito, A. et al. (2018) Toxic Amyloid Tape: A Novel Mixed Antiparallel/Parallel β-Sheet Structure Formed by Amyloid β-Protein on GM1 Clusters. ACS Chemical Neuroscience, 10(1), 563-572.

[37] Bellomo, G., Bologna, S., Gonnelli, L., Ravera, E., Fragai, M., Lelli, M., & Luchinat, C. (2018) Aggregation kinetics of the Aβ1–40 peptide monitored by NMR. Chemical Communications, 54(55), 7601-7604.

[38] Gunn, A. P., Masters, C. L., & Cherny, R. A. (2010) Pyroglutamate-Aβ: role in the natural history of Alzheimer's disease. Int J Biochem Cell Biol, 42(12), 1915-1918.

[39] Supnet, C., & Bezprozvanny, I. (2010) The dysregulation of intracellular calcium in Alzheimer disease. Cell Calcium, 47(2), 183-189.

[40] St George-Hyslop, P. H. (2000) Molecular genetics of Alzheimer's disease. Biological Psychiatry, 47(3), 183-199.

[41] Yu, X., & Zheng, J. (2012) Cholesterol promotes the interaction of Alzheimer β-amyloid monomer with lipid bilayer. Journal of Molecular Biology, 421(4-5), 561-571.

[42] Di Scala, C., Yahi, N., Lelièvre, C., Garmy, N., Chahinian, H., & Fantini, J. (2012) Biochemical identification of a linear cholesterol-binding domain within Alzheimer's β amyloid peptide. ACS Chemical Neuroscience, 4(3), 509-517.

[43] Jawhar, S., Wirths, O., & Bayer, T. A. (2011) Pyroglutamate amyloid-β (Aβ): a hatchet man in Alzheimer disease. Journal of Biological Chemistry, 286(45), 38825-38832.

[44] Nussbaum, J. M., Schilling, S., Cynis, H., Silva, A., Swanson, E., Wangsanut, T., Tayler, K., Wiltgen, B., Hatami, A., Reonicke, R. et al. (2012) Prion-like behaviour and tau-dependent cytotoxicity of pyroglutamylated amyloid-β. Nature, 485(7400), 651–655.

[45] Mandler, M., Walker, L., Santic, R., Hanson, P., Upadhaya, A. R., Colloby, S. J., Morris, C.M., Thal, D.R., Thomas, A.J., Schneeberger, A. et al. (2014) Pyroglutamylated amyloid-β is associated with hyperphosphorylated tau and severity of Alzheimer's disease. Acta neuropathologica, 128(1), 67-79.

[46] Gunn, A. P., Wong, B. X., Johanssen, T., Griffith, J. C., Masters, C. L., Bush, A. I., Barnham, K.J., Duce, J.A. & Cherny, R. A. (2016) Amyloid-β peptide Aβ3pE-42 induces lipid peroxidation, membrane permeabilization, and calcium influx in neurons. Journal of Biological Chemistry, 291(12), 6134-6145.

[47] He, W., & Barrow, C. J. (1999) The Aβ 3-pyroglutamyl and 11-pyroglutamyl peptides found in senile plaque have greater β-sheet forming and aggregation propensities in vitro than full-length Aβ. Biochemistry, 38(33), 10871-10877.

[48] Schilling, S., Lauber, T., Schaupp, M., Manhart, S., Scheel, E., Böhm, G., & Demuth, H. U. (2006) On the seeding and oligomerization of pGlu-amyloid peptides (in vitro). Biochemistry, 45(41), 12393-12399.

[49] Schilling, S., Zeitschel, U., Hoffmann, T., Heiser, U., Francke, M., Kehlen, A., Holzer, M., Hutter-Paier, B. Proksech, M. et al. (2008) Glutaminyl cyclase inhibition attenuates pyroglutamate Aβ and Alzheimer's disease–like pathology. Nature Medicine, 14(10), 1106–1111.

[50] Dammers, C., Gremer, L., Reiß, K., Klein, A. N., Neudecker, P., Hartmann, R., Sun, N., Demuth, H.U., Schwarten, M. et al. (2015) Structural analysis and aggregation propensity of pyroglutamate Aβ (3-40) in aqueous trifluoroethanol. PloS One, 10(11), e0143647.

[51] Saido TC, Iwatsubo T, Mann DM, Shimada H, Ihara Y, Kawashima S. Dominant and differential deposition of distinct β-amyloid peptide species, AβN3(pE), in senile plaques. Neuron. 1995;14(2):457-466.

[52] Harigaya Y, Saido TC, Eckman CB, Prada CM, Shoji M, Younkin SG. Amyloid β protein starting pyroglutamate at position 3 is a major component of the amyloid deposits in the Alzheimer's disease brain. Biochem Biophys Res Commun. 2000;276(2):422-427.

[53] Wulff, M., Baumann, M., Thümmler, A., Yadav, J. K., Heinrich, L., Knüpfer, U., Schlenzig, D. Schierhorn, A., rahfeld, J.U., Horn U et al (2016) Enhanced Fibril Fragmentation of N-Terminally Truncated and Pyroglutamyl-Modified Aβ Peptides. Angewandte Chemie International Edition, 55(16), 5081-5084.

[54] Tekirian, T. L., Yang, A. Y., Glabe, C., & Geddes, J. W. (1999) Toxicity of Pyroglutaminated Amyloid β-Peptides 3 (pE)-40 and-42 Is Similar to That of Aβ1-40 and-42. Journal of Neurochemistry, 73(4), 1584-1589.

[55] Sanders, H. M., Lust, R., & Teller, J. K. (2009) Amyloid-beta peptide Aβp3-42 affects early aggregation of full-length Aβ1-42. Peptides, 30(5), 849-854.

[56] Wirths, O., Erck, C., Martens, H., Harmeier, A., Geumann, C., Jawhar, S., Kumar, S., Multhaup, G., Walter, J., Ingelsson, M.et al (2010) Identification of low molecular weight pyroglutamate Aβ oligomers in Alzheimer disease. A novel tool for therapy and diagnosis. Journal of Biological Chemistry, 285(53), 41517-41524.

[57] Bouter, Y., Dietrich, K., Wittnam, J. L., Rezaei-Ghaleh, N., Pillot, T., Papot-Couturier, S., Lefebvre, T.,Sprenger, F., Wirths, O., Zweckstetter, M. et al. (2013) N-truncated amyloid β (Aβ) 4-42 forms stable aggregates and induces acute and long-lasting behavioral deficits. Acta Neuropathologica, 126(2), 189-205.

[58] Schlenzig D, Rönicke R, Cynis H, et al. N-terminal pyroglutamate formation of Aβ38 and Aβ40 enforces oligomer formation and potency to disrupt hippocampal long-term potentiation. J Neurochem. 2012; 121(5):774-784.

[59] Russo C, Violani E, Salis S, et al. Pyroglutamate-modified amyloid β-peptides AβN3(pE)—strongly affect cultured neuron and astrocyte survival. J Neurochem. 2002;82(6):1480-1489.

[60] Tekirian TL, Yang AY, Glabe C, Geddes JW. Toxicity of pyroglutaminated amyloid β-peptides 3(pE)-40 and -42 is similar to that of Aβ1-40 and -42. J Neurochem. 1999;73(4):1584-1589.

[61] Scheidt HA, Adler J, Zeitschel U, et al. Pyroglutamate-modified amyloid β (11-40) fibrils are more toxic than wildtype fibrils but structurally very similar. Chemistry. 2017;23(62):15834-15838.

[62] Sanders HM, Lust R, Teller JK. Amyloid-β peptide Aβp3-42 affects early aggregation of full-length Aβ1-42. Peptides. 2009;30(5): 849-854.

[63] Sigurdsson EM, Permanne B, Soto C, Wisniewski T, Frangione B. In vivo reversal of amyloid-beta lesions in rat brain. *J Neuropathol Exp Neurol.* **59,** 11–17 (2000).

[64] Gordon DJ, Sciarretta KL, Meredith SC. Inhibition of beta-amyloid(40) fibrillogenesis and disassembly of beta-amyloid(40) fibrils by short beta-amyloid congeners containing N-methyl amino acids at alternate residues. Biochemistry. 2001 Jul 27;40(28):8237-45.

[65] Gordon DJ, Meredith SC. Probing the role of backbone hydrogen bonding in beta-amyloid fibrils with inhibitor peptides containing ester bonds at alternate positions. Biochemistry. 2003 Jan 21;42(2):475-85.

[66] Sciarretta KL, Gordon DJ, Meredith SC. Peptide-based inhibitors of amyloid assembly. Methods Enzymol. 2006;413:273-312.

[67] Sepulveda FJ, Parodi J, Peoples RW, Opazo C, Aguayo LG. Synaptotoxicity of Alzheimer beta amyloid can be explained by its membrane perforating property. *PLoS One* **5,** e11820 (2010).

[68] Giordano C, Sansone A, Masi A, Masci A, Mosca L, Chiaraluce R, Pasquo A, Consalvi V. Inhibition of Amyloid Peptide Fragment $A\beta_{25–35}$ Fibrillogenesis and Toxicity by *N*-Terminal β-Amino Acid-Containing Esapeptides: Is Taurine Moiety Essential for *In Vivo* Effects? Chem Biol Drug Des. 2012 Jan;79(1):30-37.

[69] Cheng PN, Liu C, Zhao M, Eisenberg D, Nowick JS. Amyloid β-Sheet Mimics that Antagonize Amyloid Aggregation and Reduce Amyloid Toxicity. Nat Chem. 2012 Nov;4(11):927-33.

[70] Peters C, Fernandez-Perez EJ, Burgos CF, Espinoza MP, Castillo C, Urrutia JC, Streltsov VA, Opazo C, Aguayo LG. Inhibition of amyloid beta-induced synaptotoxicity by a pentapeptide

derived from the glycine zipper region of the neurotoxic peptide. *Neurobiol Aging.* **34,** 2805–2814 (2013).

[71] Bharadwaj P, Head R, Martins R., Raussens V, Sarroukh R, Jegasothy H, Waddington L, Bennett L, Modulation of amyloid-beta 1-42 structure and toxicity by proline-rich whey peptides. *Food Funct.* **4,** 92–103 (2013).

[72] Barucker C, Bittner HJ, Chang PK, Cameron S, Hancock MA, Liebsch F, Hossain S, Harmeier A, Shaw H, Charron FM, Gensler M, Dembny P, Zhuang W, Schmitz D, Rabe JP, Rao Y, Lurz R, Hildebrand PW, McKinney RA, Multhaup G. Aβ42-oligomer Interacting Peptide (AIP) neutralizes toxic amyloid-β42 species and protects synaptic structure and function. Sci Rep. 2015 Oct 29;5:15410.

[73] Rajasekhar K, Madhu C, Govindaraju T. A Natural tripeptide-based inhibitor of multifaceted amyloid β toxicity, *ACS Chem. Neurosci.* **7,** 1300–1310 (2016).

[74] Shea D, Hsu CC, Bi TM, Paranjapye N, Childers MC, Cochran J, Tomberlin CP, Wang L, Paris D, Zonderman J, Varani G, Link CD, Mullan M, Daggett V. α-Sheet secondary structure in amyloid β-peptide drives aggregation and toxicity in Alzheimer's disease. *Proc Natl Acad Sci USA* **116,** 8895–8900 (2019).

[75] Ghosh A, Pradhan N, Bera S, Datta A, Krishnamoorthy J, Jana NR, Bhunia A. Inhibition and degradation of amyloid beta (Aβ40) fibrillation by designed small peptide: A combined spectroscopy, microscopy, and cell toxicity study. *ACS Chem Neurosci.* **8,** 718–722 (2017).

[76] Aoraha E, Candreva J, Kim JR. Engineering of a peptide probe for β-amyloid aggregates. *Mol Biosyst.* **11,** 2281–2289 (2015).

[77] Röhrig UF, Laio A, Tantalo N, Parrinello M, Petronzio R. Stability and structure of oligomers of the Alzheimer peptide Abeta16-22: from the dimer to the 32-mer. *Biophys J.* **91,** 3217–3229 (2006).

[78] Petty SA, Decatur SM. Experimental Evidence for the Reorganization of b-Strands within Aggregates of the A b(16-22) Peptide. J Am Chem Soc. 2005, 127, 13488-13489.

[79] Fradinger EA, Monien BH, Urbanc B, Lomakin A, Tan M, Li H, Spring SM, Condron MM, Cruz L, Xie CW, Benedek GB, Bitan G. C-terminal peptides coassemble into Abeta42 oligomers and protect neurons against Abeta42-induced neurotoxicity. *Proc Natl Acad Sci U S A.* **105,** 14175–14180 (2008).

[80] Li H, Du Z, Lopes DH, Fradinger EA, Wang C, Bitan G. C-terminal tetrapeptides inhibit Aβ42-induced neurotoxicity primarily through specific interaction at the N-terminus of Aβ42. *J Med Chem.* **54,** 8451–8460 (2011).

[81] Urbanc B, Betnel M, Cruz L, Li H, Fradinger EA, Monien BH, Bitan G. Structural basis for Aβ1–42 toxicity inhibition by Aβ C-terminal fragments: discrete molecular dynamics study. *J Mol Biol.* **410,** 316–328 (2011).

[82] Gessel MM, Wu C, Li H, Bitan G, Shea JE, Bowers MT. Aβ(39-42) modulates Aβ oligomerization but not fibril formation. *Biochemistry.* **51,** 108–117 (2012).

[83] Li H, Monien BH, Fradinger EA, Urbanc B, Bitan G. Biophysical characterization of Abeta42 C-terminal fragments: inhibitors of Abeta42 neurotoxicity. *Biochemistry.* **49,** 1259−1267 (2010).

[84] Vandersteen A, Masman MF, De Baets G, Jonckheere W, van der Werf K, Marrink SJ, Rozenski J, Benilova I, De Strooper B, Subramaniam V. *et al.* Molecular plasticity regulates

oligomerization and cytotoxicity of the multipeptide-length amyloid-β peptide pool. *J Biol. Chem.* **287,** 36732–36743 (2012).

[85] Tatulian, S. A. (2013) Structural characterization of membrane proteins and peptides by FTIR and ATR-FTIR spectroscopy. In: Lipid-Protein Interactions (J.H. Kleinschmidt, ed.) (pp. 177-218). Humana Press, Totowa, NJ.

[86] Tatulian, S. A. (2010) Structural analysis of proteins by isotope-edited FTIR spectroscopy. Spectroscopy, 24(1-2), 37-43.

[87] Atkins, P. & de Paula, J (2005) Elements of Physical Chemistry (4th ed.). Oxford University Press. ISBN 978-0-7167-7329-0.

[88] Solomon, E.I. & Lever, A. B. P. (2006) Inorganic Electronic Structure and Spectroscopy. Wiley.

[89] Park, D. (2012) Introduction to the Quantum Theory. Courier Corporation.

[90] Van Holde, K. E., Johnson, W. C., & Ho, P. S. (1998) Principles of Physical Biochemistry, Chapter-10(10.2.2). Prentice Hall, ISBN: 0-13-720459-0.

[91] Woody, R. W. (1996). Theory of circular dichroism of proteins. In Circular dichroism and the conformational analysis of biomolecules (pp. 25-67). Springer, Boston, MA. ISBN 978-1-4419-3249-5.

[92] Lakowicz, J. R. (2013) Principles of Fluorescence Spectroscopy. Springer Science & Business Media. (3rdEd.).

[93] Makhatadze GI, Clore GM, Gronenborn AM. Solvent isotope effect and protein stability. Nat Struct Biol. 1995;2(10):852-855.

[94] Petkova AT, Leapman RD, Guo Z, Yau WM, Mattson MP, Tycko R. Self-propagating, molecular-level polymorphism in Alzheimer's β-amyloid fibrils. Science. 2005;307(5707):262-265.

[95] Jeong JS, Ansaloni A, Mezzenga R, Lashuel HA, Dietler G. Novel mechanistic insight into the molecular basis of amyloidpolymorphism and secondary nucleation during amyloid formation.J Mol Biol. 2013;425(10):1765-1781.

[96] Xue C, Tran J, Wang H, Park G, Hsu F, Guo Z. Aβ42 fibril formation from predominantly oligomeric samples suggests a link between oligomer heterogeneity and fibril polymorphism. R Soc Open Sci.2019;6(7):190179.

[97] Walsh DM, Hartley DM, Condron MM, Selkoe DJ, Teplow DB. In vitro studies of amyloid β-protein fibril assembly and toxicity provide clues to the aetiology of Flemish variant (Ala692!Gly) Alzheimer's disease. Biochem J. 2001;355(3):869-877.

[98] Stine WB Jr, Dahlgren KN, Krafft GA, LaDu MJ. In vitro characterization of conditions for amyloid-β peptide oligomerization and fibrillogenesis. J Biol Chem. 2003;278(13):11612-11622.

[99] Venyaminov SY, Yang JT. Determination of protein secondary structure. In: Fasman DG, ed. Circular Dichroism and the Conformational Analysis of Biomolecules. New York, London: Plenum Press; 1996ch.3:69-107.

[100] Sreerama N, Woody RW. Circular dichroism of peptides and proteins. In: Berova N, Nakanishi K, Woody RW, eds. Circular Dichroism: Principles and Applications. John Wiley & Sons; 2000ch. 21:601-620.

[101] Kelly SM, Price NC. The use of circular dichroism in the investigation of protein structure and function. Curr Protein Pept Sci. 2000;1(4):349-384.

[102] Sreerama N, Venyaminov SY, Woody RW. Estimation of the number of α-helical and β-strand segments in proteins using circular dichroism spectroscopy. Protein Sci. 1999;8(2):370-380.

[103] Nadezhdin KD, Bocharova OV, Bocharov EV, Arseniev AS. Structural and dynamic study of the transmembrane domain of the amyloid precursor protein. Acta Naturae. 2011;3(1):69-76.

[104] Barrett PJ, Song Y, Van Horn WD, et al. The amyloid precursor protein has a flexible transmembrane domain and binds cholesterol. Science. 2012;336(6085):1168-1171.

[105] Goormaghtigh E, Cabiaux V, Ruysschaert JM. Determination of soluble and membrane protein structure by Fourier transform infrared spectroscopy. III. Secondary structures. Subcell Biochem. 1994;23: 405-450.

[106] Jackson M, Mantsch HH. The use and misuse of FTIR spectroscopy in the determination of protein structure. Crit Rev Biochem Mol Biol. 1995;30(2):95-120.

[107] Tatulian SA. FTIR analysis of proteins and protein-membrane interactions. Methods Mol Biol. 2003;2019:281-325.

[108] Dong A, Matsuura J, Manning MC, Carpenter JF. Intermolecular β-sheet results from trifluoroethanol-induced nonnative α-helical structure in β-sheet predominant proteins: infrared and circular dichroism spectroscopic study. Arch Biochem Biophys. 1998;355(2): 275-281.

[109] Brünken S, Müller HS, Endres C, et al. High resolution rotational spectroscopy on D2O up to 2.7 THz in its ground and first excited vibrational bending states. Phys Chem. 2007;9:2103-2112.

[110] Cazzoli G, Dore L, Puzzarini C, Gauss J. The hyperfine structure in the rotational spectra of D2O: lamb-dip measurements and quantum-chemical calculations. Mol Phys. 2010;108(18):2335-2342.

[111] Moran A, Mukamel S. The origin of vibrational mode couplings in various secondary structural motifs of polypeptides. Proc Natl Acad Sci U S A. 2004;101(2):506-510.

[112] Myshakina NS, Asher SA. Peptide bond vibrational coupling. J Phys Chem B. 2007;111(16):4271-4279.

[113] Goldblatt G, Cilenti L, Matos JO, et al. Unmodified and pyroglutamylated amyloid β peptides form hypertoxic hetero-oligomers of unique secondary structure. FEBS j. 2017;284(9):1355-1369.

[114] Torres J, Sepulcre F, Padrós E. Conformational changes in bacteriorhodopsin associated with protein-protein interactions: a functional alpha I-alpha II helix switch? Biochemistry. 1995;34(50): 16320-16326.

[115] Wang J, El-Sayed MA. The effect of protein conformation change from αII to αI on the bacteriorhodopsin photocycle. Biophys J. 2000; 78(4):2031-2036.

[116] Okada Y, Okubo K, Ikeda K, et al. Toxic amyloid tape: a novel mixed antiparallel/parallel β-sheet structure formed by amyloid β-protein on GM1 clusters. ACS Chem Nerosci. 2019;10(1):563-572.

[117] Vivekanandan S, Brender JR, Lee SY, Ramamoorthy AA. Partially folded structure of amyloid-beta(1-40) in an aqueous environment Biochem Biophys Res Commun. 2011;411(2):312-316.

[118] Xiao Y, Ma B, McElheny D, Parthasarathy S, Long F, Hoshi M, Nussinov R, Ishii Y. Aβ(1-42) fibril structure illuminates self-recognition and replication of amyloid in Alzheimer's disease. *Nat Struct Mol Biol.* **22,** 499-505 (2015).

[119] Wälti MA, Ravotti F, Arai H, Glabe CG, Wall JS, Böckmann A, Güntert P, Meier BH, Riek R. Atomic-resolution structure of a disease-relevant Aβ(1-42) amyloid fibril. *Proc Natl Acad Sci USA.* **113,** E4976−E4984 (2016).

[120] Colvin MT, Silvers R, Ni QZ, Can TV, Sergeyev I, Rosay M, Donovan KJ, Michael B, Wall J, Linse S, Griffin RG. Atomic resolution structure of monomorphic Aβ42 amyloid fibrils. *J Am Chem Soc.* **138,** 9663−9674 (2016).

[121] Perczel A., Hollósi M. Turns. In *Circular Dichroism and the Conformational Analysis of Biomolecules*; Fasman, G. D., Ed.; Plemun Press: New York, London, 285–380 (1996).

[122] Hamley IW, Nutt DR, Brown GD, Miravet JF, Escuder B, Rodríguez-Llansola F. Influence of the solvent on the self-assembly of a modified amyloid beta peptide fragment. II. NMR and computer simulation investigation. J Phys Chem B. 2010 Jan 21;114(2):940-51.

[123] Wang J, Tao K, Zhou P, Pambou E, Li Z, Xu H, Rogers S, King S, Lu JR. Tuning self-assembled morphology of the Aβ(16-22) peptide by substitution of phenylalanine residues. Colloids Surf B Biointerfaces. 2016 Nov 1;147:116-123.

[124] Sawaya MR, Sambashivan S, Nelson R, Ivanova MI, Sievers SA, Apostol MI, Thompson MJ, Balbirnie M, Wiltzius JJ, McFarlane HT, Madsen AØ, Riekel C, Eisenberg D. Atomic structures of amyloid cross-beta spines reveal varied steric zippers. Nature. 2007 May 24;447(7143):453-7.

[125] Colletier JP, Laganowsky A, Landau M, Zhao M, Soriaga AB, Goldschmidt L, Flot D, Cascio D, Sawaya MR, Eisenberg D. Molecular basis for amyloid-beta polymorphism. Proc Natl Acad Sci U S A. 2011 Oct 11;108(41):16938-43.

[126] Vugmeyster L, Au DF, Ostrovsky D, Kierl B, Fu R, Hu ZW, Qiang W. Effect of Post-Translational Modifications and Mutations on Amyloid-β Fibrils Dynamics at N Terminus. Biophys J. 2019 Oct 15;117(8):1524-1535.

[127] Söldner CA, Sticht H, Horn AHC. Role of the N-terminus for the stability of an amyloid-β fibril with three-fold symmetry. PLoS One. 2017 Oct 12;12(10):e0186347.

[128] Petty SA, Decatur SM. Experimental Evidence for the Reorganization of b-Strands within Aggregates of the A b(16-22) Peptide. J Am Chem Soc. 2005, 127, 13488-13489.

[129] Giordano C, Sansone A, Masi A, Masci A, Mosca L, Chiaraluce R, Pasquo A, Consalvi V. Inhibition of Amyloid Peptide Fragment $A\beta_{25–35}$ Fibrillogenesis and Toxicity by *N*-Terminal β-Amino Acid-Containing Esapeptides: Is Taurine Moiety Essential for *In Vivo* Effects? Chem Biol Drug Des. 2012 Jan;79(1):30-37.

[130] Peters C, Fernandez-Perez EJ, Burgos CF, Espinoza MP, Castillo C, Urrutia JC, Streltsov VA, Opazo C, Aguayo LG. Inhibition of amyloid beta-induced synaptotoxicity by a pentapeptide derived from the glycine zipper region of the neurotoxic peptide. *Neurobiol Aging.* **34,** 2805–2814 (2013).

[131] Wang W, Hou TT, Jia LF, Wu QQ, Quan MN, Jia JP. Toxic amyloid-β oligomers induced self-replication in astrocytes triggering neuronal injury. *EBioMedicine.* **42,** 174–187 (2019).

[132] Fradinger EA, Monien BH, Urbanc B, Lomakin A, Tan M, Li H, Spring SM, Condron MM, Cruz L, Xie CW, Benedek GB, Bitan G. C-terminal peptides coassemble into Abeta42 oligomers and protect neurons against Abeta42-induced neurotoxicity. *Proc Natl Acad Sci U S A.* **105,** 14175–14180 (2008).

[133] Gordon DJ, Meredith SC. Probing the role of backbone hydrogen bonding in beta-amyloid fibrils with inhibitor peptides containing ester bonds at alternate positions. Biochemistry. 2003 Jan 21;42(2):475-85.

[134] An Y, Bloom JW, Wheeler SE. Quantifying the π-Stacking Interactions in Nitroarene Binding Sites of Proteins. J Phys Chem B. 2015 Nov 12;119(45):14441-50.

[135] Du M, Zhou K, Yu R, Zhai Y, Chen G, Wang Q. Noncovalent Self-Assembly of Protein Crystals with Tunable Structures. Nano Lett. 2021 Feb 24;21(4):1749-1757.

[136] Hansen AL, Kay LE. Measurement of histidine pKa values and tautomer populations in invisible protein states. PNAS April 29, 2014 111 (17) E1705-E1712.

[137] Hilbich, C.; Kisters-Woike, B.; Reed, J.; Masters, C. L.; Beyreuther, K. Human and rodent sequence analogs of Alzheimer's amyloid beta A4 share similar properties and can be solubilized in buffers of pH 7.4. Eur. J. Biochem. 1991, 201, 61-69.

[138] Nguyen K, Rabenstein DL. Interaction of the Heparin-Binding Consensus Sequence of β-Amyloid Peptides with Heparin and Heparin-Derived Oligosaccharides. J Phys Chem B 2016 Mar 10;120(9):2187-97.

[139] Balbach JJ, Ishii Y, Antzutkin ON, Leapman RD, Rizzo NW, Dyda F, Reed J, Tycko R. Amyloid fibril formation by A beta 16-22, a seven-residue fragment of the Alzheimr's beta-amyloid peptide, and structural characterization by solid state NMR. Biochemistry. 2000 Nov 14;39(45):13748-59.

[140] Santini S, Wei G, Mousseau N, Derreumaux P. Pathway complexity of Alzheimer's beta-amyloid Abeta16-22 peptide assembly. Structure. 2004 Jul;12(7):1245-55.

[141] Tao K, Wang J, Zhou P, Wang C, Xu H, Zhao X, Lu JR. Self-assembly of short aβ(16-22) peptides: effect of terminal capping and the role of electrostatic interaction. Langmuir. 2011 Mar 15;27(6):2723-30.

[142] Klimov DK, Thirumalai D. Dissecting the assembly of Abeta16-22 amyloid peptides into antiparallel beta sheets. Structure. 2003 Mar;11(3):295-307.

[143] Lazo ND, Grant MA, Condron MC, Rigby AC, Teplow DB. On the nucleation of amyloid beta-protein monomer folding. Protein Sci. 2005 Jun;14(6):1581-96.

[144] Roychaudhuri R, Yang M, Condron MM, Teplow DB. Structural dynamics of the amyloid β-protein monomer folding nucleus. Biochemistry. 2012 May 15;51(19):3957-9.

[145] Hoyer W, Grönwall C, Jonsson A, Ståhl S, Härd T. Stabilization of a beta-hairpin in monomeric Alzheimer's amyloid-beta peptide inhibits amyloid formation. Proc Natl Acad Sci U S A. 2008 Apr 1;105(13):5099-104.

[146] Terzi E, Hölzemann G, Seelig J. Reversible random coil-beta-sheet transition of the Alzheimer beta-amyloid fragment (25-35). Biochemistry. 1994 Feb 15;33(6):1345-50.

[147] Kandel N., Zheng T., Huo Q., and Tatulian S.A. (2017) Membrane Binding and Pore Formation by a Cytotoxic Fragment of Amyloid β Peptide. *J. Phys. Chem. B.* 121, 10293-10305.

[148] Kohno, T.; Kobayashi, K.; Maeda, T.; Sato, K.; Takashima, A. Three-dimensional structures of the amyloid *b*-peptide (25-35) in membrane-mimicking environment. *Biochemistry* 1996, *35*, 16094-16104.

[149] D'Ursi AM, Armenante MR, Guerrini R, Salvadori S, Sorrentino G, Picone D. Solution structure of amyloid beta-peptide (25-35) in different media. J Med Chem. 2004 Aug 12;47(17):4231-8.

[150] Do TD, LaPointe NE, Nelson R, Krotee P, Hayden EY, Ulrich B, Quan S, Feinstein SC, Teplow DB, Eisenberg D, Shea JE, Bowers MT. Amyloid β-Protein C-Terminal Fragments: Formation of Cylindrins and β-Barrels. J Am Chem Soc. 2016 Jan 20;138(2):549-57.

[151] E. M. Phizicky and S. Fields, "Protein-protein interactions: methods for detection and analysis," Microbiological Reviews, vol. 59, no. 1, pp. 94–123, 1995.

[152] A. K. Dunker, M. S. Cortese, P. Romero, L. M. Iakoucheva, and V. N. Uversky, "Flexible nets: the roles of intrinsic disorder in protein interaction networks," FEBS Journal, vol. 272, no. 20, pp. 5129–5148, 2005.

[153] M. Sarmady, W. Dampier, and A. Tozeren, "HIV protein sequence hotspots for crosstalk with host hub proteins," PLoS ONE, vol. 6, no. 8, Article ID e23293, 2011.